# Structure and Light Emission in Germanium Nanoparticles

A thesis presented

by

**Ali Karatutlu**

to

School of Physics and Astronomy

in partial fulfilment of the requirements

for the degree of

Doctor of Philosophy

in the subject of

Physics

Queen Mary, University of London

London, United Kingdom

May, 2014

Submitted by: Ali Karatutlu

Supervisor: Dr. Andrei V. Sapelkin

Examiners:

Prof Andrea Sella

and

Prof Richard Walton

“So surely, with the hardship there is relief!”

“Qur’an, Opening up, 5-6

# Abstract

In this study, advanced techniques in the synthesis of germanium nanoparticles have been investigated. Based on physical and chemical production methods, including stain etching, liquid-phase pulsed laser ablation, sol-gel synthesis and two benchtop colloidal synthesis techniques, germanium nanoparticles with various surface terminations were formed. Out of those, colloidal synthesis by benchtop chemistry (named $CS_1$) were found to be the most promising synthesis route in terms of yield and stability of the as-prepared Ge qdots and its luminescence with almost no oxides present. For the characterisation of Ge nanoparticles, Raman spectroscopy, Photoluminescence (PL) spectroscopy, Transmission electron microscopy (TEM) with energy dispersive X-ray spectroscopy (EDX) and selective area electron diffraction (SAED) techniques were utilised before conducting X-ray absorption spectroscopy (XAS) measurements. The structure and morphology of Ge quantum dots formed using colloidal synthesis routes were found to fit best to the model of a nanocrystalline core surrounded by disordered Ge layers.

Optically-detected X-ray absorption studies have enabled us to establish a direct link between nanoparticles structure and the source of the luminescence. The most important outcome of this study is that it provides a direct experimental route linking synthesis conditions and properties of nanosized Ge quantum dots.

Furthermore, using annealing, we can control surface termination even further, as well as change particle size and possibly produce metastable phases.

# Publication List

1. A. Karatutlu, W. R. Little, A. V Sapelkin, A. Dent, F. G. Mosselmans, G. Cibin, R. Taylor, *J. Phys. Conf. Ser.* **2013**, *430*, 1–6.
2. A. V Sapelkin, D. Bolmatov, A. Karatutlu, W. Little, K. Trachenko, G. Cibin, R. Taylor, F. G. Mosselmans, A. Dent, G Mountjoy *arXiv:1309.3951* **2013**.

# Conferences

1. Synthesis of colloidal Ge quantum dots and its viability in living cells in E-MRS 2013 Fall Meeting, Warsaw University of Technology, Poland - September, 2013.
2. EXAFS and OD-EXAFS: Structure and luminescence in Ge quantum dots in 15th X-ray Absorption Fine Structure in Beijing, China - July 2012.
3. Raman and Photoluminescence study of chemically and physically prepared Ge nanoparticles in 17th International Summer School On Vacuum, Electron And Ion Technologies, Bourgas, Bulgaria - October 2011.

# Declaration

I declare that this work was performed entirely by myself under the supervision of Dr. Andrei V Sapelkin during the course of my Ph.D. studies at the School of Physics and Astronomy, Queen Mary University of London. No part of this thesis has been submitted elsewhere for any other degree.

*To my beloved family!*

# Acknowledgements

This thesis and the results are due to the invaluable help I received from a number of individuals and organisations.

To begin with, I would like to express my thanks to Dr Andrei V Sapelkin, who was not only an enthusiastic supervisor and role-model for me, but also provided me with an environment and the space to work in my own way and at my own pace. I have learnt many of the necessary skills required by an academic from Dr Sapelkin, including critical thinking, timing, doing research, presenting, a willingness to help resolve, time and again, a series of never-ending questions, constructive criticism and supervising.

I am indebted to the financial support given by the School of Physics and Astronomy, Queen Mary University of London (QMUL). Without this support, I would not have been able to participate in a world-leading research institute such us QMUL. In addition, I would also like to express my sincere thanks for providing me with a friendly environment in which everyone can talk and be listened to, with no imposing or forcing of ideologies.

Discussions, analyses and assistance were also given by other members of the group: Mr William R Little, for his Raman spectroscopy analysis software (Matlab and Mathematica codes) and fruitful discussions within the last three years; Mr Osman Ersoy for his support in synthesis and characterisation; Dr Ann P Wheeler and Mr Mingying Song for the bio-related works such as viability tests of Ge qdots and fluorescent images provided; Mr Yuanpeng Zhang for his help in analysing some X-ray absorption and diffraction; and Dr Pascal Puech for his Raman measurements. All these individuals helped me to complete the overall picture of the project. These colleagues have become lifelong friends and I count

myself lucky to have been able to work alongside them.

As additional thanks must go to: Diamond Light Source in the UK for the provision when conducting X-ray absorption and X-ray diffraction studies in the station; B18 and its people, including Dr G Cibin, Dr R Taylor, Dr F Mosselmans and Dr A J Dent for their collaboration and help before and after the beamtime; Dr Ignacio Hernandez and Dr Ahmed Ghandour for their help, particularly in my first year when they were doing post-doctoral research; to Dr John Dennis for the discussions we had before some of the chemical synthesis; Dr Filippo Boi and Dr Zofia Luklinska for their help in TEM measurements, particularly Filippo was usually there for me when I needed assistance in the laboratory.

I would like to mention some further names in the school: Prof. Martin Dove for his genial leadership, helpful lectures and encouragement to us to take part in CCMMP seminars and ‘Coffee hour in the Museum’; Ms Sarah Cowls for her guidance on the QMUL research fund and other management-related issues.

In addition, there are some people behind the scenes who supported me voluntarily, and to whom I owe special thanks and gratitude for helping me to maintain physical, mental and spiritual strength. I would not live in such a peaceful place without them, brothers to me not in bone if not in blood.

I also would like to thank my MSc study supervisor, Dr Bayram Unal, who supported me in my most vulnerable moments, when I needed help in resolving not only scientific problems but also personal matters. Dr Bayram Unal also showed me a very good example of how to build a state-of-the-art research centre, from the application processes to the funding needed for running the centre.

I would like to express my genuine thanks and gratitude to my family, friends and supporters. Love, affection, voluntary support, encouragement and the prayers of my parents, Mr and Mrs Karatutlu, cannot be repaid in any way, except with my gratitude to them and the hope that further success in my career will give them joy and happiness.

I would also like to express my thanks and acknowledgements to the Almighty, Who talented me with precious rewards and immeasurable blessings. The health, peace and strength given to me by the Almighty allowed me to truly be myself.

Finally, I would like to acknowledge my appreciation for each of the people, teachers and relatives who have helped me to become who I am today.

Ali Karatutlu

September 2013

# Table of Contents

## Abbreviations & Acronyms

a-Ge: amorphous germanium

Ca$_1$: Ge nanoparticles formed using benchtop colloidal synthesis method II

Ca$_1$-H$_2$Ar450$^{o}$C: Ca$_1$ nanoparticles annealed in H$_2$/Ar (5%/95%) at 450 $^{o}$C

Ca$_1$-H$_2$Ar600$^{o}$C: Ca$_1$ nanoparticles annealed in H$_2$/Ar (5%/95%) at 600 $^{o}$C

CS$_1$: Ge nanoparticles formed using benchtop colloidal synthesis method I

CS$_1$-H$_2$: Ge nanoparticles formed using benchtop colloidal synthesis method I purged with H$_2$/Ar (5%/95%) instead of Ar gas

CS$_1$-H$_2$Ar: CS$_1$ nanoparticles annealed in H$_2$/Ar (5%/95%)

EDX: Energy dispersive X-ray spectroscopy

EXAFS: Extended X-ray absorption fine structure

LP-PLA: liquid phase pulsed-laser ablation

nc-Ge: nanocrystalline germanium

OD-EXAFS: Optically detected extended X-ray absorption fine structure

PL: Photoluminescence

QCE: Quantum confinement effect

qdots: quantum dots

RFC: Richter, Campbell and Fauchet phonon confinement model

SAED: Selected area electron diffraction

TEM: Transmission electron microscope

XANES: X-ray absorption near edge structure

XAS: X-ray absorption spectroscopy

XEOL: X-ray excited optical luminescence

XRD: X-ray diffraction

## List of Figures

# List of Tables

# CHAPTER 1. INTRODUCTION

The origin of visible light emission from nanostructures has been a subject of intense debate since the seminal work done by Alivisatos *et al.* (Alivisatos, Harris, Levinos, Steigerwald, & Brus, 1988). The intense research that followed has paved the way towards applications of quantum structures in optoelectronics and in bio-sensing, and contributed to the development of nanotechnology. However, the debate has continued, and today the fundamental question about the possible origins of light emission in nanostructures still remains, due to the complexity in recovering the details of atomic arrangements in small quantum dots on a sub-nanoscale. In small particles, the interplay between the core, surface and interfacial region all have a profound effect on their electronic and optical properties. A good example of this is silicon (Si) quantum nanostructures. In 1991, Cullis and Canham (Cullis & Canham, 1991) demonstrated an efficient visible light emission at room temperature from electro-chemically formed porous silicon. This was explained through quantum confinement effect (Cullis & Canham, 1991; Maeda, Tsukamoto, Yazawa, Kanemitsu, & Masumoto, 1991) (QCE): the change in visible light emission due to the confinement of excitons when the size of the nanoparticles is comparable with the exciton Bohr radius. This effect is responsible for the blue shift of the emission of absorption (and photoluminescent) spectrum (James R. Heath, Shiang, & Alivisatos, 1994; Maeda *et al.*, 1991), and is due to the change in size of the nanoparticles. On the other hand, in the second approach, in addition to the QCE, C. Delerue and co-workers (Delerue, Allan, & Lannoo, 1998) showed for small Si clusters that surface species such as oxides and hydrides might play an important role in the modification of their emission and absorption properties. Sato *et al.* (Seiichi Sato, Ikeda, Hamada, & Kimura, 2009) also showed that changing the surface termination in Ge nanoparticles with organic molecules or H can alter light emission regardless of the size of the nanoparticle. Furthermore, it has been demonstrated (Daldosso *et al*., 2003) that interface between the surface and the core can play an important role in the electronic properties of small Si quantum dots. Thus, over two decades of research have eventually led to the development of a model of Si nanoparticles that includes core, surface, and interfacial regions. However, there is no single structural method that can provide details of the atomic arrangements and morphology required for unambiguous characterisation of the structure of quantum dots. This brings us to the main challenge, which is to establish a link between structures of nanoparticles and corresponding electronic and optical properties within the QCE model, together with the surface contribution and within disordered (i.e. amorphous) components.

Over two decades later, the questions raised on the origins of light emission of nanoparticles have not been completely resolved yet. This is especially true in free standing Ge nanoparticles (also known as Ge quantum dots or qdots) due the fact that researchers have mostly focused on either Si synthesis or Ge qdots grown on substrates such as Si or inside matrices, such as $SiO_2$ by highly elaborate production techniques using molecular beam epitaxy or sputtering (Gerion *et al.*, 2004). Synthesising Si nanoparticles is also rather elaborate, and limited to methods such as chemical etching by HF (Canham, 1990), solution synthesis at high temperature and pressure (J R Heath, 1992), or high temperature silane-based synthesis (Littau, Szajowski, Muller, Kortan, & Brus, 1993). These synthesis conditions are relatively complex and/or require hazardous environments. Compared to Si, there are several advantages to using Ge. First of all, since Ge is a structural counterpart of Si, one might expect QCE in Ge similar to that in Si.

Nevertheless, QCE can be observed for relatively larger particle sizes of Ge since exciton Bohr radius ($R_B$=24.3 nm) is larger than that of Si ($R_B$=4.9 nm) (H. Yang *et al.*, 2002). Moreover, there is evidence that band gap varies significantly faster as a function of particle size in Ge (within size range similar to that of Si) giving access to shorter light emission wavelengths for nanoparticles below 2 nm (see Figure 1.2.1.4). In addition, the small energy offset (0.13 eV) between direct and indirect band gap values in Ge can provide direct or quasi-direct behaviour in nanoscale (Ruddy, Johnson, Smith, & Neale, 2010). On top of those, there are several physical and chemical production methods available that were shown to form free standing Ge nanoparticles in various sizes (Muthuswamy, Iskandar, Amador, & Kauzlarich, 2013). Over those, the chemical etching (Buriak, 2002; Karavanskii *et al.*, 2003), pulsed-laser ablation (Seo, Kim, Kim, Choi, & Jeoung, 2006), the sol-gel technique (Henderson, Hessel, & Veinot, 2008; Henderson, Seino, Puzzo, & Ozin, 2010; Veinot, Henderson, & Hessel, 2009) and colloidal techniques (Chou, Oyler, Motl, & Schaak, 2009; James R. Heath et al., 1994; Heintz, Fink, & Mitchell, 2010; Ruddy et al., 2010; B. R. Taylor, Kauzlarich, Delgado, & Lee, 1999; Vaughn, Bondi, & Schaak, 2010; J. Wu et al., 2011) are the major routes developed recently to produce Ge nanoparticles.

So far there have been various studies reporting photoluminescence emission of Ge nanoparticles and little information about the corresponding atomic structure on a sub-nano scale. Therefore, we believe that a systematic study is required into the relationship between synthesis conditions, atomic structure, nanoscale morphology and optical properties, in order to gain a clear understanding of the contribution of surface termination into optical properties of nanoscale systems.

In this project, the first aim was to find the most effective (in terms of material yield) route of the production of matrix-free Ge nanoparticles. Hence, several synthesis methods were investigated, including stain etching, liquid-phase pulsed laser ablation, sol-gel synthesis and colloidal synthesis routes. The next objective was to provide a comprehensive structural characterisation of the produced samples in order to understand the effect of the synthesis routes on the structure and optical properties of matrix-free Ge nanoparticles. We chose to use a combination of short-range and long-range order sensitive structural methods as an approach to achieve the objective. The methods utilised were Raman spectroscopy, X-ray diffraction (XRD), and X-ray absorption spectroscopy (XAS). These were further supported by direct visualisation methods such as light microscopy and transmission electron microscopy (TEM). Photoluminescence and optical (UV-Vis) absorption spectroscopy were used to obtain information about light emission in Ge nanoparticles. Furthermore, we looked at how annealing in the oxygen free environment ($H_2Ar$) affects the structure of as-prepared Ge nanoparticles.

Thus, in the early part of the project, Ge nanoparticles with different surface terminations were synthesised (see section 2.2 Sample Preparation Methods) using chemical stain etching (section 2.2.1, see page 40), liquid phase pulsed-laser ablation (section 2.2.2, see page 43) and the sol-gel method (section 2.2.3, see page 46). Results of Ge nanoparticles with various surface terminations are discussed in CHAPTER 3 (see page 56).

This work was followed by synthesis of Ge nanoparticles performed via bench-top colloidal chemistry synthesis routes (section 3.4, see page 85), using $GeCl_4$ (Chou *et al.*, 2009) and $GeO_2$ (Wu *et al.*, 2011). As performed in the previous synthesis methods, similar characterisation methods in section 3.4 were utilised to investigate the structure of samples. Colloidally prepared samples were investigated using synchrotron-based XRD alongside EXAFS at the Ge K-edge. These synchrotron based radiation characterisation techniques were combined with standard lab-based characterisation techniques such as transmission electron microscopy (TEM), Raman spectroscopy, photoluminescence (PL) spectroscopy and UV-Vis absorption spectroscopy studies. It is also the first study which critically gives a comparison of how synthesis routes affect the final form of the product in terms of structure, stability and light emission.

Thus, the objectives of this project were: (i) to identify the most effective route for the production of Ge quantum dots out of synthesis routes including stain etching, LP-PLA, sol-gel method and colloidal synthesis methods (reducing $GeCl_4$ and $GeO_2$); (ii) to identify structure of Ge nanoparticles formed via each method; and (iii) to understand the origins of light emission if possible.

## 1.1. Group IV Semiconductors

Group IV elements including carbon (C), silicon (Si) and germanium (Ge) are in a position of great importance both in our daily life and in Nanoscience. For instance, silicon plays a crucial role in integrated circuits and is an essential component of semiconductor devices. Silicon carbide (SiC) is also known as one of the best biocompatible materials (Aspenberg *et al.*, 1996). On the other hand, Ge in Group IV is also a crucial element whose usage increases more and more in strained devices, including a combination of Si and Ge (Fan & Chu, 2010).

The following sections in this chapter give some of the background information of these elements, with a particular emphasis on the structural, electronic and optical properties of Ge.

### 1.1.1. Crystal Structure in Group IV Semiconductors

C, Si and Ge have 4 valence electrons available for bonding. These elements crystallise in the diamond-type cubic structure at ambient conditions. The unit cell of the diamond structure is represented in Figure 1.1.1.1. Each atom is tetrahedrally coordinated having 4 nearest neighbours (Bar-Lev., 1984).

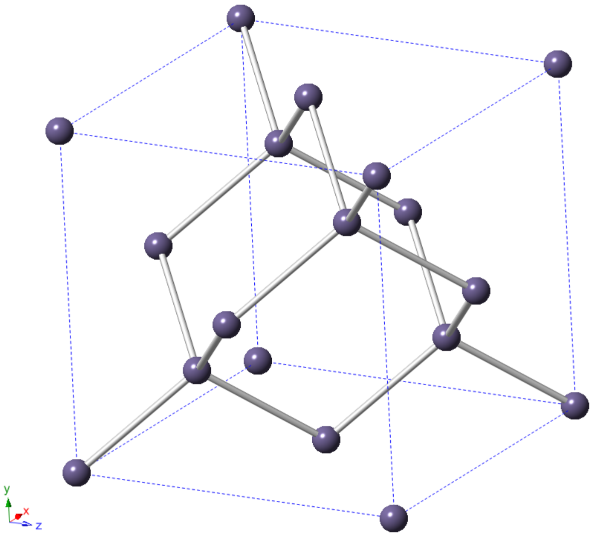

**Figure 1.1.1.1** The unit cell of the diamond cubic crystal structure. The unit cell was constructed using a commercially available software called CrystalMaker (“Crystal Maker,” 2013). [1]

---

[1] The unit cell lattice can be constructed either by entering into the software the type of space group such as $fd\bar{3}m$ for the diamond cubic structure and manually adding the lattice parameters as a = b = c =5.6579 Å; α = β = γ = 90° for crystalline Ge at ambient conditions.

**Table 1.1.1.1** Some of the important properties of Group IV elements.[2]

| **Property** | **C** | **Si** | **Ge** |
|---|---|---|---|
| Atomic Number | 6 | 14 | 32 |
| Band gap (eV) | 5.416 | 1.124 | 0.664 |
| Unit cell length (Å) | 3.57 | 5.43 | 5.66 |
| Bond length (Å) | 1.54 | 2.35 | 2.45 |

Electronic properties of the semiconducting Group IV elements are defined by their band structures, which are in turn defined by the crystal structure and the interatomic potential. Under ambient conditions, C in the diamond structure has a wide indirect band gap. Si and Ge in the diamond structure also have indirect band gaps that are narrower compared to that of C (see Table 1.1.1.1 for the band gap values).

### 1.1.2. Structure of Different Phases in Germanium

As mentioned in Section 1.1.1 Ge is generally found in the diamond cubic structure (Ge-I) at ambient conditions. Nevertheless, a variety of metastable phases have been observed in Ge nanoindentation experiments (Oliver, 2008). It is well-known (Johnson *et al.*, 2013) that a variety of Ge allotropes can become available due to the application of pressure (to the order of 10 GPa) and temperature, which

---

[2] See references (Bar-Lev., 1984) and (Madelung, 2004) for additional information.

result in a dramatic change in its electronic properties. Rapid or slow release of the pressure results in different phases of Ge. For instance, whilst fast depressurisation causes Ge to have a body-centred cubic (BC-8 or Ge-IV) structure, slow release of the pressure transforms those into a tetragonal structure (ST-12 or Ge-III). Figure 1.1.2.1 shows a schematic of the phase transformation of Ge upon release of the pressure.

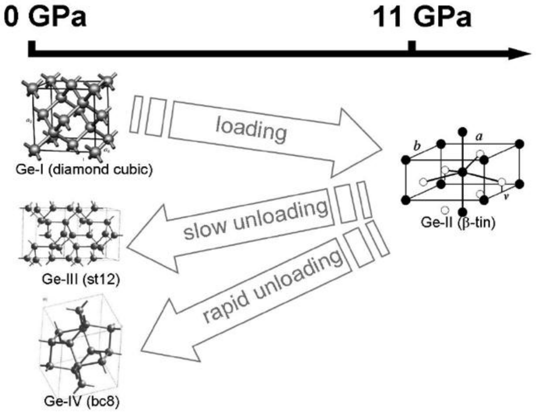

**Figure 1.1.2.1** Schematic of phase transformations in case of slow and fast unloading of crystalline cubic Ge. (Extracted from reference (Oliver, 2008)).

In one of the early studies in 1973, Joannopoulos and Cohen (Joannopoulos & Cohen, 1973) showed that Ge in Ge-I and BC-8 phases are similar in that they have six-fold rings of bonds and one type of atomic environment; on the other hand, ST-12 is different as it has five-fold rings of bonds and can have two types of atomic environment. In other words, all eight atoms in the primitive cells of BC-8 are positioned in the same relative arrangement in which the bond lengths are about the same (2.49 Å). In case of ST-12, the tetragonal unit cell of the ST-12 phase is: a = b = 5.93 Å, c = 6.98 Å, $\alpha = \beta = \gamma = 90$. The first interatomic distance, 2.4802 ± 0.0008 Å ($R_{i1}$ as represented in Figure 1.1.2.2) was found to be about 0.03 Å larger compared to the diamond cubic phase 2.4494 Å (ICDS-43422). There are a further 16 atoms in 7 shells between 3.45 Å, and 4.00 Å. Thus it can be seen that ST-12 gives a more local disorder while retaining tetrahedral-like arrangements. The local disorder means here that we have a crystal in the long-range order, however, the atoms in the primitive cells are located in a “disordered” tetrahedral-like arrangement. ST-12 phase is a direct band gap semiconductor with a band gap of 1.47 eV. The structural models of ST-12 phase given in (a) and (b) were observed upon the release of the high pressure in 1964 (Bundy & Kasper, 1963) and 2008 (Wosylus, Prots’, Schnelle, Hanfland, & Schwarz, 2008) respectively.

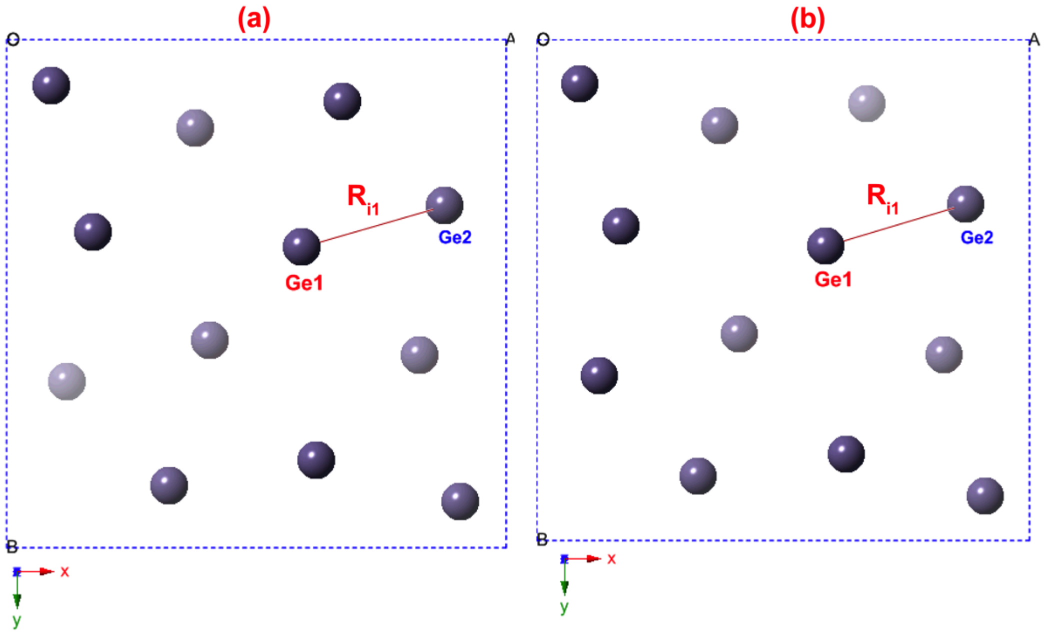

**Figure 1.1.2.2** ST-12 structures constructed using ICSD cards (a) ICDS-16570 and (a) ICDS-419380 are observed in the view direction of z-axis. For (a) and (b), the nearest interatomic distance, $R_{i1}$ were found to be 2.4793 ± 0.0383 Å and 2.4802 ± 0.0008 Å. The unit cells of the (a) and (b) are a=b=5.930 Å, c=6.980 Å and a=b=5.928 Å, c=6.980 Å respectively.

The first interatomic distance of the positions of Ge atoms inside ST-12 phase are close to that of amorphous Ge (a-Ge). In a-Ge, the average interatomic distances is 2.48 Å within the random tetrahedral amorphous structure (Ding & Andersen, 1986).

Ge can readily form oxides and thus forms $GeO_2$, which can then be either found as crystalline polymorphs of alpha-quartz (trigonal, see Figure 1.1.2.3), rutile (tetragonal, see Figure 1.1.2.4) type structures or can be found to have an amorphous structure in the form of $GeO_2$ glass (a-$GeO_2$) (Micoulaut, Cormier, & Henderson, 2006).

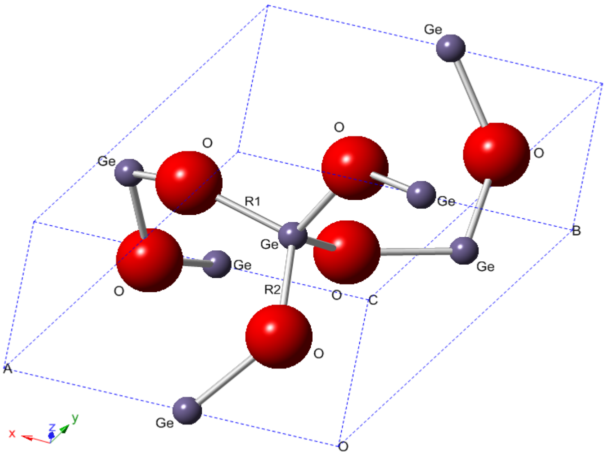

**Figure 1.1.2.3** The unit cell of the alpha-quartz (trigonal) type $GeO_2$ shows two independent Ge-O bond distances as R1 and R2. Ge atoms and O atoms are represented by violet and red spheres respectively.

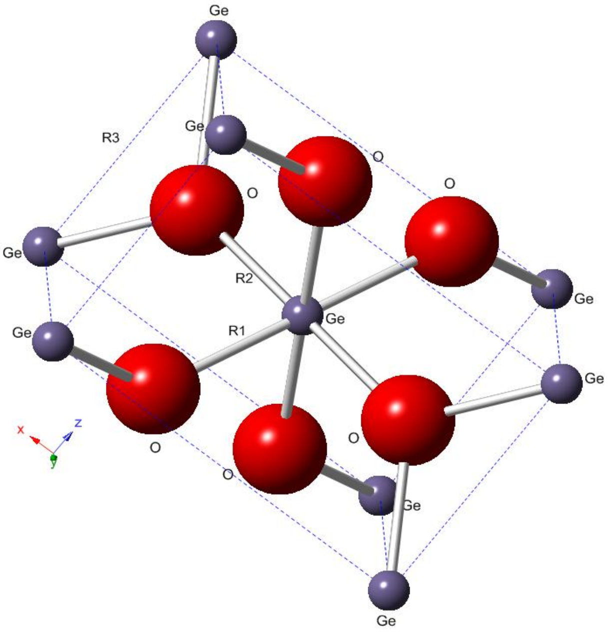

**Figure 1.1.2.4** The unit cell of the rutile type $GeO_2$ shows two axial Ge-O bonds (R2) are longer four equatorial Ge-O bonds within the $GeO_6$ polyhedron. Ge atoms and O atoms are represented by violet and red spheres respectively.

The interatomic distances (R1 and R2) and the lattice parameters of the alpha-quartz and the rutile $GeO_2$ structures are given in Table 1.1.2.1. The structure of a-$GeO_2$ can be viewed as a continuous random network of tetrahedrally bonded Ge-O atoms like in alpha-quartz type $GeO_2$. In a-$GeO_2$, the interatomic distances of Ge-O, O-O and Ge-Ge are given as 1.73, 2.85 and 3.17 ± 0.04 Å according to the results given by XRD and neutron diffraction measurements (Micoulaut *et al.*, 2006).

**Table 1.1.2.1** The axial Ge-O bonds and the lattice parameters in the alpha-quartz and the rutile type $GeO_2$.[3]

| **Material** | **Alpha-quartz** | **Rutile** |
|---|---|---|
| Band gap (eV) | 6.0 eV | 5.35 eV |
| Lattice parameters (Å) | a= 4.987<br>b= 4.987<br>c=5.652 | a=4.407<br>b=4.407<br>c=2.862 |
| R1 (Å) | 1.741±0.001 | 1.8721±0.0002 |
| R2 (Å) | 3.153±0.004 | 2.861±0.0003 |

Amorphisation was also believed to be a precursor for the phase transformation at high pressure from alpha-quartz type $GeO_2$ to rutile type $GeO_2$ (Tsuchiya, Yamanaka, & Matsui, 1998).

---

[3] The values are extracted from the structural models based on the alpha-quartz and the rutile type $GeO_2$ structures using the structural database cards of COD ID: 9007477 and COD ID: 2101851. The nearest Ge-Ge bonds in alpha-quartz and rutile type $GeO_2$ have a bond distance of 3.153 Å and 2.861 Å respectively. The bond angles for the alpha-quartz and the rutile type $GeO_2$ are $\alpha=\beta=90^o$, $\gamma=120^o$ and $\alpha=\beta=\gamma=90^o$ respectively.

The band gap values of both alpha-quartz type $GeO_2$ and a-$GeO_2$ glass were found to be at about 6.0 eV at 300 K (Trukhin, 2009). The band gap of the rutile type $GeO_2$ was previously reported (Madelung, 2004) to have a direct transition of 5.35 eV (T=300 K). The emission properties of $GeO_2$ polymorphs and a-$GeO_2$ glasses are generally investigated using photoluminescence spectroscopy (see page 24 for the technique) and the corresponding emission values are represented in Table 1.1.2.2.

**Table 1.1.2.2** Photoluminescence Emission bands of $GeO_2$ polymorphs, amorphous $GeO_2$ glass and ST-12 phase of Ge thin film

| **Property** | **Excitation eV (nm)** | **Photoluminescence emission eV (nm)** |
|---|---|---|
| **Pure crystalline Alpha-quartz type $GeO_2$** | ≈4.35 eV (285 nm) at 80 K<br>(Fitting, Barfels, Trukhin, & Schmidt, 2001) | ≈2.40 eV (515 nm) at 80 K |
| **Rutile type $GeO_2$** | ≈3.68 eV (337 nm) at 280 K<br>≈5.00 eV (248 nm) at 80 K<br>(Fitting *et al.*, 2001) | ≈2.30 eV (539 nm) at 280 K<br>≈2.30 eV (539 nm) and ≈3.00 eV (413 nm) at 80 K |
| **Amorphous $GeO_2$ Glass** | ≈4.16 eV (298 nm) at room temperature<br>(Xu, Zhu, Chen, Fung, & Li, 1996) | 2.85 eV (435 nm), 3.05 eV (406 nm), 3.18 eV (389 nm), 3.35 eV (370 nm) at room temperature |
| | ≈4.35 eV (285 nm)<br>(Fitting *et al.*, 2001) | ≈2.40 eV (515 nm) at 80 K |
| **Bulk Ge (Diamond)** | 2.41 eV (514 nm) at 7 K<br>(Lieten *et al.*, 2012) | 0.730 eV (≈1699 nm), 0.710 eV (≈1747 nm), 0.702 eV (≈1766 nm) at 7 K |
| **a-Ge:H** | 1.92 eV (≈645 nm) at 2 K<br>(Noll, Carius, & Fuhs, 1985) | 0.6 eV, 0.7 eV at 2 K |
| **Ge thin films (ST-12)** | ≈3.96 eV (313 nm) at 77 K<br>(Nozaki, Sato, Rath, Ono, & Morisaki, 1999) | No luminescence observed (as-prepared) at 77 K<br>2.80 eV (442 nm) (oxidised) at 77 K |

The photoluminescence emission values of the bulk Ge in the diamond cubic structure, hydrogenated a-Ge (a-Ge:H) and ST-12 phase of germanium film (before and after oxidation) are also shown in Table 1.1.2.2 for comparison.

General characteristic of emission properties of $GeO_2$ polymorphs and a-$GeO_2$ is that they all exhibit light emission at around have green 550 nm. Rutile type $GeO_2$ also has a violet emission at 400 nm when the PL measurement is performed at low temperatures such as 80 K.

The next section introduces the change of the properties of germanium from the bulk to the nanosize regime including size and surface effect on its electronic and emission properties. Furthermore, the local structural changes in case of the nanoparticles are also mentioned in the following section.

## 1.2. Properties of Semiconductor Nanostructures

In this section we consider the effects of size onto the properties of germanium including size and surface effect on its electronic and emission properties. Furthermore, the local structural changes in the case of the nanoparticles are also considered.

### 1.2.1. Electronic Band Structure and Quantum Confinement Effect (QCE)

Semiconductor nanostructures are inorganic structures which can be subdivided into various types such as thin films (2D), nanopillars and nanowires (1D) and nanoparticles (0D), also known as quantum dots (Alivisatos, 1996b). The interest in quantum dots is driven by the significant changes in the physical properties of the semiconductor quantum dots, such as energy band gap increases as a function of reduced size. This is a phenomenon known as the quantum confinement effect or quantum size effect (Ekimov, Efros, & Onushchenko, 1985) (see Figure 1.2.1.3 and Figure 1.2.1.5). In other words, the size of a nanoparticle affects electronic and optical properties as compared to the bulk sample.

The band gap is the energy range where no electron states can exist. In the following we consider the effect of size on the energy difference between the highest occupied band (valence band) and lowest unoccupied band (conduction band). Physical interpretation of the optical properties of semiconductors is usually made according to the type of electronic band gap of the semiconductor. Hence, depending on the type of their electronic band gaps, semiconductors can be broadly divided into two categories, such as direct band gap as seen in Group II-VI and Group III-V compounds (e.g. CdSe, ZnS, InP), and indirect band gap as observed in covalent Group IV compounds (e.g. Si, Ge) (Efros & Rosen, 2000). For instance, the minimum energy required to promote one electron from the valence band to the conduction band is 0.67 eV in Ge (see Figure 1.2.1.1(a)). Here, in order to conserve momentum, phonons are required for the lowest energy transition between conduction electrons and holes (see Figure 1.2.1.2).

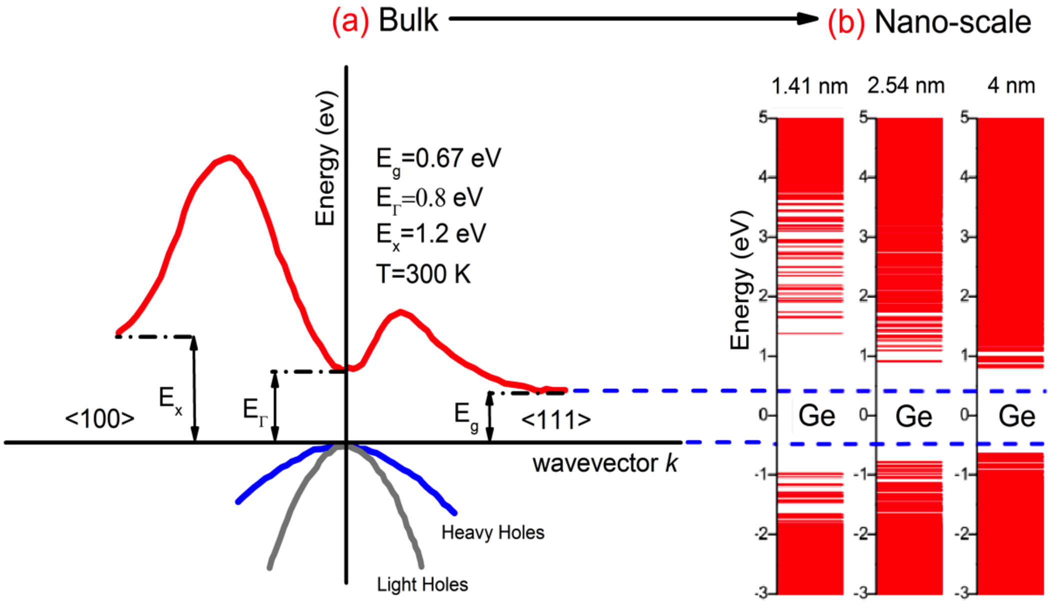

**Figure 1.2.1.1** a) Energy-wavevector (E-k) diagram for indirect band gap elemental semiconductor germanium (b) Evolution of band gap from bulk to nanocrystalline Ge. Blue dashed line shows the band gap energy in Bulk Ge. (Figure (a) and (b) were taken from references ("Bulk Ge Band Gap," 2010) and (Bulutay, 2007) respectively)

In bulk semiconductors, current carriers such as electrons and holes can be described by Bloch waves, which are free to move inside the lattice potential. However, in semiconductor nanocrystals, the carrier motion is spatially confined, which may lead to increased interaction between the carriers. Based on this notion, the band gap is observed to increase and is inversely proportional to the finite size of the nanocrystals (see Figure 1.2.1.1(b)).

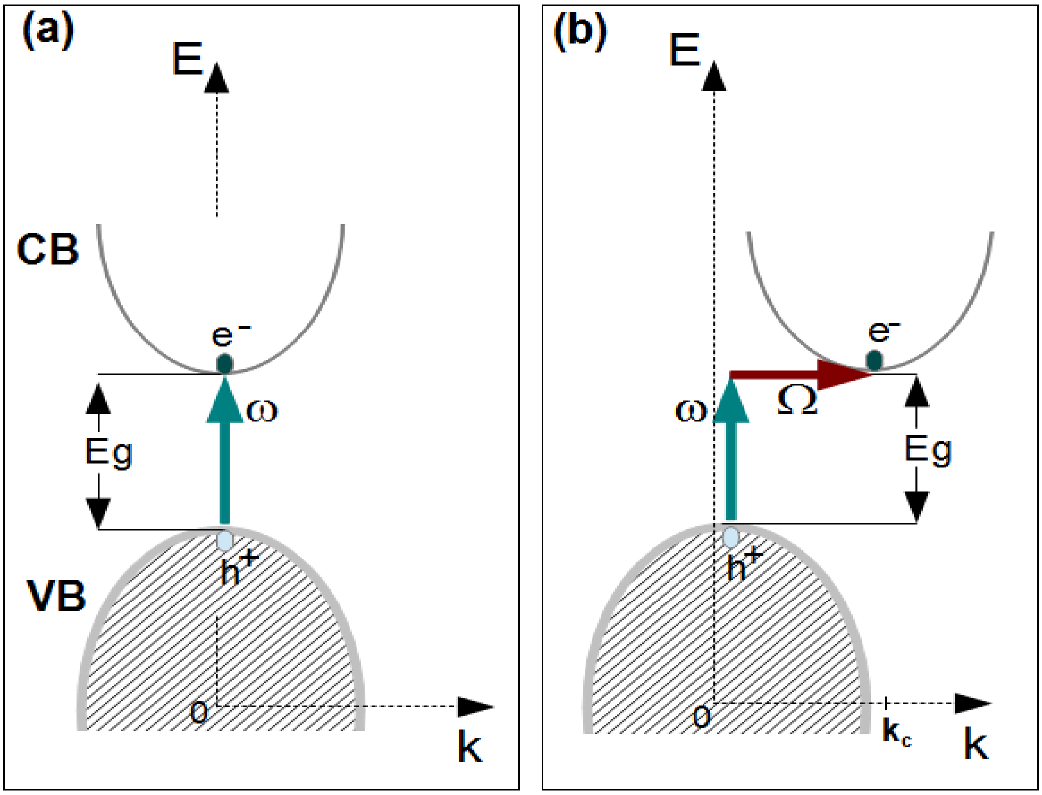

**Figure 1.2.1.2** Schematics of (a) direct and (b) indirect band gaps which illustrates respectively the direct and the indirect transition of the electron upon photo-excitation equal to band gap, $E_g$. Indirect transition (b) involves both a photon and a phonon since the band gap edges of conduction band (CB) and the valence band (VB) are separated with a nonzero $k$-value ($k_c$); $\omega$ and $\Omega$ are frequency of incident photon and emitted phonon which has a vector of $k_c$. (Reproduced from (Kittel, 2004))

The quantum size effect was first observed in 1981 by Ekimov and Onuschenko for CuCl nanocrystals grown in a transparent matrix (Ekimov & Onuschenko, 1981). Using absorption measurements, they observed a change of about 0.1 eV in the band gap of the material upon changing the size of the nanocrystal. Then, QCE studies followed in 1985 by Ekimov *et al.* (Ekimov *et al.*, 1985) for semiconductor nanocrystals inside glassy silica matrix, and Henglein *et al.* (Fojtik, Weller, & Henglein, 1985) for colloidal solutions independently. Efros and Rosen (Efros & Rosen, 2000) reported the progress of the theoretical results on the electronic structure of semiconductor nanocrystals. From semiconductor crystals (bulk) to an ideal nanocrystal, charge carriers (electrons and holes) start feeling confinement depending on the size of the nanocrystal. Since for most semiconductors the electron de Broglie wavelength (16 nm for Ge) and exciton Bohr radius (24 nm for Ge) is larger than the lattice constant (0.56 nm for Ge), the nanocrystal can be thought of as a quantum well (see Figure 1.2.1.3).

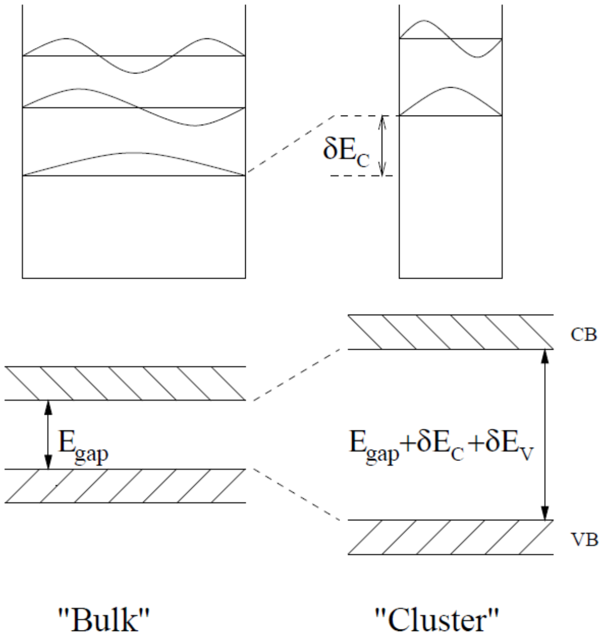

**Figure 1.2.1.3** Schematic diagram of quantum confinement model. Due to decrease in size, nanoparticle can be considered as a quantum well resulting in an increase in the ground state energies. Band gap energy increases, which showed a shift of conduction and valence bands, represented as $\delta E_c$ and $\delta E_v$ respectively. (Extracted from reference (Bostedt, 2002).)

Inside the nanocrystal, electrons and holes can only occupy allowed energy states, which can be explained according to the ‘particle in a box’ model with an infinite potential. In other words, the solution to spherically symmetric infinite potential well can be written in terms of the energy levels of the exciton. The energy shift of the absorption lines (increase in the band gap) due to confinement of the excitons can be written in terms of $\Delta E = \hbar\pi/(2\mu a^2)$ where $\mu$ is the reduced mass of the exciton and $a$ is the average radius of the nanocrystal (Ekimov & Onuschenko, 1981). Hence, the quantum confinement effect is observed once the nanocrystal size is in a certain size regime. From bulk to the nanocrystal size regime, there are two types of QCE considered: weak and strong QCE. In the case of weak QCE, the size of the semiconductor nanocrystal is close to, but still larger than, the exciton Bohr radius ($a_b$). Equation 1.3.1.1 describes the dependence of the exciton absorption lines ($\hbar\omega$) as a function of the size of the nanocrystal (a) under the assumption of the weak QCE ($a > a_b$).

$$\hbar\omega = E_g - E_{ex} + \frac{\hbar^2\pi^2}{2M_s a^2} \qquad \text{Equation 1.3.1.1}$$

where $E_g$ is the bulk band gap energy, $E_{ex}$ is the binding energy of the exciton, $M_s$ is the exciton translational mass ($M_s{=}m_e{+}m_h$).

On the other hand, in strong QCE ($a < a_b$), the nanocrystal size is smaller than the exciton Bohr radius, which results in a relatively big opening of the band gap even for a small change in the size of nanocrystals. Here, the characteristics of the optical spectra are given in Equation 1.3.1.2, in which quantisation of the electrons ($E_v^e(a)$) and holes ($E_v^h(a)$) are considered to be separate ($\kappa$ is a dielectric constant of the bulk semiconductor).

$$\hbar\omega = E_g + E_v{}^e(a) + E_v{}^h(a) - 1.8\frac{e^2}{\kappa a} \qquad \text{Equation 1.3.1.2}$$

Thus the most striking feature of the QCE is a change in the optical properties of the material (sometimes referred to as “blue shift’’), (Alivisatos, 1996a) which can be observed as a wavelength shift of the luminescence emission by changing the size of the nanocrystallite.

Brus (Brus, 1986) also developed a relatively simple confinement model similar to that described above for an electron-hole pair which is known as Brus’s

Model. He predicted the optical band gap of an isolated and a finite size semiconductor nanocrystal, in terms of the band gap of the bulk material, reduced the effective mass of the carriers and the size of the nanocrystal. Meada and co-workers (Maeda *et al.*, 1991) were the first to use Brus's model in Ge nanocrystals embedded in silica despite the fact that the model was not intended to be used with nanocrystals growing densely inside a silica matrix. Still, they observed that the peak of the photoluminescence emission (2.18 eV) did not deviate from the predicted value (2.15 eV) according to the Brus model.

Bostedt (Bostedt, 2002) showed experimentally that there is a change in the band gap with respect to the size of Ge nanoparticles grown on a substrate. His results are given in Figure 1.2.1.4, which shows an increase of the band gap when decreasing the size of Ge nanoparticles.

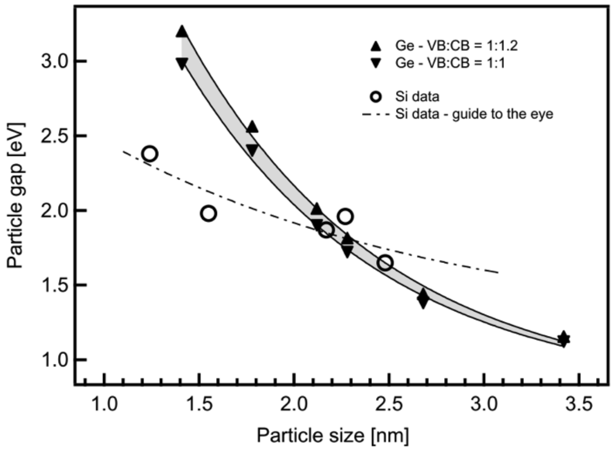

**Figure 1.2.1.4** Comparison of experimental band gap change in Ge and that in Si with respect to corresponding particle size. VB and CB refer to valence band conduction band respectively. (Taken from reference (Bostedt, 2002).)

Niquet *et al.* (Niquet, Allan, Delerue, & Lannoo, 2000) reported an analytical model of how band gap varies with the size of Ge nanocrystals and compared with experimental results of blue-green and near IR emitting Ge nanocrystals. The parabolic band gap increase, as a result of decreasing the size, is a general feature of many semiconductor nanocrystals, and an example of this for Ge is shown in Figure 1.2.1.5.

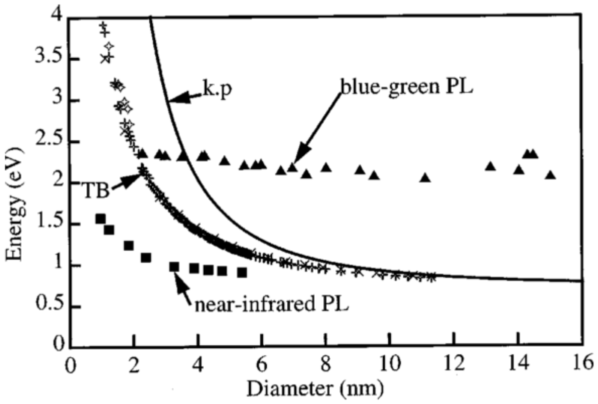

**Figure 1.2.1.5** Band gap change of spherical Ge nanocrystals with respect to its size based on tight binding model and k.p perturbation theory (shown as TB and k.p respectively in the graph) and comparisons with the earlier experimental results reported for Ge. (Extracted from reference (Niquet *et al.*, 2000))

Figure 1.2.1.5 shows that there are discrepancies between experimentally observed luminescence emissions such as in blue-green and near-infrared regions of the electromagnetic spectrum and the theory. One can see from Figure 1.2.1.5 that the experimental data (e.g. blue-green PL and near-infrared PL) do not agree well with the theory. Effects other than size may be important, and especially so for the blue-green PL data. Considering Table 1.1.2.2, blue-green PL may in fact be due to oxides, which suggest the importance of surface termination and surface states in the interpretation of PL data. Thus, the initial step to a clear understanding of the structure of a nanoparticle on an atomic scale is essential in order to interpret the PL emission data.

Ge nanoparticles just like bulk Ge, are usually found to be produced in the diamond cubic structure (Gerion *et al.*, 2004; Heath *et al.*, 1994). Nonetheless, there are studies of Ge nanoparticle deposition on Ge thin film which shows the existence of a stable ST-12 phase in the as-prepared samples (Kim *et al.*, 2010; Nozaki *et al.*, 1999; Sato, Nozaki, Morisaki, & Iwase, 1995). In some samples, there may be some cases in which a crystalline and an amorphous phase coexist together with oxides (Heath *et al.*, 1994). Nevertheless, it is not always clear what is the exact atomic structure of these samples or mixed phases due to the difficulty of identifying multiple phases at the nanoscale. Thus, to gain insight into the situation in the experiments, structural modelling of small Ge nanoparticles has been used. An example model of a matrix-free Ge nanoparticle (about 2 nm in size), as shown in Figure 1.2.1.6, can be used. One can see that crystalline core and surface disorder can co-exist as a Ge-I phase is surrounded by an amorphous shell (Pizzagalli, Galli, Klepeis, & Gygi, 2001). In their model, the interatomic distance in the surface shell was found to be 2.46 Å, which is 2 % larger than crystalline bulk Ge (2.45 Å). However, these models have so far been of limited use as they are only capable of modelling very small (1-2 nm) particles, while in experiments the sizes are usually 10-50 nm.

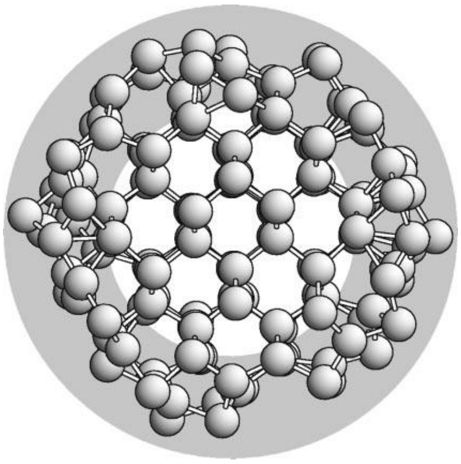

**Figure 1.2.1.6** Cross-sectional view 190 atoms with a core of the diamond cubic like structure (white area) is surrounded by a disordered matrix (grey in color) (Taken from reference (Pizzagalli *et al.*, 2001)).

Recent EXAFS experiment on Ge nanocrystals embedded in silica seems to indicate that the first (2.448±0.002 Å), the second (3.997±0.003 Å) and the third (4.688±0.003 Å) nearest neighbour shells decrease as a function of the size of the nanocrystals (Ridgway *et al.*, 2004), particularly when the size is less 20 nm.

Surface species can also play an important role in affecting the decay process of the photoluminescence emission. Dangling bonds can be saturated with hydrogen or oxide termination. The effect of oxide-termination on the band gap can be observed via oxygen-related defect states and oxygen vacancies (Peng *et al.*, 2011). In other words, surface state due to oxide termination is formed and can result in a ‘’red shift’’ (Hessel, Henderson, & Veinot, 2006), which is a shift to longer wavelengths compared to the light emission simply due to QCE. The scheme in Figure 1.2.1.7 shows the relationship between surface states and core states in a nano-cluster.

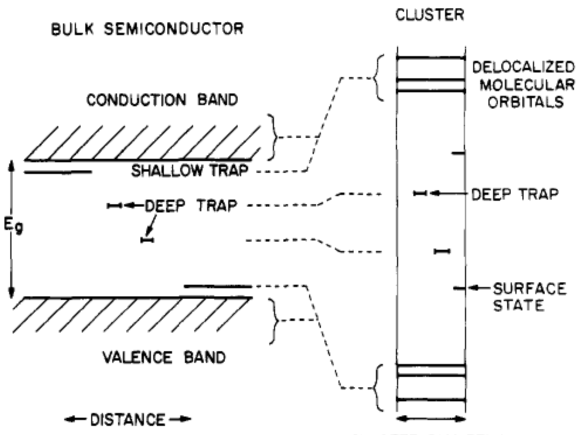

**Figure 1.2.1.7** Schematic of the correlation between nano-cluster states and bulk states (Extracted from reference (Brus, 1986)).

We can now see that QCE, structural effects and surface states can all contribute significantly to the electronic structure of Ge quantum dots. Furthermore, these properties can be significantly influenced by encapsulating matrices and by synthesis conditions. Moreover, the structure of nanosized samples is also influenced significantly by methods of preparation and can be affected by the characterisation techniques. Thus we can see that the main challenges are: (i) to be able consistently to produce structurally and chemically stable matrix-free Ge quantum dots; (ii) to recover both the structure and morphology of quantum dots on sub-nano scale in order to link specific light emission properties to the corresponding morphological (structural) features. In the following chapter we provide description of the synthesis methods we explored and characterisation methods we used to address these challenges.

# CHAPTER 2. EXPERIMENTAL PROCEDURES

## 2.1. Experimental Characterisation Techniques

In order to understand the structural and emission properties of germanium nanoparticles in supra-atomic scale, a combination of various short-range and long-range order techniques is required. In order to build a comprehensive picture of the relationship between structure and optical properties, we utilised the following: Raman and photoluminescence (PL) spectroscopy, UV-Vis absorption spectroscopy, transmission electron microscopy (TEM) with selective area electron diffraction (SAED) and energy dispersive X-ray spectroscopy (EDX), powder X-ray Diffraction (XRD), Extended X-ray Absorption Fine Structure in transmission and optical modes using X-ray excited optical luminescence (XEOL).

### 2.1.1. Raman and Photoluminescence (PL) Spectroscopy

Raman spectroscopy is a fast, convenient and non-destructive technique that covers a wide range of energies with a capability of measuring small changes (down to 0.01 THz) in the vibrational frequencies of molecules (Dove, 2002). Raman spectroscopy as a vibrational technique is based on “Raman shift”, discovered by C. H. Raman in 1928 (Raman & Krishnan, 1928). When light interacts with matter, light is scattered elastically which is known as Rayleigh scattering. Nevertheless, a small portion of the light is scattered non-elastically due to an energy exchange with phonon modes. Frequency (energy) difference between incoming and scattered photons corresponds to the value of energy of vibrational modes. This value can either be positive as the energy is transferred to a phonon (Stoke’s scattering) or negative as energy is gained from a phonon (anti-Stokes scattering, see Figure

2.1.1.1). The Raman technique allows us to record optically active phonons, which are a fingerprint of a specific structure since the phonon spectrum is uniquely defined by symmetry and interatomic interactions. Thus the technique can be used as an indirect method of structural identification.

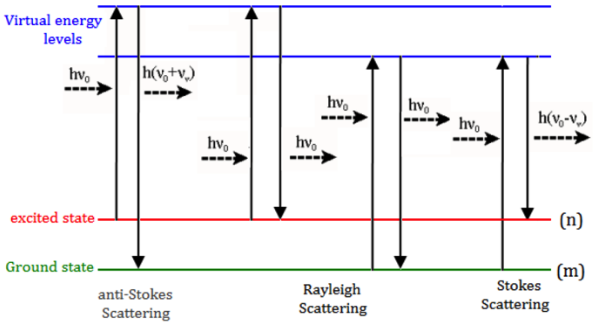

**Figure 2.1.1.1** Scheme of a Raman process: showing from left to right anti-Stokes, Rayleigh and Stokes scattering. (Taken from reference (Ghandour, 2009).)

Raman spectroscopy has also been used as a sensitive probe in order to determine the size of nanocrystalline Ge (nc-Ge) and the crystallinity of the sample (Hayashi & Yamamoto, 1990). In crystalline bulk Ge, only phonons at the zone centre result in a single peak of 300 cm$^{-1}$ due to the selection rule of $k$=0 (Bottani *et al.*, 1996). However, in a-Ge for example, this selection rule does not apply since there is no long-range order and all phonons are optically allowed. Thus, the Raman of a-Ge has a broad hump at 275 cm$^{-1}$ (Fujii, Hayashi, & Yamamoto, 1991). In nanocrystals, finite size effects also affect the Raman signal as the local symmetry and intermediate-range order are still present, but the long-range periodicity is lost. As the size of the nanocrystal decreases, the peak position is shifted to lower frequencies and the FWHM of the spectrum is broadened asymmetrically towards a lower frequency. Broadening is due to an increase of the uncertainty in the energy as the size of the nanocrystal decreases. Asymmetric broadening is caused by probing phonon states away from the Brillouin zone centre where $k$=0.

A phonon confinement model that includes particle size, a free parameter, can describe these effects and thus Raman spectroscopy can be used to extract the average particle size. The model known as Richter's Model or RWL (Richter, Wang, Ley) model was proposed initially by Richter *et al.* in 1981 (Richter, Wang, & Ley, 1981) and took into account the effect of the phonon confinement on the shape and position of the Raman peak. Campbell and Fauchet (Campbell & Fauchet, 1986) improved Richter's Model (RFC model) by considering the exact shape of the nanocrystal. The final expression is shown in Equation 2.1.1.1 and has been widely used to determine particle size in spherical Si and GaAs nanocrystals. Nevertheless, the model can be generally used to find out the average size of nanoparticles. The information required to use this expression for Ge nanoparticles can be given as follows: the bulk optical phonon dispersion curve, the natural line width and peak position of the Raman spectrum of bulk Ge. The model defines the Raman intensity *I*, for a corresponding Raman shift of the wavenumber $\omega$.

$$I(\omega) = \int_0^{2\pi/a_0} \frac{\exp\left(-\frac{qd_0}{4\pi}\right)^2 a_0 \pi q^2}{(\omega-\omega_q)^2 + \left(\frac{\Gamma_0}{2}\right)^2} dq \qquad \text{Equation 2.1.1.1}$$

where $a$, $q$, $d_0$, $\omega_q$ and $\Gamma_0$ stand for the lattice parameter, the phonon wave vector, the particle size, the phonon dispersion curve and the natural line width of Raman peak, respectively. The limitation of this model is the averaging of a complex three dimensional phonon dispersion relationship throughout the first Brillouin zone by replacing it with a single phonon branch (Campbell & Fauchet, 1986). The advantages are fast numerical implementation and reasonable accuracy. We used a code already written in MATLAB to extract particle sizes from Raman signals. The parameters we used for Ge were: $\Gamma_0$ = 7 $\text{cm}^{-1}$ (obtained from a calibration standard); $\omega_q = \left[\omega_0\text{-}104\left(\frac{q}{2\pi/a}\right)\right]^2$ (see Das *et al*., 2000), were $\omega_0$ is 300.6 $\text{cm}^{-1}$. The code simulates FWHM of the experimental Raman peak based on the Voigt or pseudo-Voigt function (convolution of Lorentz and Gaussian functions) and calculates a Raman spectrum for a given size. In other words, the size of Ge nanoparticles is extracted for a corresponding FWHM, which is found after several iterations and fitted (the least squares fitting was used) to the FWHM of the experimental spectrum until the R-factor is smaller than 0.009.

Photoluminescence spectroscopy (PL) is also a non-destructive probe for optical properties of the material. In PL, the excited sample is illuminated by a light source, usually using a continuous laser source. This light is absorbed by the sample and promotes valence electrons to the conduction band. The decay process can be observed as re-emission, which is known as luminescence. When the source of the excitation is light particles (photons), this is the reason it is called photoluminescence (Nataraj, 2010).

When the emission of the photons after the excitation comes directly from the conduction band, the measure of energy from the emitted photons gives a value close to the band gap energy of the material as shown in Figure 2.1.1.2. Nevertheless, this model might not be exactly true, since the final decay process can also come from the surface or from an intermediate region. However, the nature of emission can be much more complicated and is related to surface state states and defects.

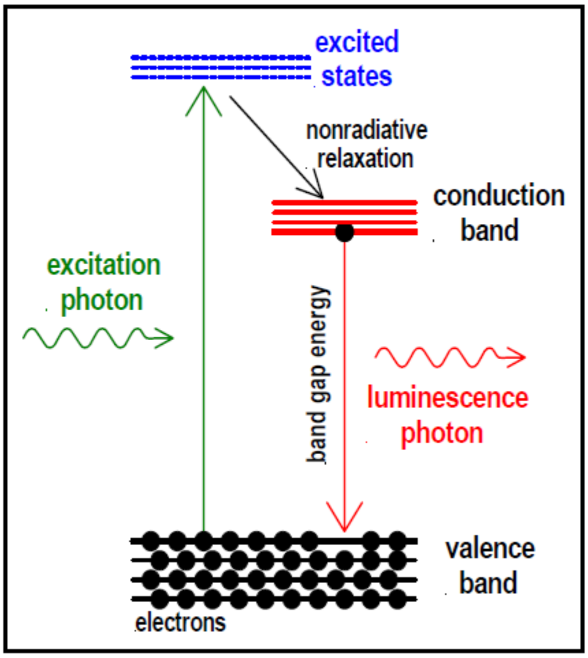

**Figure 2.1.1.2** The scheme of a photoluminescent event (Taken from the reference (Heiman, 2004)).

For Raman and PL measurements, a Renishaw 1000 spectroscopy system (with a He-Ne laser with excitation of 633 nm) and Horiba-JY Labram (diode lasers with the excitations of 473 and 785 nm) with 0.3 nm experimental resolution (See reference (Renishaw, 2002) for more details) were utilised. Before using a spectrometer either for Raman or PL measurements, the spectrometer was calibrated with bulk c-Si wafer. The Raman peak of c-Si wafer is shown in Figure 2.1.1.3. The reference measurement of a bulk c-Si with a peak of 520 $cm^{-1}$ is consistent with the Raman shift of the bulk c-Si by S. Hayashi and K. Yamamoto (520 $cm^{-1}$) (S. Hayashi & Yamamoto, 1990). Every Raman and PL measurement was measured with at least 10 times of accumulation.

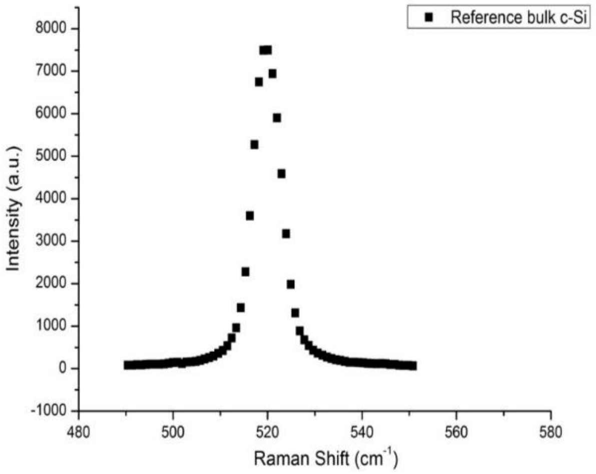

**Figure 2.1.1.3** Reference Raman spectrum of bulk c-Si

For Raman and PL spectroscopy measurements, Ge nanoparticles suspended in ethanol were transferred onto a glass slide using a disposable Pascal pipette. After the ethanol was naturally evaporated, the measurements were performed from the powder.

## 2.1.2. UV-Vis Absorption Spectroscopy

Absorption measurements provide information on how the band gap of Ge nanocrystals alters when reducing the size of the nanocrystals (James R. Heath *et al.*, 1994). It can even show small changes in the optical band gap when the surface species of the nanocrystals change (Taylor *et al.*, 1999; Yang, Bley, Kauzlarich, Lee, & Delgado, 1999). A beam of light on a sample can be absorbed, scattered or transmitted. The Bouger-Lambert-Beer Law given in Equation 2.1.2.1 is used in an absorption measurement in UV-Vis and IR region (Perkampus, Grinter, & Threlfall, 2012).

$$\ln\left(\frac{I_0}{I}\right)_\nu = \log\left(\frac{100}{T(\%)}\right)_\nu = A_\nu \qquad \text{Equation 2.1.2.1}$$

where $A_\upsilon$ is absorbance, $T_\upsilon$ is transmittance, $I_0$ is the initial intensity monochromatic light coming on the sample, $I$ is the intensity of light transmitting.

The spectrometer used in this study has a configuration of Perkin-Elmer Lambda 9 (Perkampus *et al.*, 2012) which consists of a twin monochromator so that the measurement can also simultaneously be recorded for a reference sample.

UV-Vis absorption spectroscopy measurements of the Ge nanoparticles suspended in ethanol were conducted inside a quartz cuvette. The background absorption from the ethanol was taken as a reference and subtracted from the absorption measurement of Ge nanoparticles suspended in ethanol. Thus, only the absorption from Ge nanoparticles could be obtained.

### 2.1.3. Transmission Electron Microscopy (TEM)

Transmission electron microscopy is an electron microscopy technique which can give particle sizes and shapes in the order of 1 Å resolution due to a small de Broglie wavelength of high energy electrons (Fujii *et al.*, 1991). In TEM, an electron beam passes through a very thin sample such as Ge nanoparticles distributed on a C coated Cu grid. After interaction of electrons and sample, an image is reconstructed, magnified and observed using an imaging platform such as a luminescent screen or recorded with a CCD camera (Nataraj, 2010) (see Figure 2.1.3.1).

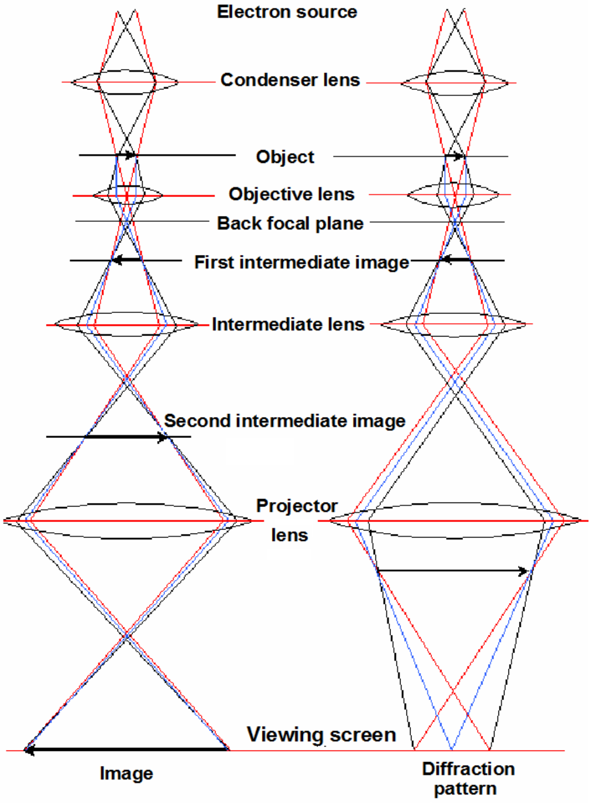

**Figure 2.1.3.1** Scheme of transmission electron microscope (TEM) with selective area electron diffraction (SAED) mode. (Taken from reference ("Tranmission electron microscopy scheme," 2010))

The TEM samples were prepared as follows:

- The Ge nanoparticles prepared using each method were suspended in ethanol after synthesis.[4]
- Then, each of these samples was transferred onto the top of the TEM carbon-coated Cu grid.

---

[4] Before their suspension in ethanol, Ge nanoparticles after each synthesis were separated from the chemical solution using 10000 rpm of centrifugation and washed twice using de-ionised water and ethanol.

- After the ethanol dried completely, the sample on the carbon-coated Cu grid was inserted inside the JEOL JEM 2010 in order to conduct the TEM measurement.

A JEOL JEM 2010 (200 keV) was utilised for TEM measurements, including the modes such as selective area electron diffraction (SAED) and energy dispersive X-ray spectroscopy (EDX). SAED can be used to identify the crystal structure like X-ray diffraction, but instead of averaging the whole sample, SAED can give structure information of materials on a very short scale such as nanoparticles. EDX can be used to identify elements in nanoparticles distributed on the C coated Cu grid. Software called Gatan Digital Micrograph was used in all the TEM collections and the analyses.

In addition to imaging in TEM, from the same area, SAED can give information about the crystal structure of germanium nanoparticles (Shieh, Chen, Ko, Cheng, & Chu, 2004; Taylor *et al.*, 1999). Diffraction spots or rings can correspond to lattice spacing (*d*) of germanium nanocrystals. In other words, for a diamond-cubic crystal in Ge, reflections from certain planes such as (111), (220) can be seen with *d* spacing 3.27 Å and 2.00 Å respectively [21] and used to identify the structure.

### 2.1.4. X-ray Diffraction

X-ray diffraction (XRD) can be utilised to identify the crystal structure of samples. XRD can also be thought of as a complementary technique for the electron diffraction (SAED) and for X-ray absorption spectroscopy, which also probes the local environment of the sample.

The main principle of XRD can be expressed using the Bragg law, as illustrated in Figure 2.1.4.1.

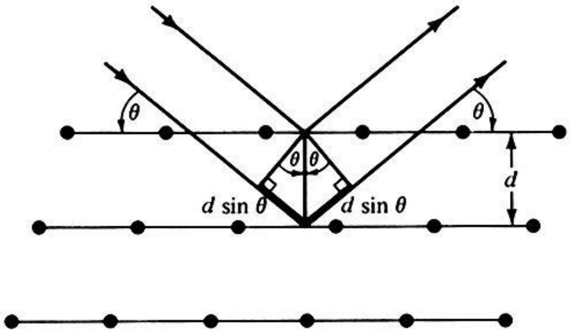

**Figure 2.1.4.1** The scheme of Bragg reflection from a crystalline sample. The reflection occurs from a certain plane depending on the angle of the incident of the X-ray and its wavelength. (Taken from reference (Bostedt, 2002))

Each reflection is due to X-ray scattering from the atomic lattice. A constructive interference, which is characteristic of the crystal structure, occurs when the Bragg reflections given in Equation 2.1.4.1 are satisfied:

$$n\lambda = 2d\sin\theta$$ Equation 2.1.4.1

where $n$ is the integer number, $\lambda$ is the wavelength of the incident X-ray beam, $d$ is the lattice space and $\theta$ is the angle of the incident X-ray beam.

The size of the crystallites, *D*, can be calculated using the Scherrer equation (Yang, 2004), as expressed in Equation 2.1.4.2, using each X-ray reflection from the corresponding planes.

$$D = \frac{0.9\lambda}{\beta\cos\theta}$$ Equation 2.1.4.2

where $\beta$ is the FWHM of the diffracted peak in radians, $\lambda$ is the wavelength of the X-rays in nanometer (nm). This expression works well for samples up to 200 nm – well within the range of sizes of our samples.

X-ray diffraction measurements were carried out at room temperature in station B18, Diamond Light Source, UK with the configuration represented in Figure 2.1.4.2.

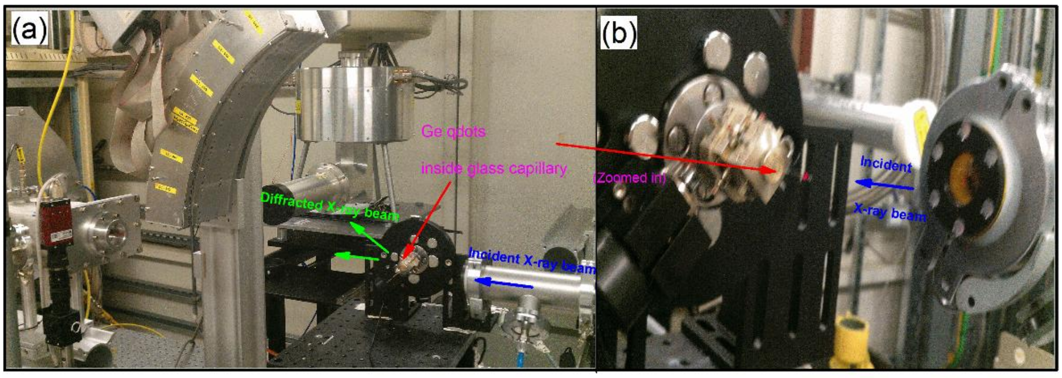

**Figure 2.1.4.2** Picture of X-ray Diffraction measurement conducted at station B18, Diamond Light Source, UK. X-ray beam (λ=1.54409 Å, E=8047 eV) is focused onto Ge qdots inside the glass capillary, which is attached to a rotating stage.

Before conducting the XRD measurements, the samples formed using the colloidal synthesis routes were placed inside a glass capillary (diameter of 0.75 mm) as shown in Figure 2.1.4.3, in order to prevent the formation of oxide.

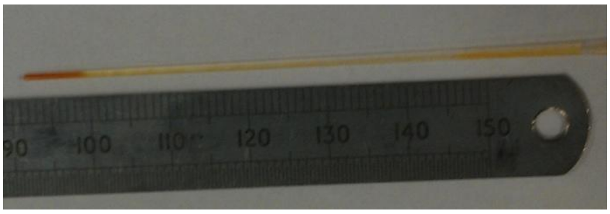

**Figure 2.1.4.3** Ge nanoparticles (yellow colour) prepared using the benchtop colloidal synthesis: method I were transferred inside the glass capillary.

## 2.1.5. X-ray Absorption Fine Structure: EXAFS and OD-EXAFS Using XEOL

X-ray Absorption Fine Structure (XAFS) is a tool to study the local structure of a chosen element as an absorbent at atomic and molecular level. The unique feature of XAFS is that it is element specific and can be applied not only to crystals but also to disordered materials such as glasses and amorphous systems, solutions, and even molecular gases. Hence a wide range of disciplines including physics, chemistry, medicine and engineering can make use of XAFS. In XAFS the absorption coefficient, $\mu(E)$, is measured as a function of energy. As the energy of the incoming X-ray photons increases, $\mu(E)$ decreases exponentially. From the minimum to maximum value of the energy range, there is an abrupt increase known as the absorption edge, which is a characteristic of the absorbing element and related to excitation of the core electrons. The physics behind XAFS is a quantum mechanical phenomenon based on the photoelectric effect (see Figure 2.1.5.1(a)). Incident X-ray photons promote electrons from a core shell, such as K shell, to the continuum, which creates an interference pattern between the outgoing and scattered (from surrounding atoms) parts of photoelectron wavefunction. In the XAS method, X-ray absorption near edge structure (XANES) and extended X-ray absorption fine structure (EXAFS), as shown in Figure 2.1.5.1(b), are studied separately. More details about XANES can be found in the textbook "Introduction to XAFS: A practical guide to X-ray Absorption Fine Structure Spectroscopy", (Bunker, 2010), which gives a broad introduction of the field. The following parts will focus on EXAFS only.

### 2.1.5.1. Extended X-ray Absorption Fine Structure (EXAFS):

The typical starting region for EXAFS is 20-30 eV above the absorption edge jump, as circled in Figure 2.1.5.1(b). At this range of energies, X-ray photoelectrons have a wavelength comparable with interatomic distances, which then forms constructive interference between outgoing and scattered X-rays and local maximum in the absorption coefficient. In the same way, at higher energies, the photoelectrons have higher energy (shorter wavelength), causing local minimum in the absorption coefficient due to destructive interference.

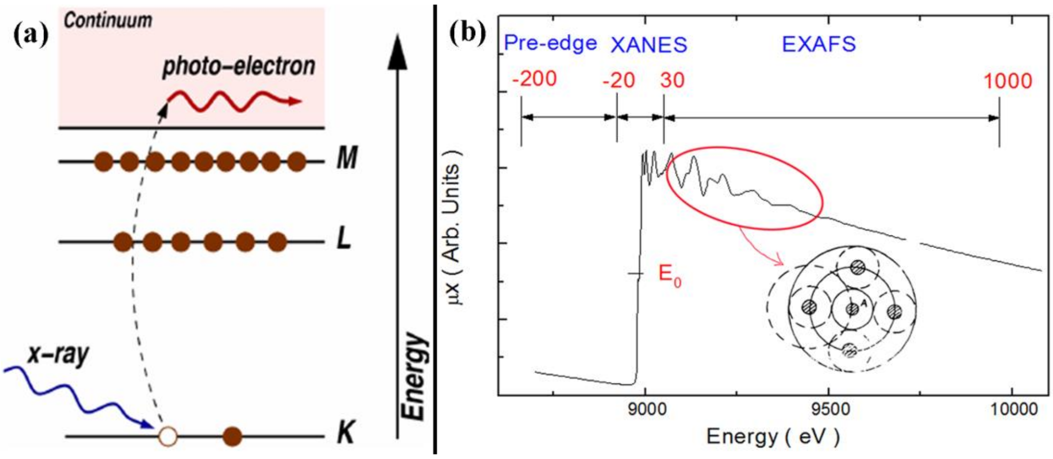

**Figure 2.1.5.1** (a) Schematic of an X-ray absorption event in which core-level electron is promoted out of atom after an X-ray is absorbed. (b) An example of XAFS spectrum: Pre-edge, X-ray absorption near edge structure (XANES) and extended X-ray absorption fine structure (EXAFS). (Taken from references (Newville, 2004) and (Zhang, 2013) respectively.)

In XAS analysis, EXAFS function, $\chi(k)$ is defined as a fraction, given in Equation 2.1.5.1, between the observed absorption coefficient, $\mu$ and the absorption coefficient, $\mu_0$ of an isolated atom (i.e. free of EXAFS effects).

$$\chi(k) = \frac{\mu - \mu_0}{\mu_0}$$ Equation 2.1.5.1

$\mu_0$ is approximated usually using a smooth spline function due to fact that it can almost never be measured directly.

The expression given in Equation 2.1.5.2 is known as the standard EXAFS equation derived by Stern, Sayers and Lytle (Stern, Sayers, & Lytle, 1975).

$$\chi(k) = \sum_i \frac{N_i A_i(k) S_0^2}{kR_i^2} e^{-2R_i/\lambda(k)} e^{-2k^2\sigma_i^2} \sin(2kR_i + \phi_i(k)) \qquad \text{Equation 2.1.5.2}$$

where $N_i$ is the number of neighbours (coordination number); $S_0^2$ is for scattering amplitude attenuation (or amplitude reduction factor); $A_i(k)$ is the backscattering amplitude term from each of the $N_i$ neighbouring atoms; $\sigma_i^2$ is known as the root-mean square deviation (RMSD) value from $R_i$ and contributes to Debye-Waller factor ($e^{-2k^2\sigma_i^2}$), which stands for the vibration of the atoms; $R_i$ is the absorber-scatterer distance; $\lambda(k)$ is the electron mean free path; and $\phi_i$(k) within sine function is the phase difference between outgoing and back-scattered light. Through the curve fitting using FEFF code (Ankudinov, Rehr, & Conradson, 1998) and a software programme called Demeter (Newville, 2001; B Ravel & Newville, 2005), these parameters can be extracted.

The steps followed in the fittings of all the EXAFS measurements [5] can be listed as follows:

- Background removal from the measured EXAFS data is the first step and is generally performed by an Autobk algorithm determined by some initial parameters. (ATHENA)
- Normalisation process is followed after the background removal, which is used for removing variations due to sample preparation, thickness and other aspects of the measurement. (ATHENA)
- Generate the scattering paths based on a particular structural model, which we consider the sample can be. (ARTEMIS)

---

[5] See Appendix on page 127 for a step by step procedure as followed in the EXAFS data analysis.

- Choosing a number of the relevant structural parameters. (ARTEMIS)
- Refining these parameters in order to perform the fittings. (ARTEMIS)

### 2.1.5.2. Optically-Detected Extended X-ray Absorption Fine Structure (OD-EXAFS) Using X-ray Excited Optical Luminescence (XEOL):

OD-EXAFS is one of the experimental methods of collecting EXAFS. It is based on X-ray excited optical luminescence (XEOL) emission being sensitive to the absorption events (see Figure 2.1.5.2). Thus an EXAFS signal can be extracted by collecting integral light emission as a function of incident X-ray energy. This method allows the linking of optical emission with underlying atomic structure contributing to the emission under certain circumstances. Figure 2.1.5.2 depicts X-ray excitation followed by photoluminescence, which is structurally recorded as OD-EXAFS.

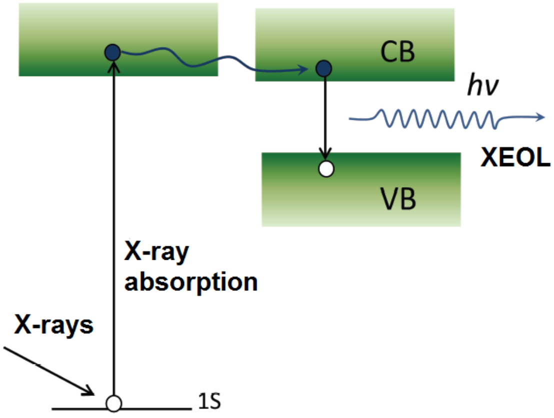

**Figure 2.1.5.2** Scheme of X-ray excitation-photoluminescence cycle in OD-EXAFS. An excitation from 1S state to continuum followed with luminescence, which is linked, to structure (OD-EXAFS).

The instrumentation of EXAFS and OD-EXAFS using XEOL is demonstrated in Figure 2.1.5.3. OD-EXAFS and EXAFS, including simultaneous

XEOL measurements of the same area for each sample, have been conducted at beamline B18 at Diamond Light Source at the Rutherford Appleton Laboratory in the UK. The equipment for OD-EXAFS includes a spectrometer equipped with a photomultiplier tube (Hamamatsu R3809U-50 MCP), in order to record the X-ray emitted luminescence, in addition to an X-ray detection system (more details given in our study (Karatutlu *et al.*, 2013)). The Ge K-edge was studied for OD-EXAFS and EXAFS, as a function of energy over the range of 11.05-12 keV. XEOL measurements were collected from the same area as a function of wavelength centred at 700 nm for each set of the samples.

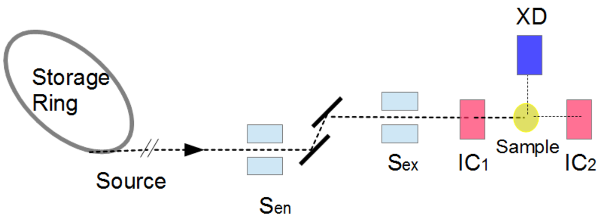

**Figure 2.1.5.3** The schematic of X-ray absorption spectroscopy measurements (EXAFS, OD-EXAFS and XEOL) was shown using station B18 at Diamond Light Source at the Rutherford Appleton Laboratory in the UK. In the scheme, the synchrotron radiation XAFS experiment is depicted as being combined with a simultaneous recording of a XEOL measurement from the same area of the sample. [6]

The EXAFS samples were prepared in two different ways. The samples formed using stain etching, LP-PLA and the sol-gel method were prepared as

---

[6] $S_{en}$ and $S_{ex}$ are entrance and exit slits, $IC_1$ and $IC_2$ are the ionisation chambers, XD refers to the X-ray excited optical luminescence (XEOL) detector which is the spectrometer mentioned above in the text. The XEOL is collected using an optical fibre and directed to the spectrometer. Transmission EXAFS part of the scheme was reproduced from reference (Welter, 2003).

pellets[7]. The samples formed using the colloidal synthesis routes were placed inside a glass capillary as shown in Figure 2.1.4.3.

## 2.2. Sample Preparation Methods

In this section, experimental methods such as chemical stain etching, liquid phase pulsed-laser ablation, the sol-gel method and the benchtop colloidal synthesis routes are described.

### 2.2.1. Chemical Stain Etching

Chemical stain etching is one of the methods used for producing visible luminescent nanoparticles from semiconductors (Karavanskii *et al.*, 2003). There are a few differences between the chemical etching process and the electrochemical etching (anodisation) process. In the case of stain etching, there is no need to apply a bias[8]. The samples can be produced simply by exposing their surface to the chemical stain etching solution.

Since Turner (Turner, 1960), an aqueous HF/$HNO_3$ solution has been used electrochemically as an etchant for Si and Ge. Additionally, using an aqueous HF/$HNO_3$ solution with a volume ratio of 500:1 respectively was shown in chemical stain etching of Si (Abramof, Beloto, Ueta, & Ferreira, 2006).

---

[7] The pellets were prepared using a manual pellet press with a 1.3 cm die under an 8 ton press. Each of the dried (using Ar gas) powder of the samples (30 mg each) were mixed with boron nitride powder (70 mg) (provided by Diamond Light Source).

[8] Particularly in the earlier studies, HF solution was utilised together with the help of a current source to alter the size of the nano-pores. (see (Canham, 1990) for more information.)

Nevertheless, samples produced using HF/$HNO_3$ solution was reported to have a low photoluminescence yield (Kelly, Chun, & Bocarsly, 1994).

Thus, in addition to $HNO_3$, the attention of researchers turned to one of the well-known oxidizing agents: hydrogen peroxide ($H_2O_2$). In one of the key studies (Karavanskii *et al.*, 2003), stain etching of the n-type Ge wafer was performed under indoor light illumination for 3 hours in a solution of HF:$H_3PO_4$:$H_2O_2$ (34:17:1). This volume ratio does not work for bulk Ge in powder form.

Chemical stain etching of bulk Ge powder was performed using a solution of HF:$H_3PO_4$:$H_2O_2$ (200:200:1)[9]. Hydrofluoric acid, HF (48 wt. % in $H_2O$) [10], phosphoric acid, $H_3PO_4$ (85 wt. % in $H_2O$) and hydrogen peroxide (30 wt. % in $H_2O$) were used as-purchased from Sigma-Aldrich. The solution was stirred inside a PTFE cell for 3 hours under indoor light illumination[11]. The schematic in Figure 2.2.1.1 illustrates the processes in stain etching. Germanium powder (over 99.999 % purity [12]) was used as purchased from Sigma-Aldrich in the solution from Sigma-Aldrich. A PTFE-coated octagonal magnetic bar was used to stir the solution with a particular speed. In order to find the right amount from each chemical mentioned

---

[9] The volumes of 15 ml:15 ml:0,075 ml were used in the experiment for HF:$H_3PO_4$:$H_2O_2$ respectively. The optimum conditions were discovered at the end of 115 trials of the various amounts of the chemicals. The amount of $H_2O_2$ in the solution is particularly important: if it exceeds 0.075 ml of $H_2O_2$ it may quickly cause the dissolution of the sample.

[10] Take extreme caution whilst dealing with HF acid solution. See material safety data sheet, MSDS – 339261 in Sigma-Aldrich for the standard operating procedure and risks.

[11] Exposing the reaction cell to different light sources, such as UV, may affect the conditions.

[12] It may also contain some degree of natural oxides since the sample container was stored in a chemical storage cupboard in an ambient environment.

above, the trials were performed using a speed of 80 rpm[13]. After finding the optimum conditions at 80 rpm (sample B), the effect of the agitation speed by increasing to 120 rpm (sample A) was investigated to some extent. Nevertheless, due to the fact that the main effort in the sample preparation of stain etching was given to sample B, sample B was chosen as the sample, which was taken to the synchrotron for further investigation.

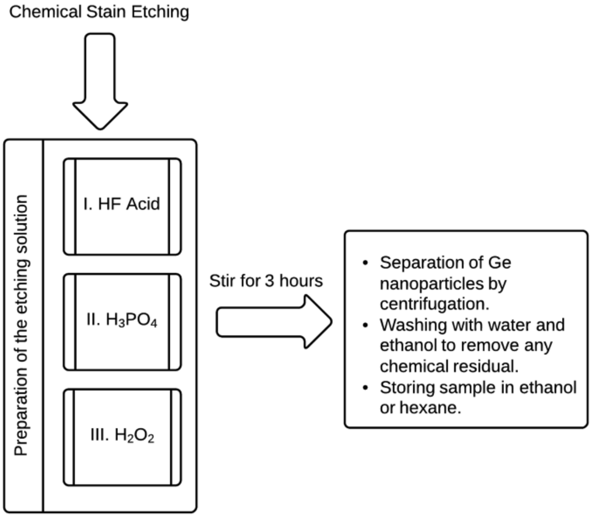

**Figure 2.2.1.1** The schematic of the stain etching process. Ge nanocrystals were formed via etching using a solution of HF, phosphoric acid and hydrogen peroxide for 3 hours.

After formation of the Ge nanoparticles, the sample colour was transformed from black to yellow at the end of 3 hours. The picture of Ge nanoparticles formed using the stain etching is shown in Figure 2.2.1.2(b). The picture of crystalline bulk Ge is also shown for comparison in Figure 2.2.1.2(a).

---

[13] The PTFE coated magnetic bar and the magnetic stir plate used are available from Sigma-Aldrich.

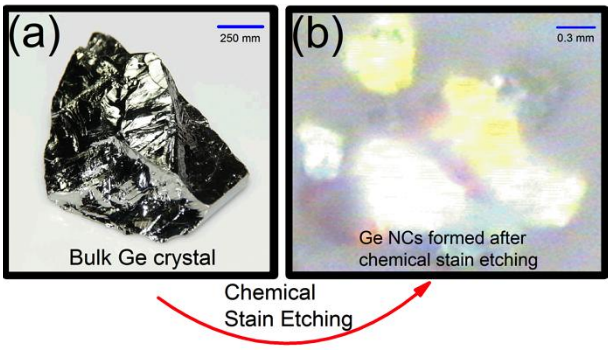

**Figure 2.2.1.2** Picture of (a) Crystalline bulk Ge (b) Ge nanocrystals formed using stain etching. (Picture of bulk Ge was taken from reference ("Crystalline Bulk Ge," 2013).) The scale bars (both with blue colour) in (a) and (b) have the size of 250 mm and 0.3 mm respectively. The picture (b) was taken using an optical microscope attached to a Renishaw 1000 spectrometer.

## 2.2.2. Liquid Phase Pulsed-Laser Ablation (LP-PLA)

Laser ablation became available after the invention of the ruby laser in the 1960s (Maiman, 1960). Since the 1980s, it has been used to form a wide range of nanomaterials in ambient conditions (Yang, 2007), in gas (Seo *et al.*, 2006) or in liquid phase (Semaltianos *et al.*, 2009). Laser ablation of a target immersed in a liquid has been known about since 1987 when Patil and co-workers ablated pure iron in liquid ammonia for nitridation of iron (Ogale, Patil, Roorda, & Saris, 1987), and has been used successfully to produce photoluminescent silicon nanoparticles (Umezu, Minami, Senoo, & Sugimura, 2007) with a possibility of tuning their size (Semaltianos *et al.*, 2009). In laser ablation, when laser light interacts with the target, an ablation plume is formed (Yang, 2007). The ablation plume consists of species of the bulk target in the form of atoms, ions and molecules expanding to the environment around the target with a very high kinetic energy. If the ablation is performed inside a suitable liquid-host that would not be absorbing the laser light, then the expanding species can interact and form nanoparticles composed of atoms both from the target and the liquid, with the benefit of a colloidal solution of nanoparticles as the product (Amendola & Meneghetti, 2013). The extreme temperatures and pressures attained at the target-liquid interface may result in the generation of a variety of species such as vapour of the solid target with some amounts from the surrounding liquid (Yang, 2007). It is possible that the size as well as morphology of the nanoparticles may be affected by altering the liquid-host, wavelength and time of ablation. Some investigations have been carried out with silicon (Semaltianos *et al.*, 2009; Takada, Sasaki, & Sasaki, 2008), but, as yet, only a little work has been done using germanium (Jiang, Liu, Liang, Li, & Yang, 2011).

Bulk germanium powder (over 99.999 % purity), purchased from Sigma-Aldrich was used as the target material. The laser was an Nd:YAG laser (Surelite I-10), as schemed in Figure 2.2.2.1. Using a combination of dichroic mirrors, the beam was focused to an area of 4x1 mm$^2$ inside a quartz cuvette. The laser power and wavelength were set at 108 mJ and 355 nm. The pulse frequency was 1 Hz and the pulse duration was around 13 ns. A quartz cuvette contained 18 mg of the bulk germanium powder and liquid hexane to a depth of 1.5 mm. The cuvette (4.5x1.25x1.25 cm) was purchased from Sigma-Aldrich and washed with deionised water and ethanol several times then dried with Ar gas before conducting the experiment.

Ablation in the hexane was carried out for various lengths of time, however, the minimum amount of time to produce a sufficient amount of sample that can be used for further characterisation studies was found to be 7 hours. The hexane was allowed to fully evaporate before suspending the residue in ethanol. Centrifuging at 13000 rpm was used to separate the produced sample from the original target material.

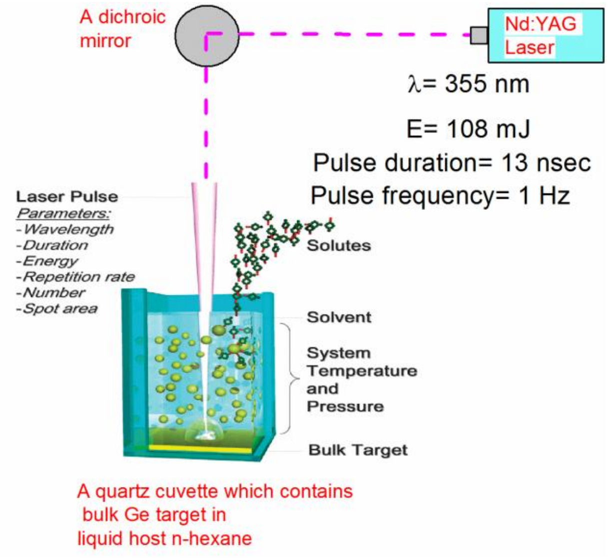

**Figure 2.2.2.1** The schematic of the experimental configuration of liquid phase pulsed-laser ablation (LP-PLA) conducted in this section. The Nd:YAG laser with a wavelength of 355 nm, an energy of 108 mJ, a pulse duration of 13 ns and a pulse frequency of 1 Hz was focused on bulk Ge target in liquid host n-hexane using a dichroic mirror. (The scheme of the cuvette was taken from reference (Amendola & Meneghetti, 2013)).

Ge nanoparticles formed via LP-PLA are shown in Figure 2.2.2.2. The cluster of Ge nanoparticles is represented in a grey (creamy white) colour and marked by red arrows.

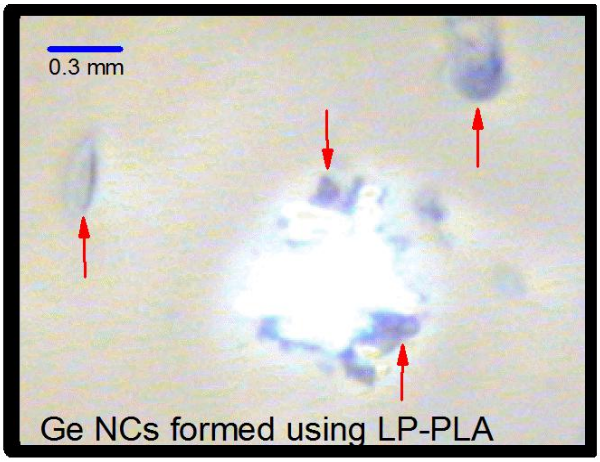

**Figure 2.2.2.2** Picture of Ge nanocrystals formed using LP-PLA at the end of 7 hours ablation process. The scale bar (blue in colour) is 0.3 mm in size. The picture was taken using an optical microscope attached to a Renishaw 1000 spectrometer.

### 2.2.3. The Sol-Gel Method

The flexibility of the sol-gel route makes it possible to produce the final material as powders, bulk and coating films (Henderson, Seino, *et al.*, 2010). In most of the nano-fabrication methods, the main reason to use a method is to be able to control the size of nano-clusters (Nogami & Abe, 1997). Furthermore, a surrounding matrix surrounding Ge nanocrystals, such as silica, can provide Ge nanocrystals with an environment of protection so as to preserve its unique physical properties, including optical, and can be useful in devices such as optical switches and waveguides (Hayashi *et al.*, 1990). Furthermore, the choice of precursors can give Ge nanoparticles embedded in different surrounding matrices (Veinot *et al.*, 2009). For instance, TEOS and TEOG can produce Ge nanocrystals embedded in a silica matrix (Henderson, Seino, *et al.*, 2010). At the end of the sol-gel reactions, through co-hydrolysis and co-condensation processes, the oxide enriched co-polymer such as $(GeO_2)_x(SiO_2)_y$ can be obtained (Yang *et al.*, 2002). Then, thermal processing of $(GeO_2)_x(SiO_2)_y$ co-polymers in inert (Ar) or reducing ($H_2$(5 %)/Ar(95 %)) atmosphere results in diffusion of Ge atoms inside silica matrix and formation of Ge nanocrystals (Henderson, Hessel, Cavell, & Veinot, 2010).

Ge nanocrystals embedded in $SiO_2$ were formed by reductive thermal processing of sol-gel glasses obtained from a mixture of tetraethoxyorthogermanate (TEOG, 99.95 %) and tetraethoxyorthosilicate (TEOS, 98 %) following the method given in the reference (Henderson, Seino, *et al.*, 2010). The key steps of sol-gel synthesis of Ge nanoparticles embedded in silica ($SiO_2$) are shown in Figure 2.2.3.1. Three successive processes were used: preparation of the gel, then 48 hours of heating treatment at 100 °C and 3 hours of heating treatment at 600 °C in air, followed by a heating treatment in $H_2$(5%)/Ar(95%) medium at 700 °C. When preparing the gel, the amount of precursors such as TEOG and TEOS determines the stoichiometric ratio between $GeO_2$ and $SiO_2$ as well as the size of the Ge nanocrystals.

In a typical synthesis of the gel, 0.728 g of TEOG, 4.2 g of TEOS, and 8 ml of anhydrous ethanol was mixed for 30 minutes. After adding 4 ml of HCl acid (37 %) the colourless solution turns a cloudy white colour. At the end of 48 hours, the gel of $(GeO_2)_{25}(SiO_2)_{218}$ was obtained (see Figure 2.2.3.2). Then heat treatment in air at 100 °C was applied for an additional 48 hours. Via this process, a powder of the $(GeO_2)_{25}(SiO_2)_{218}$ [14] was formed. For total drying of the sample, 3 hours additional heating treatment at 600 °C in air was applied.

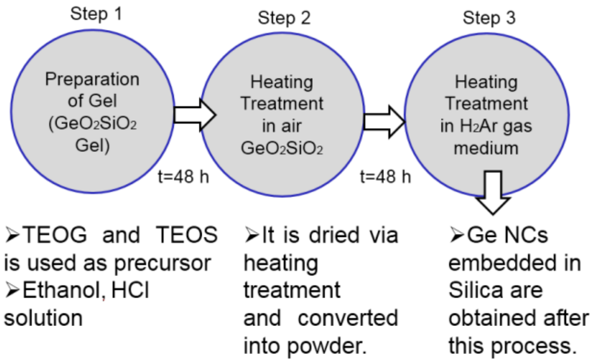

**Figure 2.2.3.1** The schematic of the sol-gel method. Successive methods such as preparation of the gel, $GeO_2SiO_2$ powder and formation of Ge nanocrystals embedded in $SiO_2$ were followed.

---

[14] The stoichiometric ratio was determined using the EDX result of the Ge nanoparticles embedded in silica given in page 85.

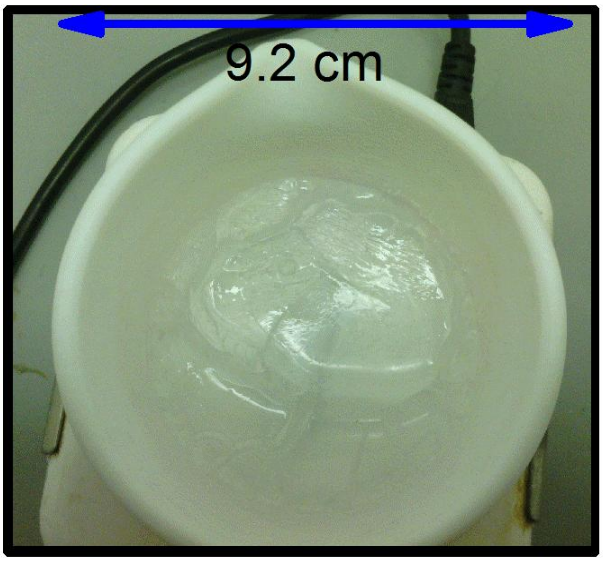

**Figure 2.2.3.2** At the end of 48 hours, the gel of $(GeO_2)_{25}(SiO_2)_{218}$ was obtained inside the PTFE beaker (white colour). The scale bar (blue in colour) is 9.2 cm in size, which is equivalent to the diameter of the PTFE beaker.

The colour of the $(GeO_2)_{0.125}(SiO_2)_{0.825}$ co-polymer at the end of step 2 is white (see Figure 2.2.3.3(a)). In order to remove oxides from Ge and let Ge atoms diffuse inside the $SiO_2$ matrix, $(GeO_2)_{25}(SiO_2)_{218}$ sample was heated for 3 hours at 700 $^oC$ in a medium of $H_2$(5%)/Ar(95%). At the end of the heating treatment in $H_2$(5%)/Ar(95%) gas medium, the colour of the sample turns pale brown depending on the size of the Ge nanocrystals (see Figure 2.2.3.3(b)).

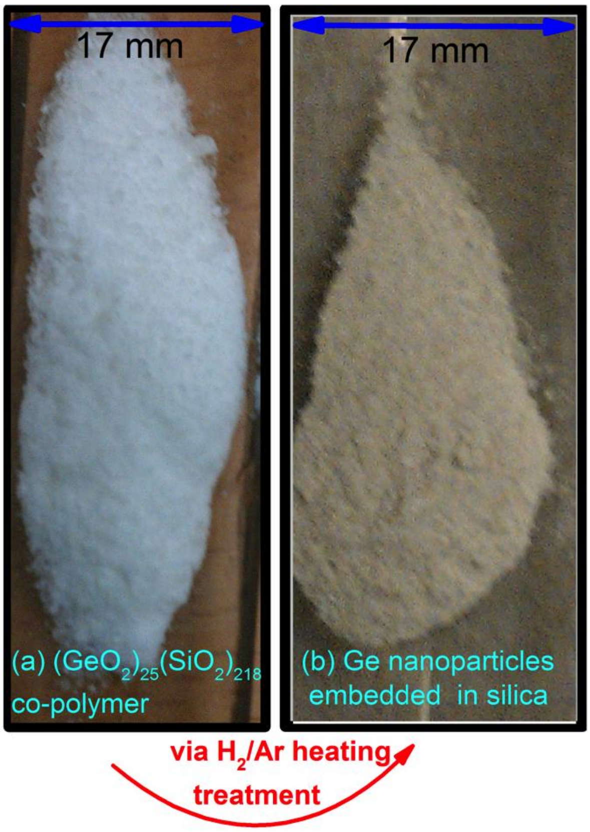

**Figure 2.2.3.3** Picture of samples produced using the sol-gel method: (a) $(GeO2)_{25}(SiO2)_{218}$ co-polymer (b) Ge NCs embedded in silica matrix. The pictures were taken using an HTC Desire HD cellular phone. Pale brown sample in (b) may be considered as an indication for the formation of Ge nanoparticles.

The luminescent picture (taken by an epi-fluorescent microscope with the excitation of $\lambda_{exc} = 350$ nm) of Ge nanocrystals embedded in silica synthesised using the sol-gel method is shown in Figure 2.2.3.4.

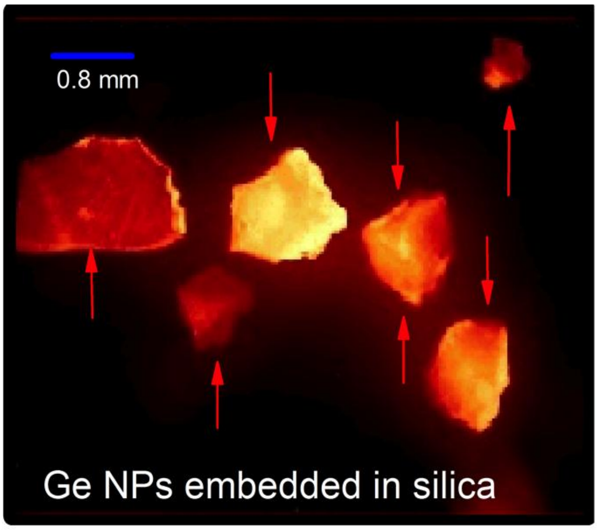

**Figure 2.2.3.4** Luminescent picture of Ge nanocrystals embedded in silica (red in colour) formed using the sol-gel method. The scale is 0.8 mm in size.

## 2.2.4. Colloidal Synthesis Routes

A variety of routes for the preparation of colloidal semiconductors was studied in the 1980s, including CdS, ZnS and ZnO (Koch, Fojtik, Weller, & Henglein, 1985). In the 1990s, after observation of the room temperature light emission from Si (Cullis & Canham, 1991), the solution phase synthesis of Si (Heath, 1992) and that of Ge (Heath *et al.*, 1994) were observed. However, they observed that some of the sample oxidized despite the fact the experiment was carried out in a glove box and transferred to a sealed pressure bomb. Then, Taylor *et al.* (Taylor *et al.*, 1999) used NaGe reduction to obtain Ge nanoparticles, but this method also has its drawbacks, such as removing excess Na after the formation process using a high-vacuum line at 300 $^{o}$C for 4 hours. Recent reports, particularly around reducing halides ($GeI_2$/$GeI_4$ (Ruddy *et al.*, 2010; Vaughn *et al.*, 2010) or $GeCl_4$ (Chou *et al.*, 2009)) and oxides ($GeO_2$ (Wu *et al.*, 2011)), have received a great deal of attention. However, the methods for reducing iodine-based halides require the use of a Schlenk line at high temperature. The light emission from Ge nanoparticles synthesised using $GeI_2$/$GeI_4$ reduction was claimed to be due to the quantum confinement (size) effect in the near-infrared region (from 1.6 eV to 0.7 eV) (Ruddy *et al.*, 2010).

#### 2.2.4.1. The Benchtop Colloidal Synthesis I: Formation of Ge Nanoparticles by Reduction From $GeCl_4$

Ge nanoparticles were synthesised by utilising a bench-top colloidal synthesis route (Chou *et al.*, 2009) which forms Ge nanoparticles suspended in water and ethanol. Initially, 265 μL of $GeCl_4$ was dissolved in a solution of 10 mL of ethylene glycol and 50 mg of polyvinylpyrolidone (PVP, MW =630.000). Then, 6 mL of 2 M of $NaBH_4$ in triethylene glycol dimethyl ether (used as $NaBH_4$ solution henceforth) was added at a rate of 90ml/hour for the first 2 ml and then 9 ml/hour for the remaining 4 ml. As depicted in Figure 2.2.4.1, this controlled addition process for the $NaBH_4$ solution was performed with a syringe pump[15] into a 3 neck round bottom beaker in which the solution was bubbled using a continuous Ar (or $H_2$/Ar(5%/95%)) flow with an inlet of a micro-tube through the solution (see also Figure 2.2.4.2(a)). All the chemicals were used as-purchased from Sigma-Aldrich. The formation process took approximately one hour[16] and the final product was separated from the colloidal chemical solution by 10 minutes of centrifugation at

---

[15] The Alaris IVAC P3000 syringe pump and B-D Plastipak (20 ml) syringes were used in the synthesis. The syringe pump and the 20 ml syringes are commercially available from companies called Carefusion and BD respectively.

[16] A one hour reaction time was chosen initially, using intuition, and after a pre-investigation of the as-prepared sample using Raman spectroscopy, photoluminescence spectroscopy and TEM measurements, it was kept constant.

10,000 rpm. Increasing the $GeCl_4$ concentration causes the Ge nanoparticles to grow in size. In addition to changing the $GeCl_4$ concentration, annealing in $H_2$/Ar (5%/95%) or Ar gas medium with a flow rate of 100 ccm can also increase their size and modify their surface. These samples of Ge nanoparticles (produced with 265 μL of $GeCl_4$, produced with 300 μL of $GeCl_4$, annealed in $H_2$/Ar (5%/95%) gas) are referred to in the following section as $CS_1$, $CS_2$ (as-synthesised) and $CS_1$-$H_2$Ar (annealed) respectively. We used annealing as a way of controlling particle size and crystallinity. Ge nanoparticles formation via $CS_1$ was modified so that $H_2$/Ar (5%/95%) gas was used to purge the chemical preparation solution instead of Ar gas, in order to remove any possible oxide formation in as-prepared samples. Ge nanoparticles prepared via purging of $H_2$/Ar (5%/95%) gas were named $CS_1$-$H_2$.

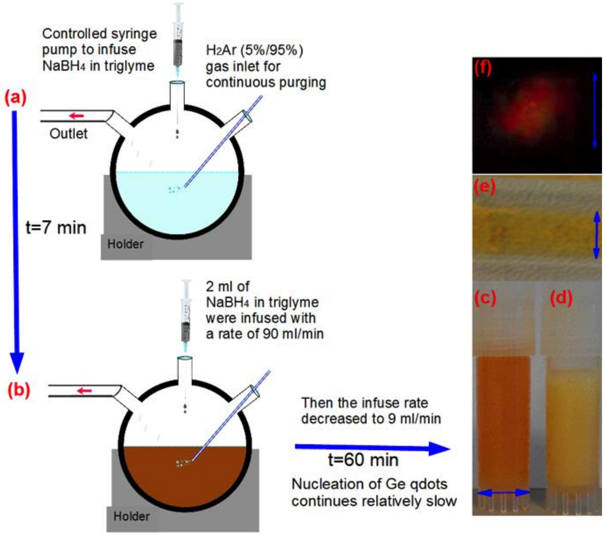

**Figure 2.2.4.1** The schematic of experimental configuration. From (a) to (b), the addition rate of $NaBH_4$ in triglyme was decreased from 90 ml/min to 9 ml/min. (c) Picture of Ge nanoparticles as prepared ($CS_1$) suspended in chemical solution just after formation and (d) in ethanol after separation of Ge nanoparticles from chemical residual by 13000 rpm. (e) Ge nanoparticles powder dried on a quartz boat using Ar gas. (f) Photoluminescence picture of Ge nanoparticles with an excitation of 442 nm laser light. Scale bars (all with blue colours) in (c), (e) and (f) are 10 mm, 17 mm and 0.75 mm respectively.

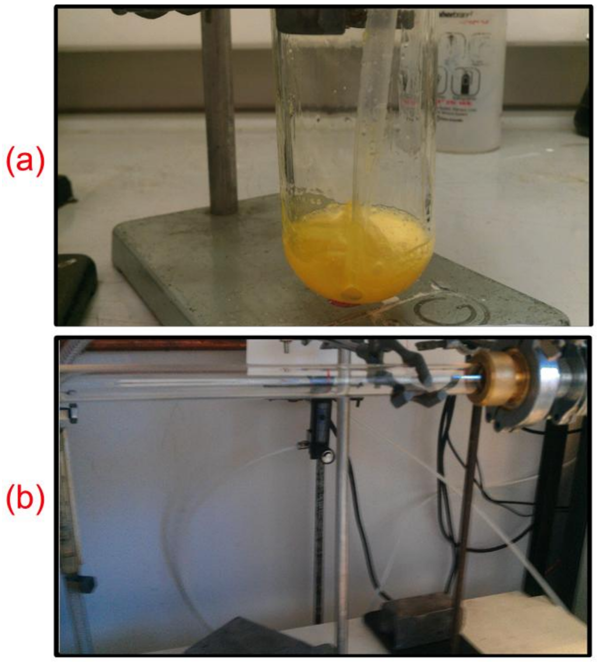

**Figure 2.2.4.2** (a) Picture of Ge nanoparticles formed by colloidal synthesis ($CS_1$ and $CS_1$-$H_2$) (b) Picture of experimental configuration for annealing of as-prepared Ge nanoparticles with a flow of $H_2$/Ar ($CS_1$-$H_2$Ar) gas. In (a), a 100 ml three-neck beaker was used. In (b), as-prepared sample dropped on a quarzt boat (10 cm length) used for annealing inside a quartz tube with a diameter of 1.5 cm and a length of 56 cm via a split furnace.

### 2.2.4.2. The Benchtop Colloidal Synthesis II: Formation of Ge Nanoparticles by Reduction of $GeO_2$

The second method of the benchtop colloidal synthesis was utilised to form germanium nanoparticles by decomposition of $GeO_2$ (Wu *et al.*, 2011) at 60°C, at ambient pressure with an adaptation of a syringe pump (see sample preparation in page 51) to control the size of Ge qdots and to cease the reaction at a particular moment. All the chemicals were purchased from Sigma-Aldrich and used as purchased without any purification. In a typical experiment, 26 g of $GeO_2$ powder ($\geq$ 99%) was dissolved in 0.01 g of polyvinylpyrolidine (PVP, MW=630.000) and 10 ml of 0.15 M of NaOH solution. Then, 0.5 ml of 0.5 M HCl acid solution was added to the flask in order to increase the pH to 7.0. The solution at this point is colourless and transparent. Heating the solution begins with the initiation of the formation of Ge nanoparticles by a controlled addition rate, such as 20 ml/h of 10 ml of 0.75 M of $NaBH_4$ in triethylene dimethyl glycol ether via the syringe pump. So, the original recipe was modified using a controlled addition of the $NaBH_4$ solution instead, using only $NaBH_4$. Over 30 min, the colour of the solution changed from colourless (see Figure 2.2.4.3(a)) (no $NaBH_4$ solution added yet) to yellow (sample $Ca_{1a}$, see Figure 2.2.4.3(b)) (1 ml of $NaBH_4$ solution added), then brown (see Figure 2.2.4.3(c)) and at the end, dark brown (sample $Ca_{1d}$, see Figure 2.2.4.3(f)), referring to the reduction of $GeO_2$ then growing Ge nanoparticles via nucleation. The formed Ge nanoparticles were separated from chemical residue using centrifugation at 10000 rpm, washed with ethanol several times and stored in ethanol. The evolution of formed Ge nanoparticles (stored as suspended in ethanol) after separation from the chemical residua was also demonstrated in Figure 2.2.4.4. The Ge nanoparticles can be suspended in ethanol or kept in hexane for more than a month.

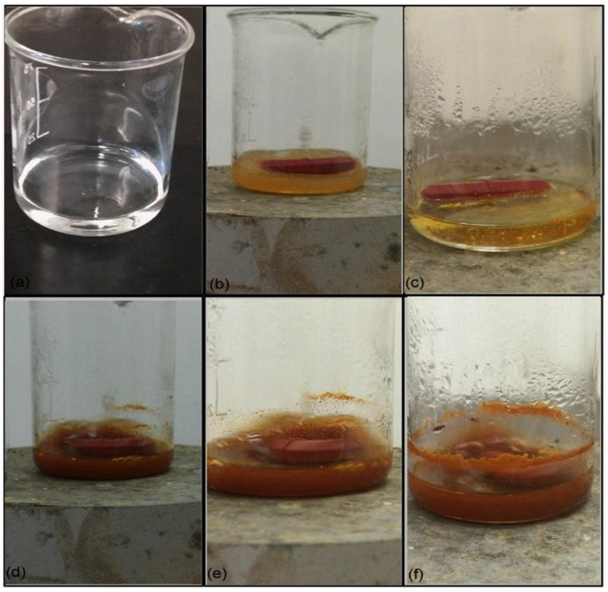

**Figure 2.2.4.3** From (a) to (f), the evolution of Ge nanoparticles formed inside a 100 ml Pyrex beaker using the benchtop colloidal synthesis method II.

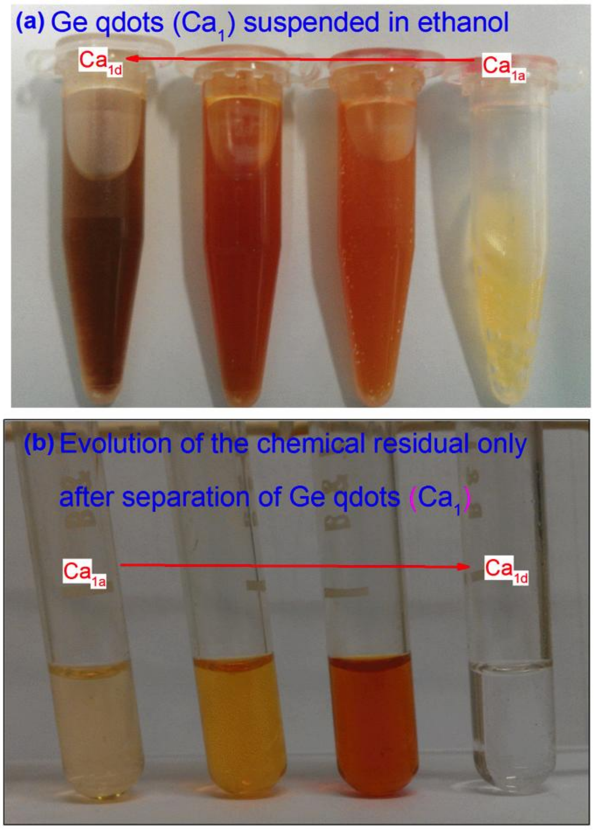

**Figure 2.2.4.4** (a) The evolution of Ge qdots using the benchtop colloidal synthesis method II ($Ca_1$). From $Ca_{1a}$ to $Ca_{1d}$, the size of Ge qdots changes their colour respectively from yellow to dark brown in accordance with the size of Ge qdots. (b) The evolution of the chemical residue was shown after separated from Ge qdots using centrifugation at 10000 rpm.

# CHAPTER 3. RESULTS AND DISCUSSION

In the initial part of this chapter, the results of the structural, morphological and optical properties of Ge nanoparticles formed by stain etching, LP-PLA and the sol-gel method are discussed, with comparisons to the previous studies. Raman spectroscopy was used as a first analytical tool to verify the structure and the size of Ge nanoparticles according to the phonon confinement model (Campbell & Fauchet, 1986; Richter *et al.*, 1981). Photoluminescence spectroscopy was used in order to determine the optical properties of as-prepared samples. TEM micrographs were used to find out the size and the shape of Ge nanoparticles. After these investigations, samples were studied using XAS measurements. EXAFS and OD-EXAFS including XEOL were recorded at the Ge K edge of the Ge nanoparticles. This work is followed by detailed studies of samples prepared by colloidal synthesis methods and XRD was used in addition to optical and EXAFS techniques.

## 3.1. Chemical Stain Etching

### 3.1.1. Raman and PL Spectroscopy

The Raman shift of bulk Ge before chemical stain etching was collected for a reference, and the peak position with symmetry is centered at 300.61 ± 0.02 $cm^{-1}$ as given in Figure 3.1.1.1. This is consistent with previous calculations and experimental measurements ( $\omega$ =300.6 $cm^{-1}$, (Malone & Cohen, 2012)).

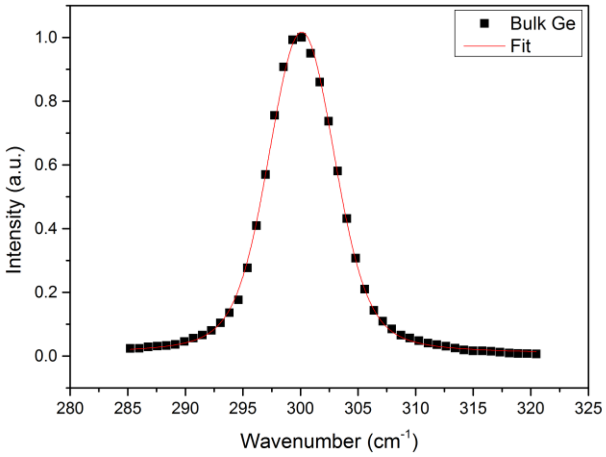

**Figure 3.1.1.1** Raman shift of reference bulk Ge powder as purchased from Sigma-Aldrich. The fit was performed using a Voigt function which is a perfect convolution of Lorentz and Gaussian distributions (Gouadec & Colomban, 2007). The peak position and the FWHM of bulk Ge is 300.61 ± 0.02 cm$^{-1}$ and 6.86 ± 0.06 cm$^{-1}$ based on Voigt fit.

Using chemical stain etching (see sample preparation on page 40), there were two different samples (sample A and sample B) produced with a faster agitation speed (A) and slower speed (B), at 120 rpm and 80 rpm respectively. In Figure 3.1.1.2, the Raman spectra collected from sample A and sample B are shown. Sample A shows as a larger shift in the Raman peak position (12 cm$^{-1}$, compared to the peak frequency of bulk Ge centered at 300 cm$^{-1}$) than that for sample B (7 cm$^{-1}$). It is also obvious that both of the spectra have the asymmetric broadening observed in previous studies (Kartopu, Bayliss, Hummel, & Ekinci, 2004; Wu *et al.*, 1997), which is also one of the well-known characteristics of nanocrystals.

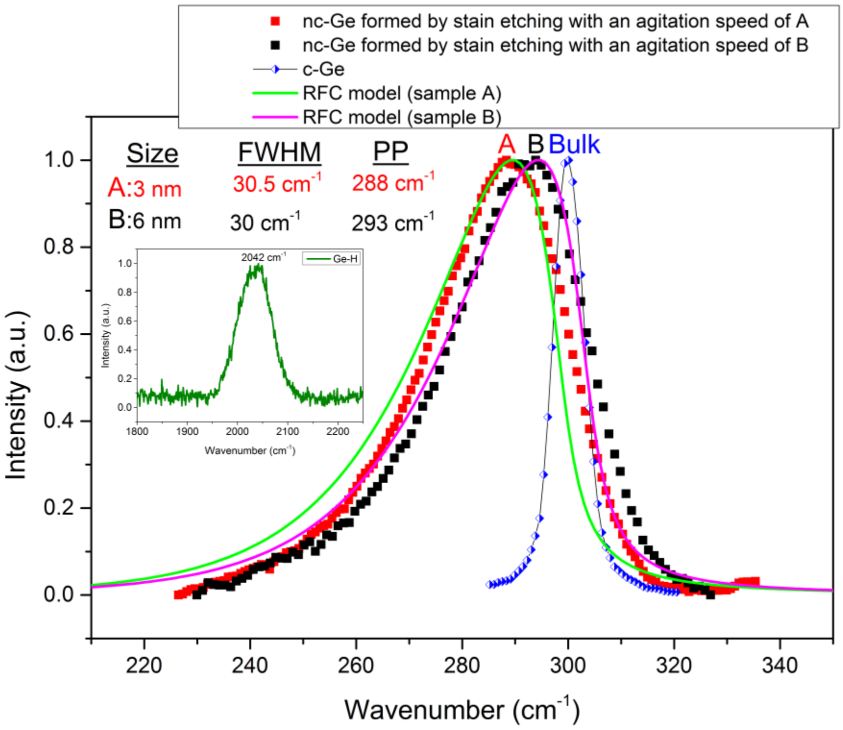

**Figure 3.1.1.2** Raman shift of sample A and sample B with a faster agitation speed, 120 rpm, and a slower agitation speed, 80 rpm respectively. The size of each sample was determined using the phonon confinement model developed by Campbell and Fauchet (Campbell & Fauchet, 1986). The calculations were estimated based on the peak positions instead of FWHM. The sizes of sample A and sample B were estimated to be 3.0 nm and 6.0 nm with a 0.3 nm uncertainty. Raman shift of c-Ge (blue colour) is also shown for comparison. The inset shows a broad peak at 2042 cm$^{-1}$ assigned to hydride termination of Ge nanoparticles (Choi & Buriak, 2000). RFC fittings to the data are also shown.

Using the phonon confinement model[17] (Campbell & Fauchet, 1986; Richter *et al.*, 1981), the mean size of each sample was found to be 3 nm for sample A and 6 nm for sample B respectively (see .

We also recorded extended Raman spectra for both samples in order to check possible presence of germanium hydrates and oxides. The inset in Figure

---

[17] Equation 2.1.1.1 given for the phonon confinement model seen on page 25 was applied to get the size.

3.1.1.2 shows a peak at 2042 $cm^{-1}$ observed in the extended spectra which we ascribed to a vibration associated with the Ge-H bond.

Kipphardt reported (Kipphardt *et al.*, 1999) that $GeO_2$ could react with HF to form hexafluorogermanic acid[18], $H_2GeF_6$. On the other hand, $GeO_2$ in its alpha-quartz phase and amorphous phase is known to be soluble in water [19] (Rojas, 2010). Hence, the process of etching is quite complex due to simultaneously occurring competition for the Ge dissolution. The model of the dissolution of Ge by a highly concentrated HF acid adapted by Garralaga Rojas, Enrique in 2010 may also be considered for the formation of H-terminated Ge nanoparticles. The process starts with $H_2O_2$ which can lead to oxide formation on the surface of bulk Ge. Then, HF acid can remove oxide and thus result in the dissolution of bulk Ge. The dissolution process is stopped when Ge nanoparticles are considered to be formed and the Ge nanoparticles may be found H-passivated due to nucleophilic substitution between fluorine and hydrogen atoms [20]. These processes can lead to the formation of hydride termination of Ge nanoparticles. This is consistent with the data shown in the inset graph in Figure 3.1.1.2 with a broad peak at 2042 $cm^{-1}$ (Choi & Buriak, 2000).

---

[18] $GeO_2+6HF \rightarrow H_2GeF_6+2H_2O$ (Kipphardt *et al.*, 1999)

[19] $GeO_2 + H_2O \rightarrow H_2GeO_3$

[20] Nucleophilic attack can be described as an attack of a nucleophile (e.g. $F^-$), which is a chemical species that donates an electron pair to an electrophile (e.g. $H^+$) in order to form a chemical bond (e.g. HF) in case of a reaction (see (Mayr *et al.*, 2001) for more information about nucleophiles and electrophiles).

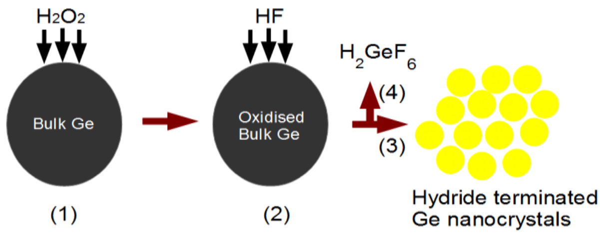

**Figure 3.1.1.3** The dissolution of Ge atoms from bulk Ge which may be considered as a model for the formation of H-terminated Ge nanoparticles.

After investigation of Ge nanoparticles using Raman spectroscopy, the PL spectra were recorded for sample B. As shown in Figure 3.1.1.4, the PL spectrum of sample B (as-prepared, Figure 3.1.1.4 (a)) shows signal in the near infrared region with a single peak centred at about 800 nm, however, after exposing sample B to air for two days in order to see stability of the sample, the PL of sample B was observed to have a broad shoulder (Figure 3.1.1.4 (b)) with a convolution of two peaks centred at 552 nm and 607 nm, in addition to a third peak at 706 nm. The green emission at 552 nm from Ge nanoparticles is generally assigned the oxygen related defect states in oxygen vacancies (Peng *et al.*, 2011).

The 607 nm peak is rather weak, while the nature of emission at 706 nm is unclear, but one may expect that oxidation process should result in reduction of Ge crystalline core, thus increasing the quantum confinement effects. This in turn should result in the blue-shift of the PL emission wavelength.

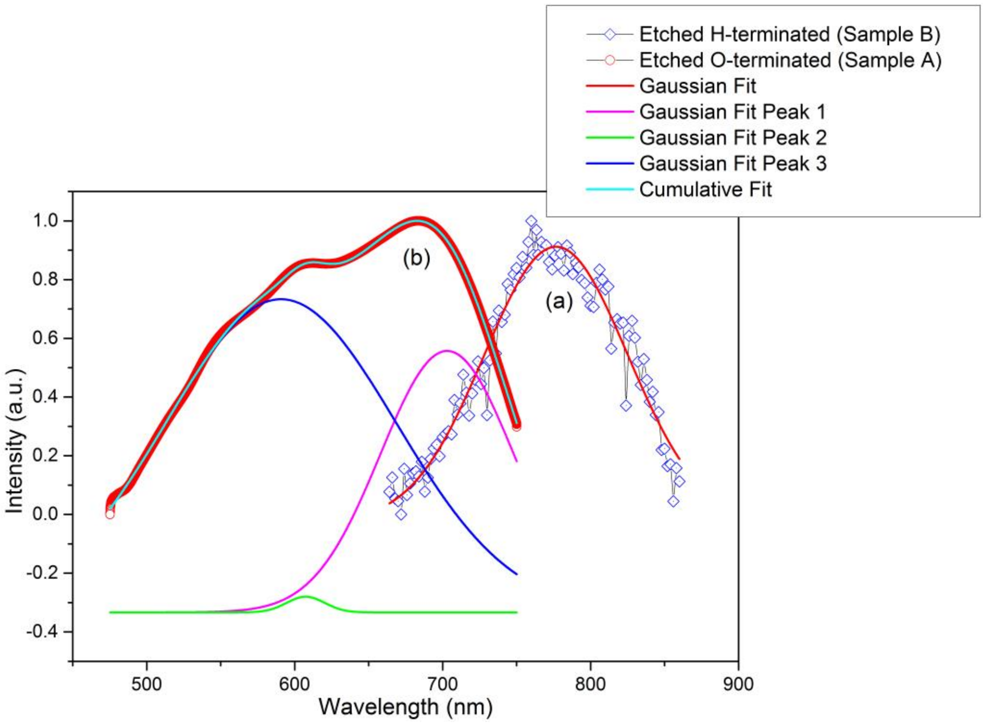

**Figure 3.1.1.4** Photoluminescence of stain etched germanium nanocrystals with an excitation wavelength of 442 nm: (a) H-terminated. The emission peak was found to be at 800 nm (1.55 eV) after a Gaussian single peak fitting. (b) Exposed to air for 2 days (O-terminated). A multi-peak Gaussian fit shows three main peaks at 706 nm (1.76 eV), 607 nm (2.05 eV) and 552 nm (2.25 eV).

Sample B (Ge nanocrystals larger in size) was continued to be characterised using techniques such as TEM and XAFS data (XEOL and OD-EXAFS).

### 3.1.2. TEM Data

Using TEM, the size and the shape of the Ge nanoparticles formed by chemical stain etching were determined. A TEM micrograph is shown in Figure 3.1.2.1 for H-terminated Ge nanocrystals (stored suspended in ethanol) just after preparation using stain etching. The mean size of the crystallite was measured to be 10 nm ± 4 nm out of 60 quantum dots. EDX measurement of germanium nanocrystals as shown in Figure 3.1.2.2 detects germanium and also the trace of oxygen (O) and phosphorus (P). P was only observed in EDX measurement and can be due to the presence of residual $H_3PO_4$ chemical solution. Carbon may be attributed to a carbon coated copper grid.

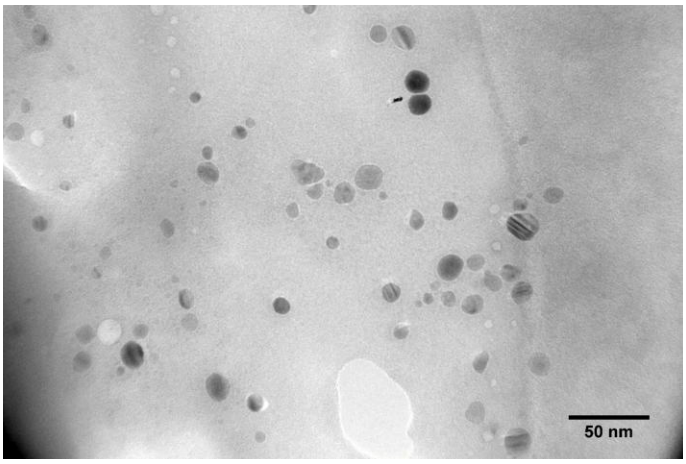

**Figure 3.1.2.1** TEM micrograph of H-terminated Ge nanocrystals formed using stain etching. Size distributions out of 60 quantum dots shows that the average size of Ge nanocrystals is 10 nm ± 4 nm.

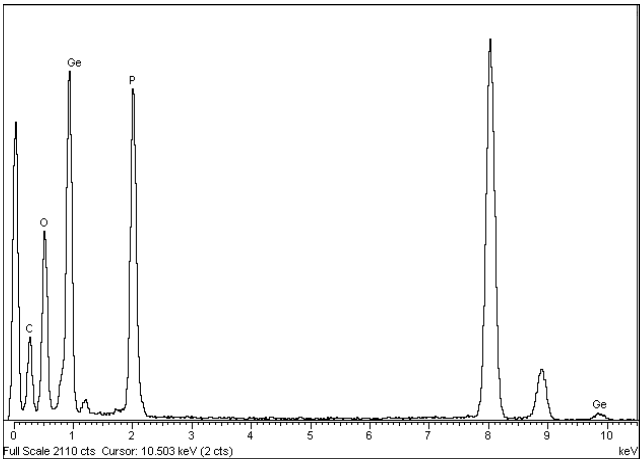

**Figure 3.1.2.2** EDX of stain etched Ge nanocrystals gives the trace of oxides and phosphorus in addition to Ge. The peaks at about 8 keV and 9 keV are from Cu.

SAED of Ge nanocrystals were taken and shown in Figure 3.1.2.3. The SAED of stain etched Ge nanocrystals shows three rings whose measurements are consistent with (002), (113) and (004) planes of diamond cubic structure of Ge.

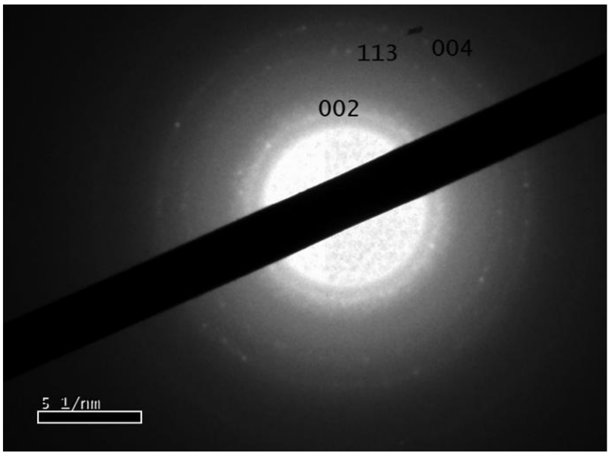

**Figure 3.1.2.3** SAED of stain etched Ge nanoparticles gives a combination of spots, which is an indication of a crystalline feature.

### 3.1.3. XAFS Data

OD-XAS measurements were collected using XEOL at around 700 nm for all samples[21] as that region of emission is not expected to be associated with the germanium oxide. General characteristics of light emission of oxidised Ge were observed to be green in the region from 500 nm to 600 nm (Table 1.1.2.2.). An XEOL spectrum of bulk Ge reference with an emission wavelength of about 550 nm, shown in Figure 3.1.3.1, is consistent with the previous studies of oxidized Ge nanocrystals (Peng *et al.*, 2011).

---

[21] That was because we identified that the emission in 500 nm range was related to the oxide.

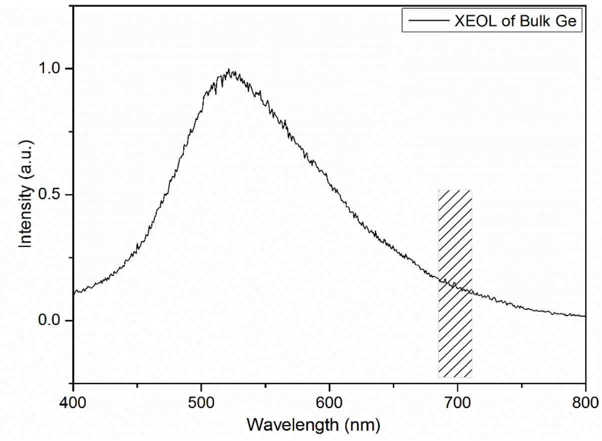

**Figure 3.1.3.1** XEOL of bulk c-Ge produced green emission of photoluminescence. Shaded area shows the XEOL measurement was centred at 700 nm.

EXAFS and OD-EXAFS spectra of bulk Ge at the Ge K-edge were recorded between 11 keV and 12 keV in energy space, as shown in Figure 3.1.3.2(a). This was done in order to determine the amplitude reduction factor, $S_0^2$ of c-Ge and use it as a set parameter for other samples, as a reference measurement, before conducting any EXAFS measurements of nanoparticles. OD-EXAFS differs from EXAFS in terms of probing only the sites which are major contributing sites to the light emission in the whole sample (Dowsett, Adriaens, Jones, Poolton, & Fiddy, 2008; Karatutlu *et al.*, 2013). The difference between EXAFS and OD-EXAFS signals can be clearly seen in Figure 3.1.3.2(a) and is even more obvious in Figure 3.1.3.2(b). The comparison between EXAFS and OD-EXAFS of bulk Ge in *r*-space in Figure 3.1.3.2(b) shows that OD-EXAFS can probe native oxides[22] on the surface of the bulk Ge that are responsible for XEOL emission.

---

[22] Native oxides are the oxides formed naturally after exposing bulk Ge to air.

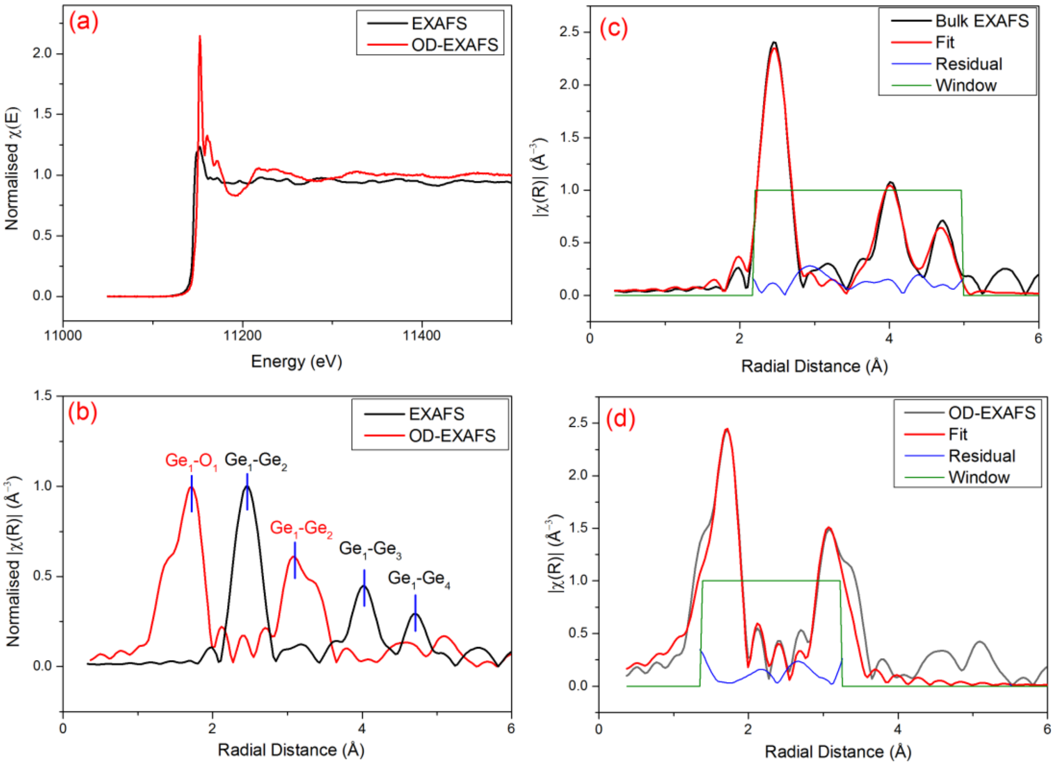

**Figure 3.1.3.2** EXAFS and OD-EXAFS of bulk c-Ge are shown (a) in energy space (b) in *r*-space. The fit of FT modulus of (c) EXAFS of bulk Ge and (d) OD-EXAFS of bulk Ge are represented. The residual between the fit and the data (blue colour) and the window of the fit (olive colour) are also shown.

In Figure 3.1.3.2(c) and (d), the fittings of EXAFS and OD-EXAFS of bulk Ge in *r*-space are represented using structural models of diamond type Ge and alpha-quartz type $GeO_2$. The fit of the FT modulus was obtained from *k*-weighted EXAFS $k^2\chi(k)$ for all fittings. The interatomic distances obtained from the fit of the FT modulus of EXAFS in Figure 3.1.3.2(c) are shown in Table 3.1.3.1. The Debye-Waller factors obtained from the fit are given in Appendix.

**Table 3.1.3.1** The R-factor and interatomic distances extracted from the multiple shell fit of EXAFS of bulk Ge reference sample. The interatomic distances are in Å.

| **The fitting quality and parameters**[23] | **Fit of FT modulus of EXAFS** | **Bulk Ge Model** |
|---|---|---|
| R-factor | 0.016 | - |
| $R_{i1}$ | 2.446 ± 0.003 | 2.449 |
| $R_{i2}$ | 3.989 ± 0.005 | 3.999 |
| $R_{i3}$ | 4.696 ± 0.007 | 4.663 |

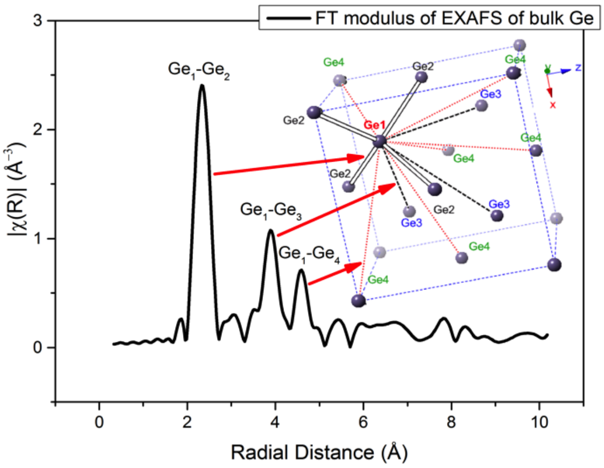

**Figure 3.1.3.3** Reference bulk Ge. The three nearest neighbour distances ($Ge_1$-$Ge_2$, $Ge_1$-$Ge_3$ and $Ge_1$-$Ge_3$) were obtained using FT modulus of EXAFS of bulk Ge and are compared with those of Diamond cubic Ge structure. In the model, Ge1-Ge2 bonds, Ge1-Ge3 bonds and Ge1-Ge4 bonds are shown with white cylinders, black dashed lines and red dotted lines respectively. The values of the interatomic distances measured are shown in Table 3.1.3.1

The first, the second and the third shells are pointed out with the corresponding nearest neighbour distances of the diamond cubic structure, as represented in Figure 3.1.3.3.

---

[23] $R_{i1}$ is the first interatomic distance and was named $Ge_1$-$Ge_2$. $R_{i2}$ was the second and named $Ge_1$-$Ge_3$ and the third, $R_{i3}$ named $Ge_1$-$Ge_4$. See page 129 for the step by step procedure of the fit.

**Table 3.1.3.2** The R-factor and interatomic distances extracted from the multiple shell fit of OD-EXAFS of bulk Ge. The interatomic distances are in Å.

| **The fitting quality and parameters**[24] | **Fit of FT modulus of OD-EXAFS** | **Alpha-quartz type $GeO_2$ Model** | **Amorphous $GeO_2$ (a-$GeO_2$) Model** |
|---|---|---|---|
| R-factor | 0.020 | - | - |
| $R_{i1}$ ($Ge_1$-$O_1$) | 1.719 ± 0.009 | 1.7367 | 1.73± 0.04 |
| $R_{i2}$ ($Ge_1$-$Ge_2$) | 3.145 ± 0.010 | 1.7413 | 3.17± 0.04 |
| $R_{i3}$ | - | 3.1534 | - |

When the results of the fit of the FT modulus of OD-EXAFS are compared with the interatomic distances of alpha-quartz type $GeO_2$ as shown in Table 3.1.3.2, the first and the second shell distances of the fit are very close to the first and the third shell distances of alpha-quartz type $GeO_2$. After comparison, the interatomic distances obtained OD-EXAFS with those of a-$GeO_2$, the first shell and the second shell are also not far from those of a-$GeO_2$ with about 0.01 Å and 0.02 Å difference respectively. The first, the second and the third shells in alpha-quartz type $GeO_2$ are pointed out with the corresponding nearest neighbour distances in Figure 3.1.3.4.

---

[24] $R_{i1}$ is the first interatomic distance and was named $Ge_1$-$Ge_2$. $R_{i2}$ was the second and named $Ge_1$-$Ge_3$ and the third, $R_{i3}$ named $Ge_1$-$Ge_4$. See 121 for the step by step procedure of the fit.

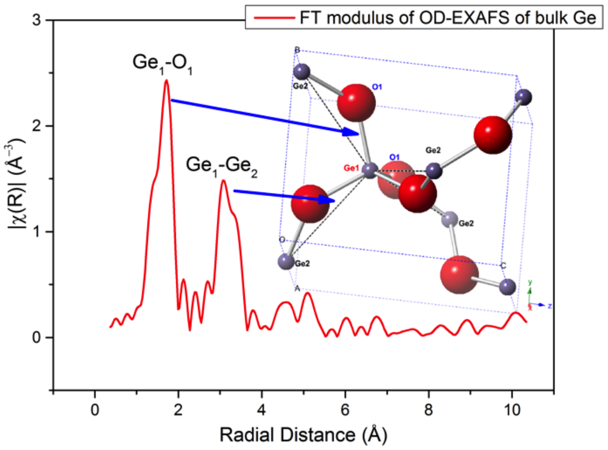

**Figure 3.1.3.4** The two nearest neighbour distances ($Ge_1$-$O_1$ and $Ge_1$-$Ge_2$) were obtained using FT modulus of OD-EXAFS of bulk Ge and are compared with those of alpha-quartz type $GeO_2$ structure. In the model, Ge1-O1 bonds and Ge1-Ge2 bonds are shown with white cylinders and black dashed lines respectively. The values of the interatomic distances measured are shown in Table 3.4.3.2.

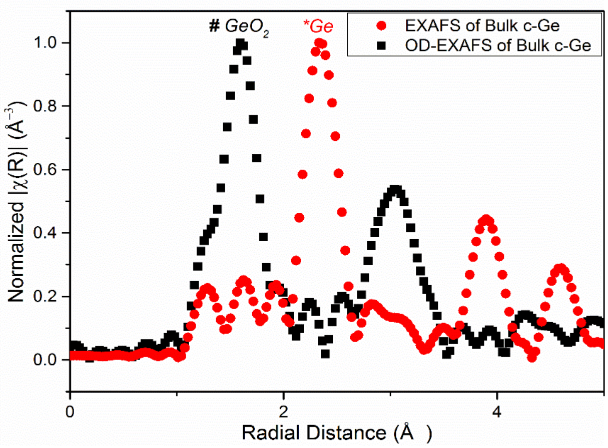

**Figure 3.1.3.5** EXAFS and OD-EXFAS of bulk c-Ge in *r*-space.

Figure 3.1.3.5 shows magnitudes of FT for EXAFS and OD-EXAFS from bulk Ge exposed to air for about 1 year. OD-XAS data were collected using XEOL emission at around 700 nm. Just like in Figure 3.1.3.6 one can clearly see that XEOL emission originates from Ge oxide related structure.

Following the reference measurements, XEOL and OD-EXAFS measurements were conducted for Ge nanocrystals formed by chemical stain etching. The XEOL emission was observed to be in the near-infrared region of electromagnetic spectrum at wavelength of 700 nm (1.77 eV) as shown in Figure 3.1.3.7.

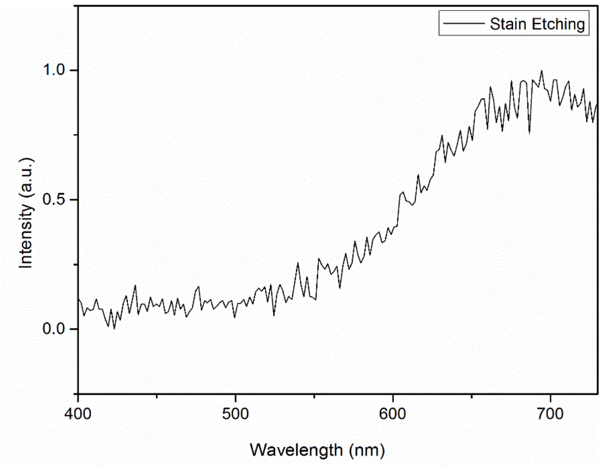

**Figure 3.1.3.7** XEOL of stain etched Ge nanocrystals emits near infrared emission of photoluminescence after exciting with X-rays at 100 K. The measurement was collected until a wavelength of 730 nm due to the limitation of experimental set-up.

In Figure 3.1.3.8, the magnitude of FT of OD-EXAFS of stain etched Ge nanocrystals shows a single peak at a distance of 2.44 ± 0.01 Å (see Table. 3.1.3.3), which is shorter by 0.06 Å than that of bulk Ge reference (Table 3.1.3.1). Thus, OD-EXAFS results clearly suggest that XEOL signal in stain etched Ge nanoparticles can be linked to Ge (rather than oxide-related) structure. Unfortunately we have been unable to record transmission EXAFS signal for the stain etched sample due to technical problems with the experimental station.

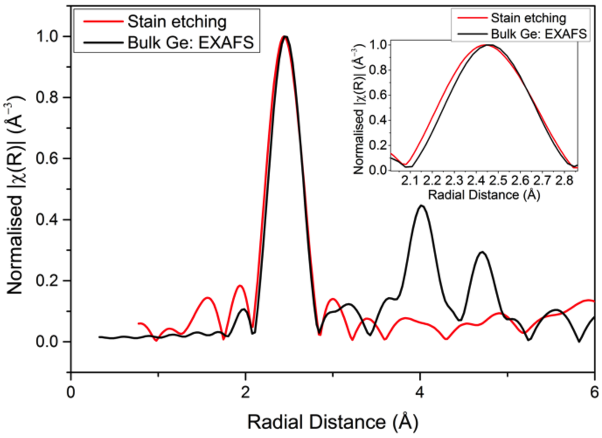

**Figure 3.1.3.8** The normalised FT modulus of OD-EXAFS of stain etched Ge nanocrystals is shown in red and compared with the FT of EXAFS of bulk c-Ge. Disordered Ge atoms centered at 2.44 ± 0.01 Å. The inset shows 0.006 Å difference between the FT modulus of EXAFS of the bulk Ge and The FT modulus of OD-EXAFS of stain etched Ge nanocrystals.

**Table 3.1.3.3** The R-factor and interatomic distances extracted from the first shell fit of OD-EXAFS of Ge nanoparticles formed using stain etching. The interatomic distances are in Å.

| **The fitting quality and parameters** | **OD-EXAFS of stain etching** |
|---|---|
| R-factor | 1.000 |
| $R_{i1}$ | 2.44 ± 0.01 |

## Summary of the Results

The overall results for the stain etched sample can be summarised as follows:

- Size of Ge nanoparticles was found to be 10 ± 4 nm and 6.9 ± 0.3 nm by TEM and Raman spectroscopy respectively.
- PL spectroscopy shows an emission peak approximately at 750 nm (1.65 eV).
- XEOL shows an emission at 700 nm (1.77 nm).
- OD-EXAFS shows the XEOL emission is due to the disordered Ge structure.

It can be inferred from the OD-EXAFS and XEOL results shown in Figure 3.1.3.8 and Figure 3.1.3.7 respectively that OD-EXAFS can be site-selective. The results also suggest that disordered Ge sites within Ge nanoparticles contribute to the emission at about 700 nm (1.77 eV). Despite the differences between XEOL and PL such that XEOL can excite sites not accessible with PL, both of the measurements were collected in a similar region of visible spectrum (Taylor, Finch, Mosselmans, & Quinn, 2013). The difference between PL and XEOL measurements of Ge nanoparticles formed using chemical stain etching can also be attributed to the temperature difference of the measurements (XEOL at 100 K and PL at RT).

## 3.2. Liquid Phase Pulsed-Laser Ablation (LP-PLA)

### 3.2.1. Raman and PL Spectroscopy

The appearance of these particles after production was creamy-white (see Figure 2.2.2.2), whereas both of the samples (sample A and B given in Section 5.1, see page 40) by stain etching were pure yellow in colour to the human eye. The Raman spectrum of Ge nanoparticles formed at the end of 7 hours by LP-PLA in liquid n-hexane is shown in Figure 3.2.1.1 where one can see an asymmetric peak located at 292 cm$^{-1}$. The size of the nanocrystallites was calculated using the phonon confinement model (Campbell & Fauchet, 1986; Richter *et al.*, 1981) and found to be approximately 6 nm. The origins of the discrepancy between the fitting and the experimental data are unclear, but may be due to amorphous Ge (broad peak at around 275 cm$^{-1}$, see Coppari *et al.*, 2009) present in the sample.

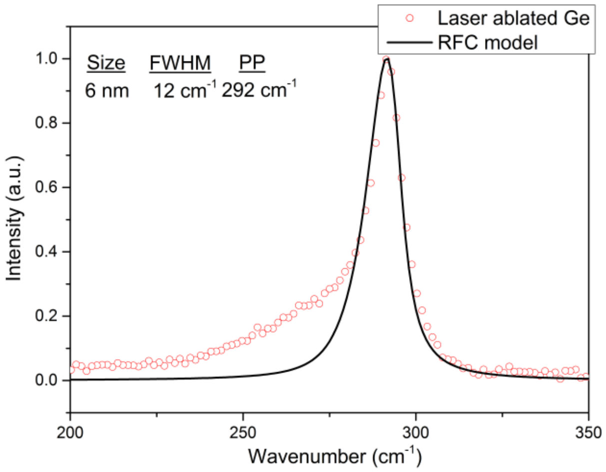

**Figure 3.2.1.1** Raman spectrum of the nc-Ge formed by LP-PLA in n-hexane at the end of 7 hours together with the fitting using the RFC model.

The PL spectroscopy measurement shows a broad emission spectrum, which can be fitted with four peaks at 545 nm (2.27 eV), 605 nm (2.05 eV), 656 nm (1.89 eV) and 700 nm (1.77 eV) (see Figure 3.2.1.2).

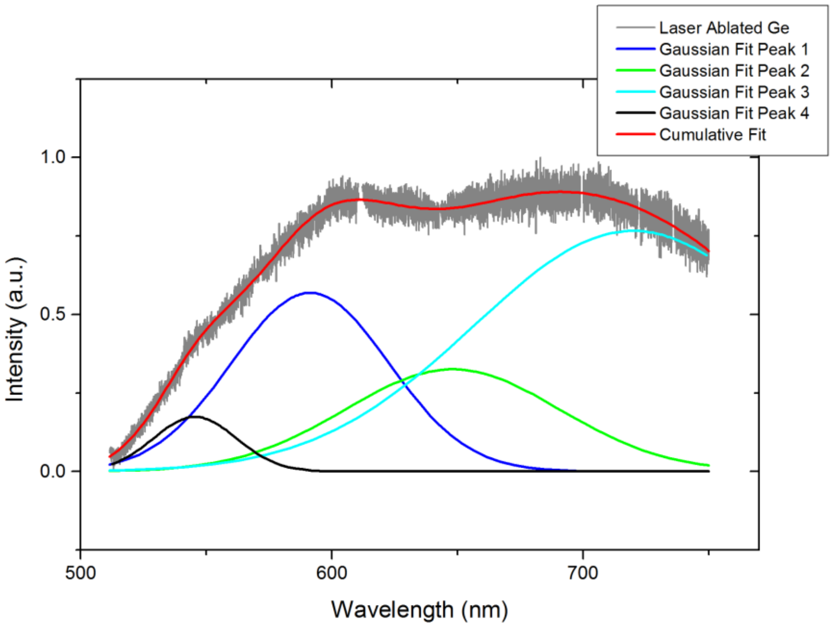

**Figure 3.2.1.2** Photoluminescence of Ge nanocrystals formed by LP-PLA in n-hexane at the end of 7 hours. A multi-peak Gaussian fit shows four main peaks at 545 nm (2.27 eV), 605 nm (2.05 eV), 656 nm (1.89 eV) and 700 nm (1.77 eV).

At this stage it’s difficult to associate the peaks with a specific emission mechanism, but by analogy with previous section the peak at around 700 nm can perhaps be tentatively linked to quantum confinement effects in Ge nanoparticles while the peak at around 545 nm could be due to $GeO_2$.

### 3.2.2. TEM Data

A TEM micrograph of Ge nanoparticles (stored suspended in ethanol) formed using LP-PLA is shown in Figure 3.2.2.1. Using TEM, the mean size of the Ge nanoparticles out of 60 nanoparticles is measured to be 41 nm ± 22 nm. The size deviates much more than expected when compared to the mean size found using the phonon confinement model (approximately 6 nm). This is due to the fact that the nanoparticles formed using LP-PLA can have a tendency to agglomerate after the ablation process. Thus the dark spots observed in in Figure 3.2.2.1 correspond to a number of nanoparticles stuck together. It has been reported that if nanoparticles formed using LP-PLA are not stable inside the suspension solution, then agglomeration can start, and even oxidation might occur depending on the composition of nanoparticles (Amendola & Meneghetti, 2013). Thus we do observe agglomeration in our nanoparticles formed using LP-PLA, but oxidation of nanoparticles at the moment of formation does not seem likely since ablation was performed inside liquid n-hexane. The latter would suggest that oxide-related emission at 545 nm (Figure 3.2.1.2) is most likely associated with oxide formation after synthesis (i.e. due to exposure to air when handling samples).

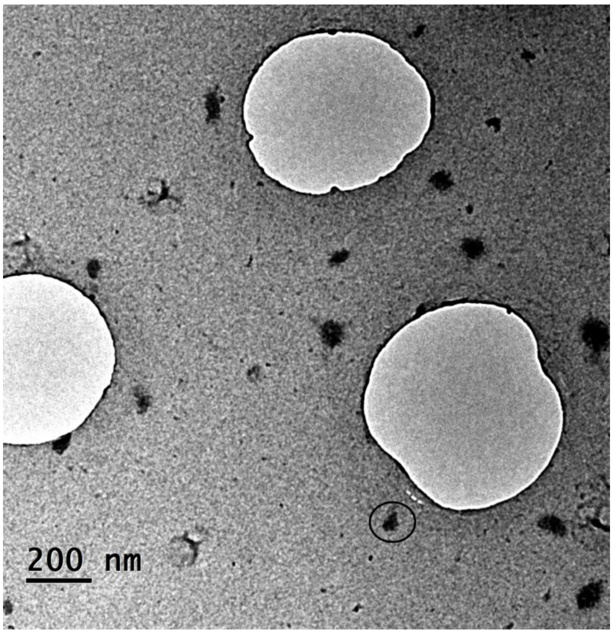

**Figure 3.2.2.1** TEM micrograph of Ge nanocrystals formed by LP-PLA in n-hexane at the end of 7 hours.

Elemental analysis from the area of the circle shown in the micrograph, given in Figure 3.2.2.1, using EDX spectroscopy measurement indicates mostly Ge with a small amount of O in Figure 3.2.2.2. The other elements such as C and Cu can be attributed to the C coated Cu TEM grid.

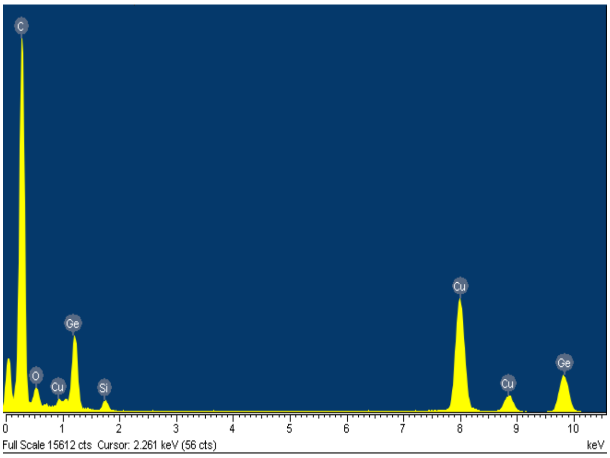

**Figure 3.2.2.2** EDX of Ge nanocrystals formed by LP-PLA in n-hexane at the end of 7 hours.

Another example of TEM measurements of Ge nanoparticles formed using LP-PLA is represented in Figure 3.2.2.3. The micrograph clearly shows the agglomeration of Ge nanoparticles.

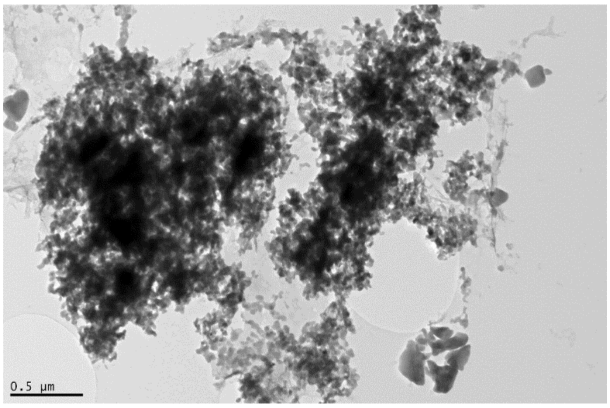

**Figure 3.2.2.3** TEM micrograph of an example of agglomeration issue in the formation of Ge nanocrystals.

SAED of Ge nanoparticles formed by LP-PLA was taken and is shown in Figure 3.2.2.4. The spots in Figure 3.2.2.4 are represented by an oval and rectangular annotations (green, red and blue) for the planes of (133), (044), (133) and (333) respectively of diamond type Ge. The SAED measurement in Figure 3.2.2.4 is thus consistent with the Raman spectroscopy measurement.

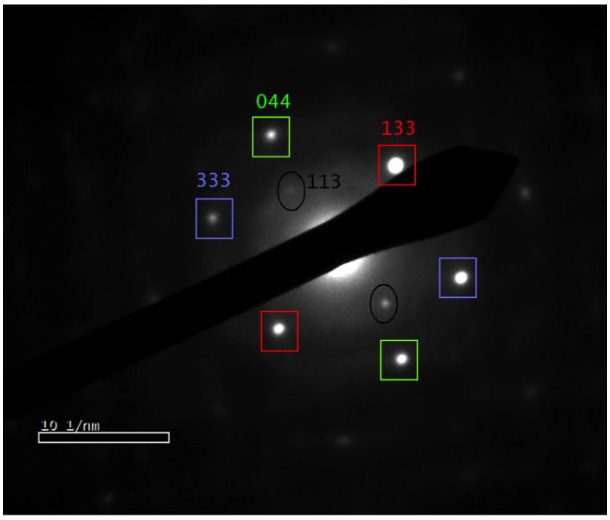

**Figure 3.2.2.4** SAED of Ge nanoparticles formed using LP-PLA gives several spots, which is an indication of the crystalline features of Ge nanoparticles.

### 3.2.3. XAFS Data

The results of transmission and OD-EXAFS are shown and compared in Figure 3.2.3.1. The data are shown in energy space and in *r*-space in Figure 3.2.3.1(a) and

Figure 3.2.3.1(b). There is a clear difference between EXAFS and OD-EXAFS of the Ge nanoparticles formed using LP-PLA, which is particularly obvious in *r*-space in Figure 3.2.3.1(b). The OD-EXAFS data seem to suggest that mostly $GeO_2$ is responsible for the light emission. However, the best fit to the OD-EXAFS data is obtained when a mixed cluster model is used that also includes diamond type Ge structure (see Table 3.2.3.1). This may suggest some small contribution from Ge nanoparticles to the light emission in addition to $GeO_2$ with the structural parameters close to the alpha-quartz phase (Table 1.1.2.1). The best fit to the transmission data is obtained using diamond type Ge structure (Table 3.2.3.1).

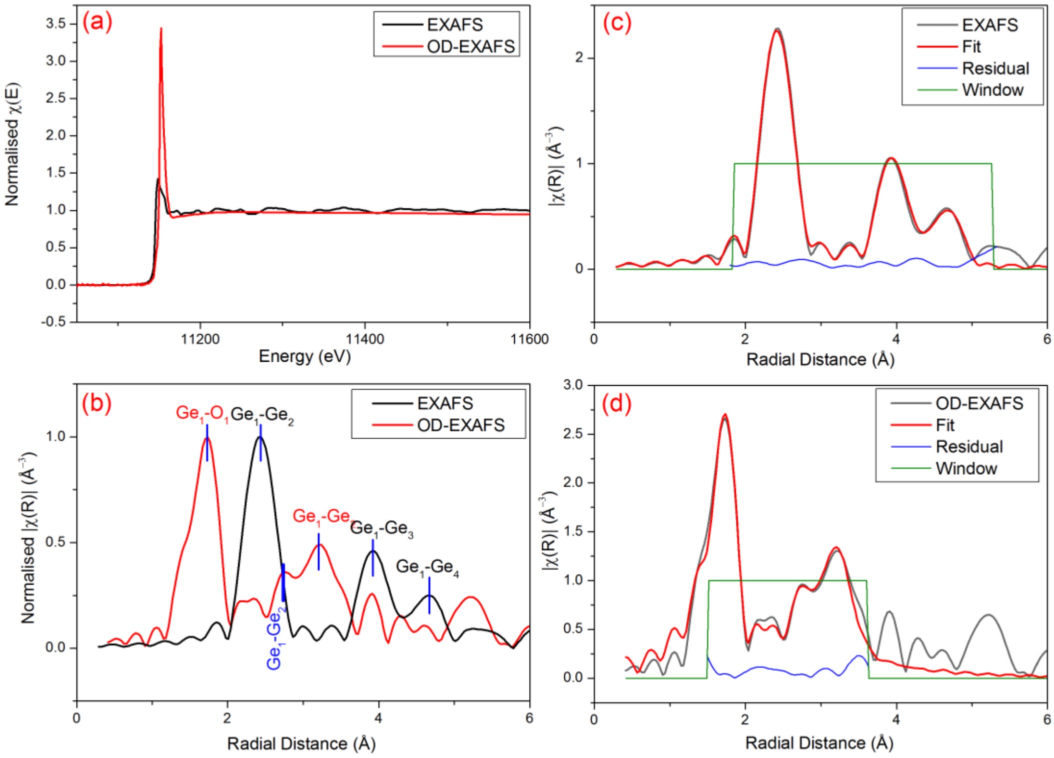

**Figure 3.2.3.1** EXAFS and OD-EXAFS of nc-Ge formed by LP-PLA are shown (a) in energy space (b) in *r*-space. The fit of the FT modulus of (c) EXAFS of nc-Ge formed by LP-PLA and (d) OD-EXAFS of nc-Ge formed by LP-PLA are represented. The residual between the fit and the data (blue colour) and the window of the fit (olive colour) are also shown.

**Table 3.2.3.1** The R-factor and interatomic distances extracted from the multiple shell fit of EXAFS and OD-EXAFS of nc-Ge. The interatomic distances are in Å.

| **The fitting quality and parameters** | **LP-PLA EXAFS** | **LP-PLA OD-EXAFS** |
|---|---|---|
| R-factor | 0.018 | 0.007 |
| $R_{i1}$ | 2.438 ± 0.005 | 1.733 ± 0.004 |
| $R_{i2}$ | 3.981 ± 0.008 | 2.510 ± 0.016 |
| $R_{i3}$ | 4.668 ± 0.009 | 3.143 ± 0.008 |

## Summary of the Results

The results for the LP-PLA sample can be summarised as follows:

- Size of Ge nanoparticles was found to be 41 ± 22 nm and 6.2 ± 0.3 nm by TEM and Raman spectroscopy respectively. TEM data suggest that the origin of the discrepancy is particle agglomeration.
- PL spectroscopy shows emission peaks approximately at 545 nm (2.27 eV), 605 nm (2.05 eV), 656 nm (1.89 eV) and 700 nm (1.77 eV).
- OD-EXAFS shows the emission is mainly due to the alpha-quartz type $GeO_2$.

The fit represented in Figure 3.2.3.1(c) for EXAFS shows a good consistency for a diamond type Ge structural model. In the case of the OD-EXAFS fit in Figure 3.2.3.1(d), the diamond cubic structure of Ge was used in addition to the alpha-quartz type $GeO_2$ (see Table 3.2.3.1), but the major contribution to the light emission from Ge nanoparticles formed using LP-PLA is due to $GeO_2$ sites.

## 3.3. Sol-Gel Method

### 3.3.1. Raman and PL Spectroscopy

The data in Figure 3.3.1.1 represent Raman signal of $GeO_2$-$SiO_2$ co-polymer (sample colour is white, see page 46) which was obtained via annealing for 48 hours heating treatment at 100 °C and an additional 3 hours heating treatment at 600 °C in air. The peak at 433 $cm^{-1}$ in Figure 3.3.1.1 was assigned to Ge-O-Ge symmetric stretching mode (Micoulaut *et al.*, 2006) due to the co-polymerisation of $GeO_2$-$SiO_2$.

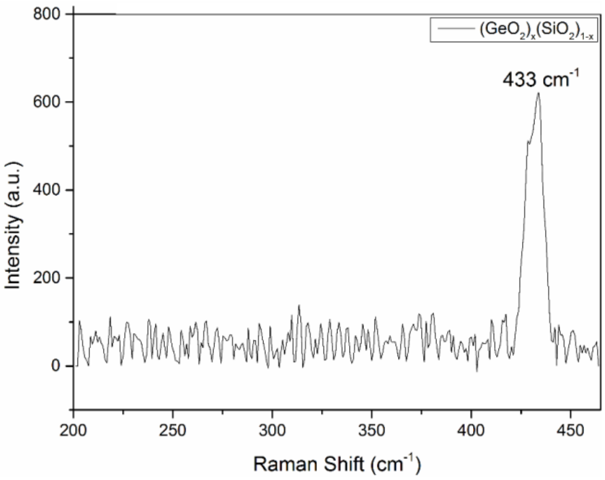

**Figure 3.3.1.1** Raman shift of $GeO_2$-$SiO_2$ co-polymer after annealing at 600 °C in air.

An additional heating treatment at 700 °C in $H_2$(5%)/Ar(95 %) was followed in order to reduce $GeO_2$ to Ge in the co-polymer so as to obtain nanocrystalline Ge embedded in a $SiO_2$ matrix (brown in colour, see Page 46). Figure 3.3.1.2 shows Raman signal of the Ge nanocrystals at the end of the thermal process at 700 °C in $H_2$(5 %)/Ar(95 %). The size calculated using the phonon confinement model (Campbell & Fauchet, 1986; Richter *et al.*, 1981) was estimated to be approximately 5 nm. Again, the nature of discrepancy between the RFC model and the experimental signal may be due to amorphous contribution (see Section 3.2.1 above).

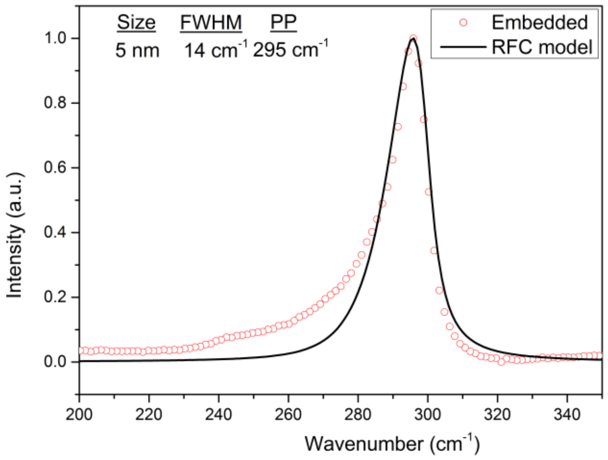

**Figure 3.3.1.2** Raman Shift of nc-Ge after $H_2$(5 %)/Ar(95 %) heating treatment at 700 °C together with the fitting using the RFC model.

The PL measurement from Ge nanocrystals embedded in silica given in Figure 3.3.1.3 has two emission peaks at 595 nm (2.08 eV) and 670 nm (1.85 eV). Optical properties of Ge nanocrystals of similar sizes (3-5 nm) embedded in amorphous silica were reported with broad PL emission peaks at 2.18-2.2 eV (563-570 nm) with the absorption edge at 2.8 eV (442nm) (Maeda *et al.*, 1991; Nogami & Abe, 1997) at assigned to the quantum confinement effects (QCE) in Ge.

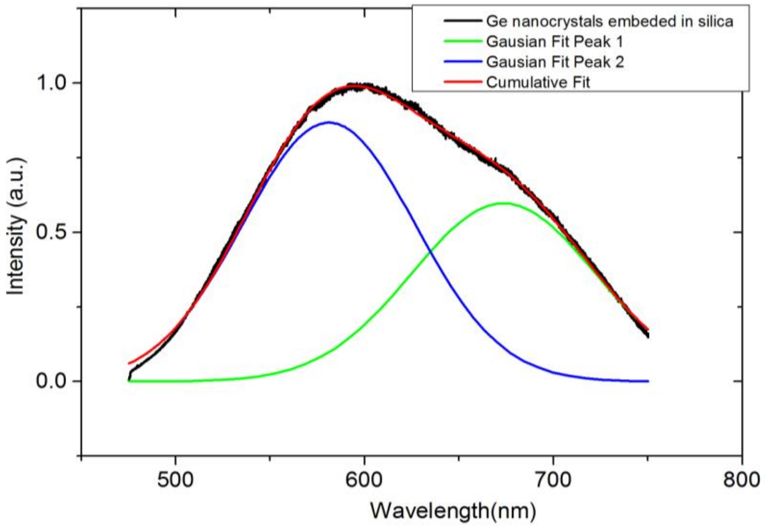

**Figure 3.3.1.3** Photoluminescence of nc-Ge after $H_2$(5 %)/Ar(95 %) heating treatment at 700 °C. A multi-peak Gaussian fit shows two main peaks at 595 nm (2.08 eV) and 670 nm (1.85 eV).

Thus, we can tentatively associate the 595 nm emission with the QCE. The emission at 670 nm can perhaps be ascribed to the surface-interface states formed on the boundary between Ge nanoparticles and silica matrix as described in the Introduction (see Figure 1.2.1.7). However, the neither the results reported previous nor our PL data fit the QCE models for Ge nanoparticles of 3-5 nm in size where the light emission is expected below approximately 1.5 eV (826 nm) (see Figure 1.2.1.5).

## 3.3.2. TEM Data

The TEM micrograph in Figure 3.3.2.1 shows Ge nanocrystals (spherical particles, black in colour) embedded in a silica matrix (grey surrounding environment). The size of Ge nanocrystals was estimated to be 10 nm ± 6 nm measured out of 60 nanoparticles.

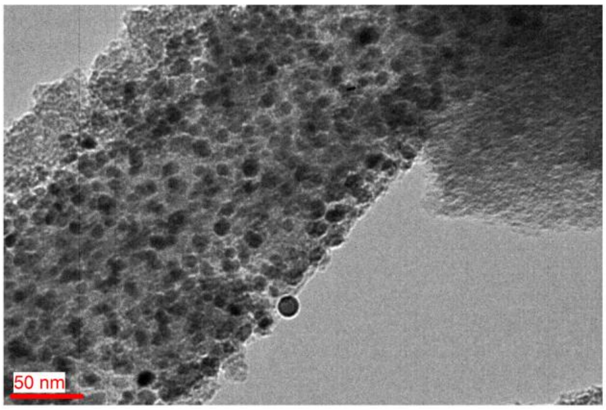

**Figure 3.3.2.1** TEM micrograph of Ge nanocrystals embedded in silica produced using the sol-gel method. Size distributions out of 60 quantum dots shows that the average size of Ge nanocrystals is 10 nm ± 6 nm.

EDX shows in Figure 3.3.2.2(a) Ge, O and Si. Quantitative results of the elemental analysis of Ge, O and Si are also represented in Figure 3.3.2.2(b) for the typical area given in Figure 3.3.2.3 with a weight percentage of 5.47 ± 0.04, 46.83 ± 0.08 and 47.70 ± 0.04 respectively.

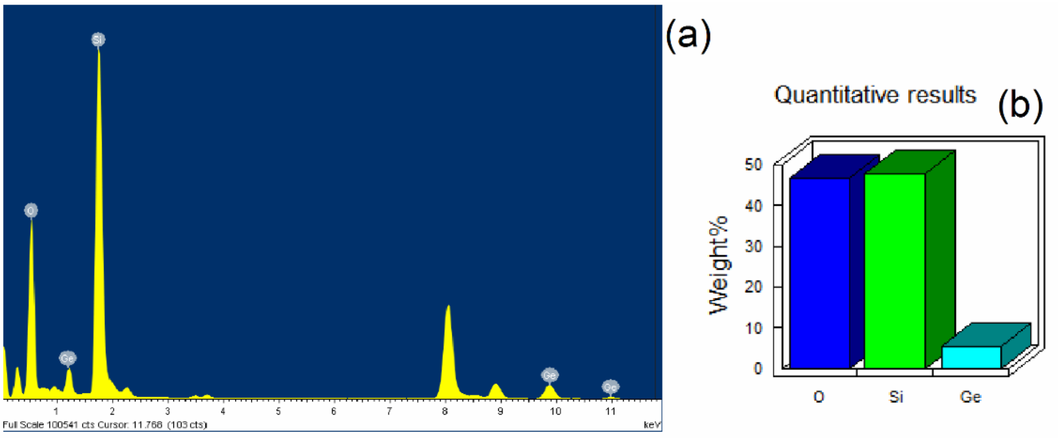

**Figure 3.3.2.2** EDX of nc-Ge after $H_2$(5 %)/Ar(95 %) heating treatment at 700 °C.

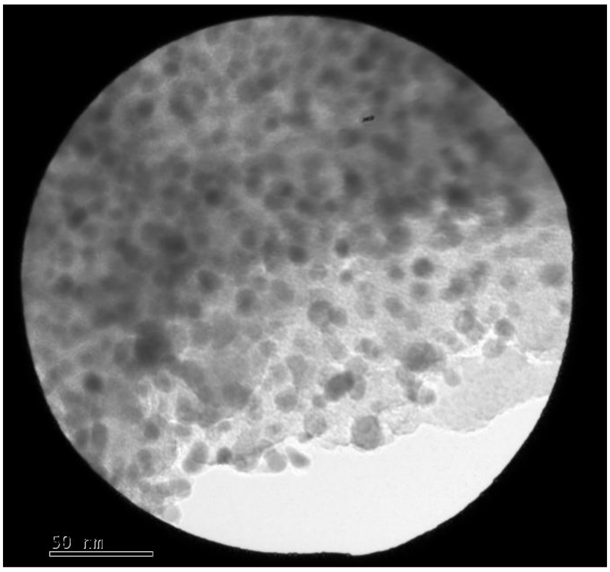

**Figure 3.3.2.3** The area of SAED which also shows a typical area for the EDX measurement.

In addition to the elemental analysis which can show signs of Ge nanocrystals within an oxide enriched environment, SAED might also be indicative for other phases such as the existence of $GeO_2$ (Peng *et al.*, 2011). The reflections from the first ring given in Figure 3.3.2.4(a) are attributed to alpha-quartz type $GeO_2$ $(\bar{1}22)$. Some of the spots are ascribed to the reflections of diamond type Ge (044) and Ge (333) as the corresponding circles are drawn in Figure 3.3.2.4(b).

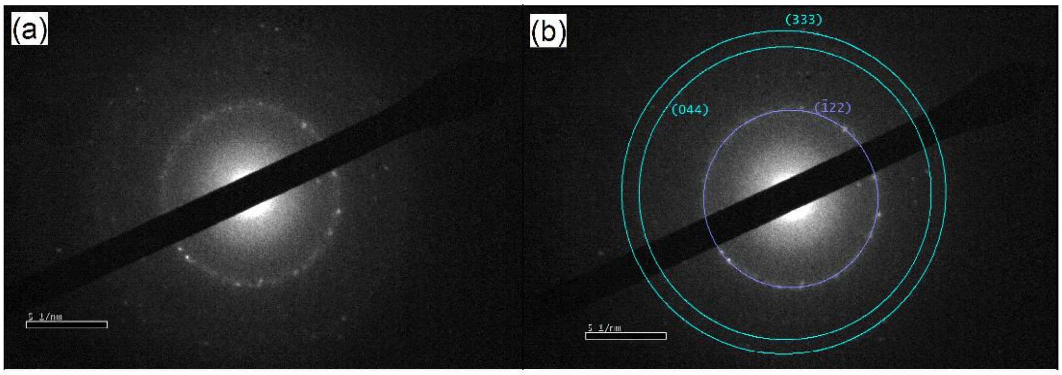

**Figure 3.3.2.4** SAED of Ge nanoparticles embedded in an oxide enriched silica matrix formed using the sol-gel method gives a combination of spots, which is an indication of a crystalline feature of Ge and also oxides.

## 3.3.3. XAFS Data

As explained in previous sections (Section 3.1 and 3.2, see pages 63 and 75 respectively), in order to complete the link between the structural contribution and the optical emission, the sample formed using the sol-gel method is characterised with EXAFS, OD-EXAFS using XEOL. XEOL measurement of Ge nanocrystals embedded in silica gives a broad peak around 500 nm. The onset of the peak at 400 nm (3.1 eV) observed in the XEOL measurement given in Figure 3.3.3.1 is referred to oxide sites in silica glasses (Yoshida, Tanabe, Takahara, & Yoshida, 2005).

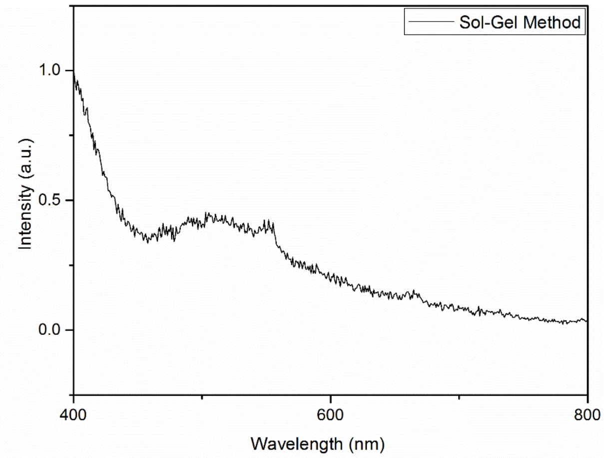

**Figure 3.3.3.1** XEOL of nc-Ge embedded in silica shows a broad spectrum of photoluminescence.

The XEOL data are clearly very different from the PL data above (figure 3.3.1.3). The reason for it is unclear, but in part may be due to very strong XEOL signal from $SiO_2$ matrix and low temperature (100 K) at which XEOL measurements were taken. EXAFS and OD-EXAFS (recorded at around 550 nm) data in energy space and in *r*-space of Ge nanocrystals embedded in silica are given in Figure 3.3.3.2. The transmission data suggest a large amount of $GeO_2$ and a relatively small amount of Ge (e.g. compare the relative amplitudes of Ge-O and Ge-Ge shells in Figure 3.3.3.2 (c), no phase correction).

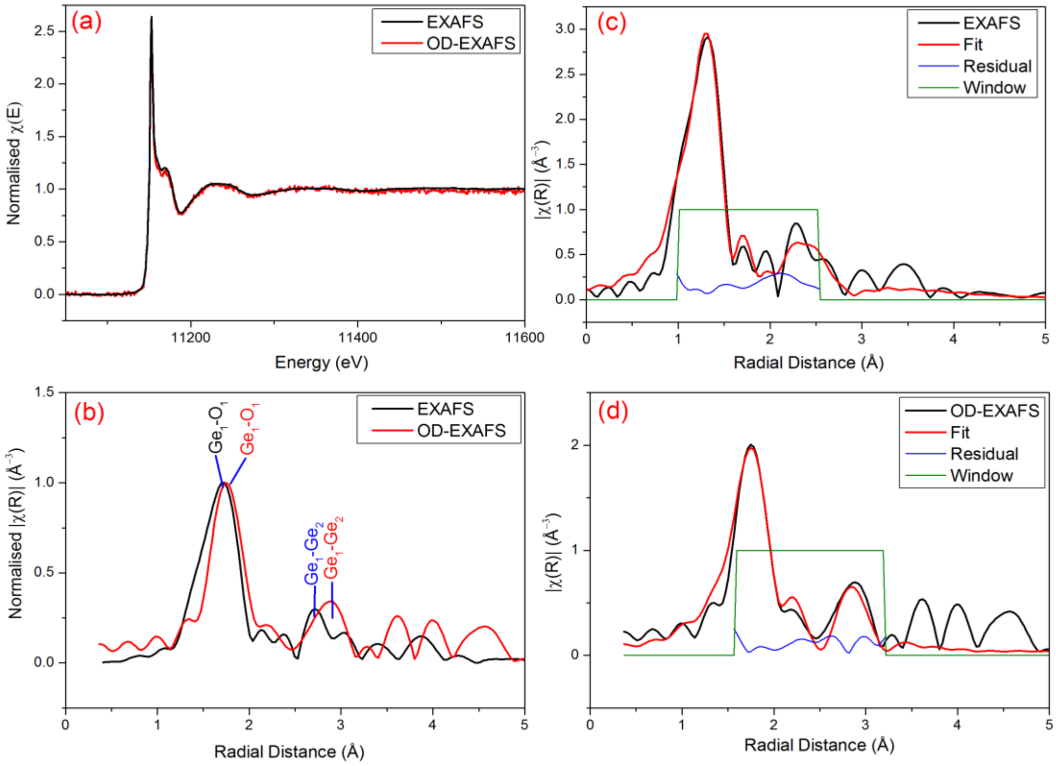

**Figure 3.3.3.2** EXAFS and OD-EXAFS of Ge nanocrystals formed using the sol-gel method are shown (a) in energy space (b) in *r*-space. The fit of the FT modulus of (c) EXAFS of Ge nanocrystals formed using the sol-gel method and (d) OD-EXAFS of Ge nanocrystals formed using the sol-gel method are represented. The residual between the fit and the data (blue colour) and the window of the fit (olive colour) are also shown.

EXAFS and OD-EXAFS of Ge nanocrystals embedded in $SiO_2$ look similar until after 3 Å, but careful investigation shows they are slightly different in that Ge-Ge distance (at above 2 Å) in OD-EXAFS signal is slightly longer (see Figure

3.3.3.2 (b)). After fitting the FT modulus of EXAFS and OD-EXAFS using the mixed rutile type $GeO_2$ and the diamond cubic structure of Ge cluster model, the first and the second distances were obtained and are shown in Table 3.3.3.1. The fit of the FT modulus of OD-EXAFS was performed using the rutile type $GeO_2$ once it was clear that Ge-O-Ge distance was under 3 Å.

From the table we can see that Ge-O distances ($R_{i1}$) are close within error, while second shell distances ($R_{i2}$) are clearly different. In fact, the second shell distance extracted from EXAFS data is close to one found in diamond type Ge, while second shell distance extracted from OD-EXAFS closer to Ge-O-Ge bond in rutile type Ge. This suggests that XEOL light emission in sol-gel samples originates from $GeO_2$.

**Table 3.3.3.1** The R-factor and interatomic distances extracted from the multiple shell fit of EXAFS and OD-EXAFS of Ge nanoparticles embedded in silica formed using the sol-gel method. The interatomic distances are in Å.

| **The fitting quality and parameters** | **The sol-gel method EXAFS** | **The sol-gel method OD-EXAFS** |
|---|---|---|
| R-factor | 0.035 | 0.019 |
| $R_{i1}$ ($Ge_1$-$O_1$) | 1.729 ± 0.010 | 1.748 ± 0.014 |
| $R_{i2}$ ($Ge_1$-$Ge_1$) | 2.478 ± 0.035 | 2.889 ± 0.028 |

## Summary of the Results

The results for the sol-gel sample can be summarised as follows:

- Size of Ge nanoparticles was found to be 10 ± 6 nm and 5.3 ± 0.3 nm by TEM and Raman spectroscopy respectively.
- PL spectroscopy shows emission peaks approximately at 600 nm (2.06 eV) and 675 nm (1.84 eV).

- XEOL shows emission peaks approximately at 400 nm (3.1 eV), 550 nm (2.48 eV).
- OD-EXAFS shows the emission is due to the rutile-like $GeO_2$.

Due to the fact that annealing at 700 $^{o}$C can result in highly crystalline samples (Maeda *et al.*, 1991), the source of the red emission in PL to some extent was believed to arise from the quantum confinement effect (lowest electron-hole pair using the Brus model (Brus, 1984)). Nevertheless, as can be seen in Figure 3.3.3.2 (OD-EXAFS data), oxide-enriched environments with the rutile-like $GeO_2$ are the main contributing sites to the light emission.

## 3.4. Colloidal Synthesis

### 3.4.1. Colloidal Chemistry and Colloidally Stable Synthesis of Ge Nanoparticles

In this section, seeking to improve sample yield, reduce structural (and electronic) effects of an enclosing matrix and have more control over the surface termination, we used room temperature colloidal methods to synthesise Ge nanoparticles. Ge nanoparticles (used as Ge quantum dots or qdots) formed via the reduction of $GeCl_4$ (named $CS_1$ when Ar flow is used during the synthesis and $CS_1$-$H_2$ when $H_2$/Ar flow is used) (Chou *et al.*, 2009) and $GeO_2$ (named $Ca_1$) (Wu *et al.*, 2011) and further processed by annealing. All samples were investigated using the same techniques as in the previous sections with addition of X-ray diffraction and UV-Vis spectroscopy. The reason XRD was introduced is due to the fact that the Raman and TEM measurements showed surprising result, such as slightly or significantly different sample sizes. This may have originated from limitations of

TEM/SAED (e.g. sample annealing, clustering etc.) and of Raman (i.e. the surface and the interface contributions to the signal) techniques. OD-EXAFS data (see Figure 3.1.3.7) for stain etched sample seem to suggest significant disorder (i.e. no second shell was observed in FT). Hence, we have used EXAFS and XRD, which are complementary to each other, in that they provide short-range and long-range information respectively.

We did attempt to conduct OD-EXAFS measurements for colloidal samples, but due to technical problems at the beamline we have been unable to obtain XEOL signals of sufficient quality to extract OD-EXAFS. Thus, in the following sections we concentrate on building a detailed structural model of colloidal Ge nanoparticles that is consistent with the optical measurements.

## 3.4.2. The Benchtop Colloidal Synthesis Method 1 ($CS_1$): Formation of Ge Quantum Dots by Reduction from $GeCl_4$

### 3.4.2.1. Raman, PL and UV-Vis Absorption Spectroscopy

As noted in the previous sections, Raman spectroscopy was used as a first analysis technique to understand the structural properties of the Ge qdots as well as for the estimation of the average size of $CS_1$. Raman data together with analysis using RFC model are shown in Figure 3.4.2.1(a). A broad asymmetric peak just below 300 $cm^{-1}$ can be seen as expected for the diamond-type Ge qdots. The Raman spectrum of free-standing $CS_1$ (see Figure 3.4.2.1(a)) has an asymmetrical Lorentzian shape, which is an indication that the sample may be nanocrystalline (Fujii *et al.*, 1991; Karavanskii *et al.*, 2003), as is the shift in the peak position relative to the bulk Ge value.

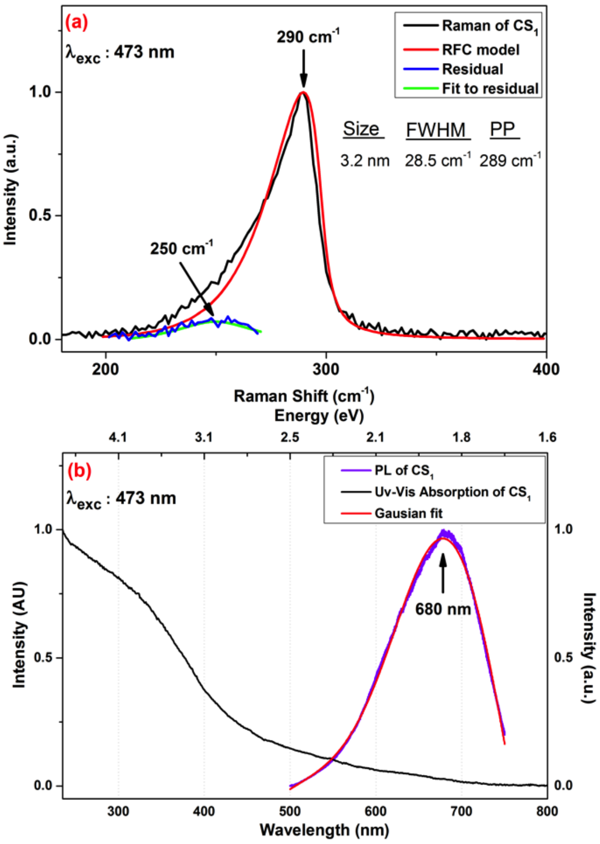

**Figure 3.4.2.1** (a) Raman spectrum of Ge qdots ($CS_1$). The Raman data were fitted with the RFC model (red colour) and subtracted from the data. Residual (blue colour) shows a peak at 250 $cm^{-1}$ after fitting with a Voigt fit (green colour). (b) Photoluminescence and UV-Vis absorption spectrum of Ge qdots ($CS_1$). A Gaussian fit shows the PL peak position at 680 nm. A diode laser was conducted at 473 nm excitation wavelength for both of these particular Raman and PL spectroscopy measurements.

The phonon confinement model (Campbell & Fauchet, 1986; Richter *et al.*, 1981) based on phonon shape modification was used to estimate the mean size of $CS_1$ which was found to be about 3.2 nm for the Raman spectrum given in Figure 3.4.2.1(a). The model deviates from the shape of the Raman signal particularly at frequencies below 273 $cm^{-1}$. Thus, the Raman data were subtracted from the RFC fit and a residual was obtained, and is shown in Figure 3.4.2.1. A Voigt fit to the residual gives a small peak at 250 $cm^{-1}$.

UV-Vis Spectrometry and PL spectroscopy measurements were used to examine the optical properties of Ge qdots ($CS_1$). In Figure 3.4.2.1(b), the PL emission peak of $CS_1$ was found to be at 680 nm when an excitation wavelength of 473 nm by a diode laser was used. The UV-Vis absorption spectrum of $CS_1$ suspended in ultra-distilled water is also shown in Figure 3.4.2.1(b). The broad UV-Vis absorption spectrum of $CS_1$ data shows that the absorption is shifted to around 400-450 nm (3.1-2.75 eV), clearly indicating a significant change as compared to bulk Ge (0.67 eV) (Mirabella *et al.*, 2013). From UV-Vis and absorption measurements it is also clear that the nature of absorption and emission event are different as the PL emission peaks at 680 nm (1.82 eV) while absorption onset takes place at around 450 nm (2.75 eV). The value of the absorption edge fall between tight binding model and k.p perturbation theory for 3 nm particles (see Figure 1.2.1.5), but is not consistent with the experimental data by Bostedt (Bostedt, 2002). However, one has to remember that Bostedt data are reported for Ge nanoparticles grown on a Si substrate and surface contribution due to substrate cannot be excluded. It is well-known that due to the high probability of excitons being captured by surface states, followed by a subsequent recombination, the surface contribution to the emission spectra (Alivisatos, 1996a; Delerue *et al.*, 1998; Okamoto & Kanemitsu, 1996; Warner & Tilley, 2006) may be significant.

In order to shed some light onto the origin of the residual peak at 250 cm$^{-1}$ in Figure 3.4.2.1 (a) we looked at the possible contribution from Ge phases other than diamond type.

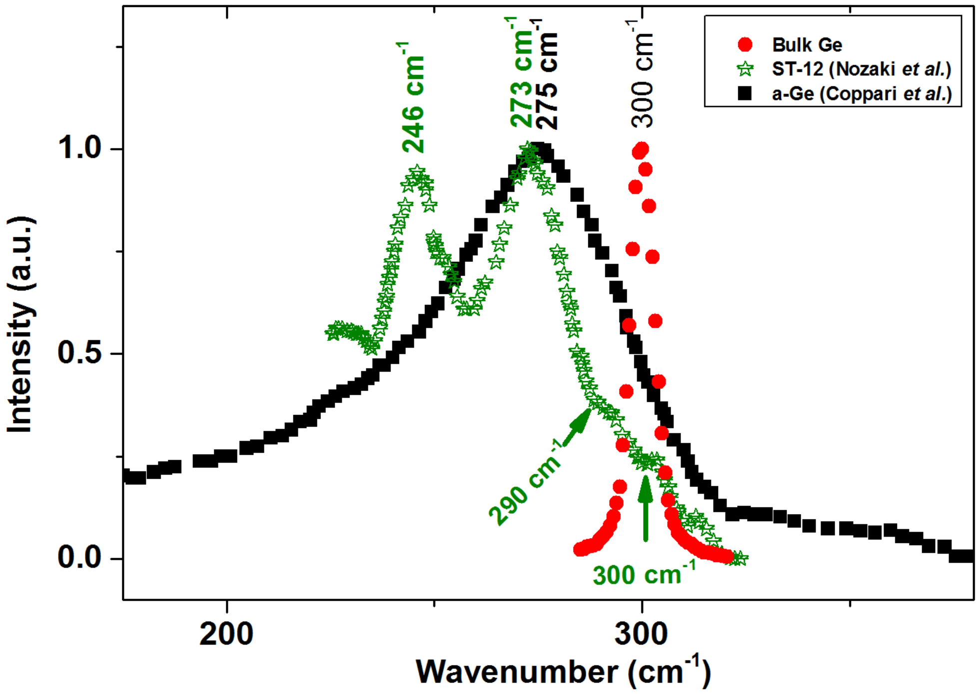

**Figure 3.4.2.2** Comparison of Raman shift of bulk Ge (the diamond cubic type), Ge in ST-12 phase and a-Ge. Bulk Ge has a peak position at 300 cm$^{-1}$. ST-12 phase of Ge obtained by cluster-beam evaporation technique (reproduced from (Nozaki *et al.*, 1999)) has two main bands at 246 cm$^{-1}$ and 273 cm$^{-1}$. There are also bands at 290 cm$^{-1}$ and 300 cm$^{-1}$. In a-Ge, there is one but a very broad and asymmetric peak at 275 cm$^{-1}$ (reproduced from (Coppari *et al.*, 2009)).

In Figure 3.4.2.2, Raman signals of bulk Ge in the diamond cubic structure are compared with that of Ge in ST-12 phase and a-Ge. As mentioned earlier, bulk Ge has a symmetric Lorentzian shape with a peak position at 300 cm$^{-1}$. ST-12 phase shows two main modes at 246 cm$^{-1}$ and 273 cm$^{-1}$ in addition to shoulders at 290 cm$^{-1}$ and 300 cm$^{-1}$, while a-Ge has a single and very broad asymmetric peak positioned at 275 cm$^{-1}$. None of these Raman signals seem to explain the residual small peak at 250 cm$^{-1}$ with only ST-12 structure showing anything at around that range.

### 3.4.2.2. TEM Data

The TEM data in Figure 3.4.2.3 clearly show the size of Ge dots and influence of increasing concentrations of $GeCl_4$ on the particle size ($CS_1$, Figure 3.4.2.3(a) and $CS_2$ Figure 3.4.2.3(b)). The analysis of TEM micrograph of $CS_1$ in Figure 3.4.2.3(a) shows the mean size of $CS_1$ to be 3.68 nm ± 0.62 nm with a very narrow size distribution out of 60 qdots of $CS_1$ in Figure 3.4.2.3(c). The results for $CS_1$ sample are consistent with the size extracted from the Raman data using RFC model. The mean size of $CS_2$ out of 60 qdots was found to be 10.15 nm ± 2.94 nm from the TEM micrograph in Figure 3.4.2.3(b) with the size distribution shown in Figure 3.4.2.3(d).

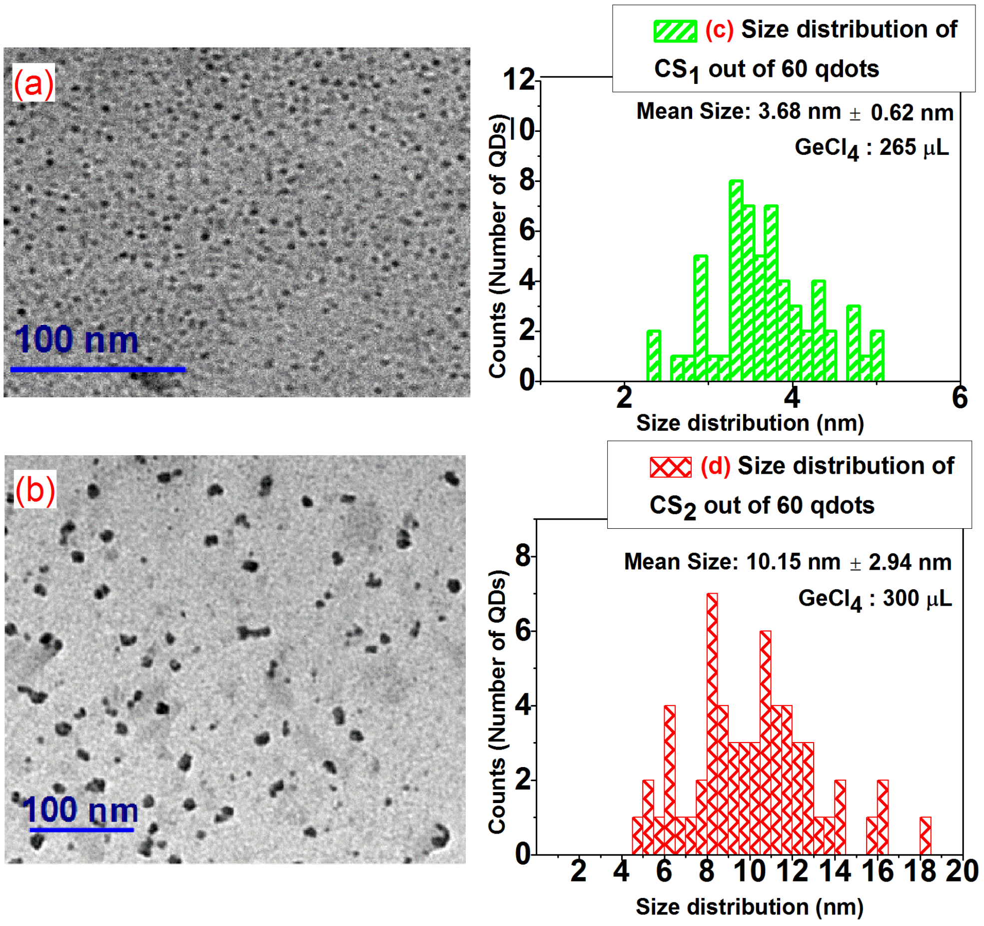

**Figure 3.4.2.3** TEM micrographs of (a) $CS_1$ and (b) $CS_2$ and the graphs in (c) and (d) are the size distributions of Ge qdots, $CS_1$ and $CS_2$ out of 60 qdots respectively.

The TEM micrograph of $CS_1$ as-prepared, shown in Figure 3.4.2.4, represents the area of SAED of $CS_1$. SAED in Figure 3.4.2.5 shows diffraction patterns, which are characteristics of Ge-I (diamond cubic) phase and also alpha-quartz type $GeO_2$. The spots are attributed to the reflections of diamond type Ge (222), Ge (133) and Ge (444) as the corresponding circles and planes are shown in blue (with yellow background) in Figure 3.4.2.5. The spots for the alpha-quartz type $GeO_2$ are less obvious (suggesting very little oxide presence), but drawn with circles in red for $GeO_2$ (011), $GeO_2$ (012) and $GeO_2$ $(\bar{1}21)$.

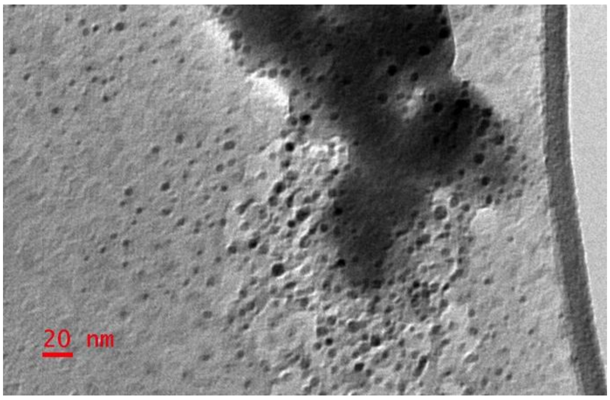

**Figure 3.4.2.4** TEM micrographs of $CS_1$ where SAED was recorded.

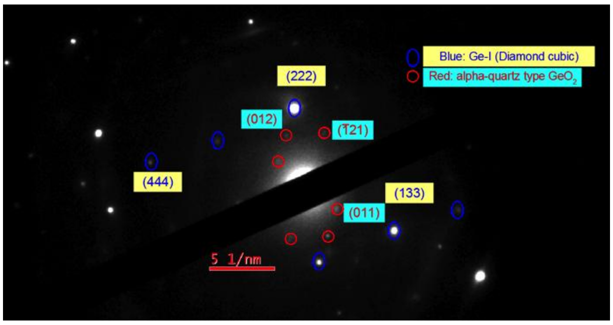

**Figure 3.4.2.5** SAED of Ge qdots shows spots, which are an indication of crystallisation in diamond cubic type, however, there are also reflections from alpha-quartz type $GeO_2$.

### 3.4.2.3. Extended Raman Spectroscopy and Effect of Annealing in $H_2$/Ar Gas Medium

Further treatment of $CS_1$ such as annealing in can be used to modify core/surface features of the Ge qdots, as it is regularly observed in embedded Ge qdots (Henderson, Seino, *et al.*, 2010; Wu *et al.*, 1997). The main objective of annealing of colloidal samples where to investigate the effect of temperature on the sample size. The effect of annealing of as-prepared samples in $H_2$/Ar were investigated using extended Raman spectrometry measurements and are shown in Figure 3.4.2.6. $CS_1$ samples annealed at 450 °C in $H_2$/Ar with a flow rate of 100 ccm are shown in Figure 3.4.2.6(b).

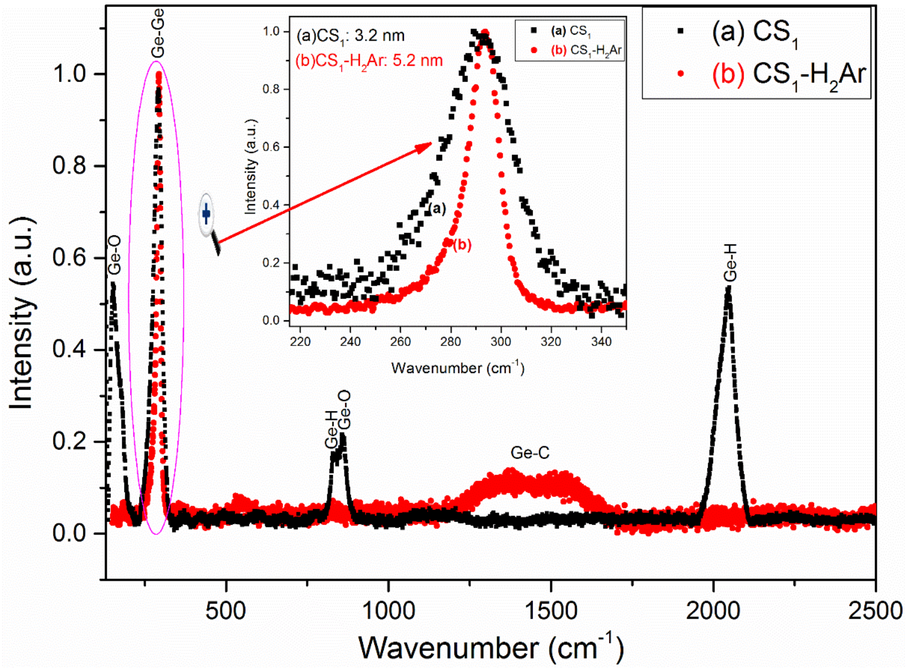

**Figure 3.4.2.6** Surface (Extended) Raman Spectroscopy Measurements of $CS_1$, $CS_1$-$H_2$Ar and $CS_1$-Ar. In case of $CS_1$, the broad peak around 2000 $cm^{-1}$ shows hydrogenation on the surface of the $CS_1$ and converted to the formation of Ge-C after annealing processes. The inset graph is the part zoomed in to the Ge-Ge (TO) bond vibration.

The size increase is confirmed by TEM measurements, and Raman spectroscopy results are also shown in the inset graph of Figure 3.4.2.6, with the size calculations according to the RFC model. After annealing of Ge qdots that were initially suspended in ethanol, Ge-H and Ge-O vibrational modes of the surface species of $CS_1$ diminish and have a tendency to be converted into Ge-C vibrational bands found at about 1500 $cm^{-1}$ by segregation of C atoms from ethanol (Su *et al.*, 2000). Hydride termination of Ge nanocrystals was reported by several authors with a broad stretching mode between 1900 $cm^{-1}$ to 2100 $cm^{-1}$ (Buriak, 2002; Mui, Han, Wang, Musgrave, & Bent, 2002; Su *et al.*, 2000). The broad peak centered at about 2000 $cm^{-1}$ in Figure 3.4.2.6 shows the Ge-H stretch mode of $CS_1$. In addition to the hydride termination there might also be a trace of $GeO_2$ polymorphs (Micoulaut *et al.*, 2006) - the bands assigned as 152 $cm^{-1}$, 450 $cm^{-1}$ and 858 $cm^{-1}$ may provide some evidence of those.

### 3.4.2.4. XRD and XAFS Data

Figure 3.4.2.7 shows powder XRD of Ge qdots ($CS_1$) which shows only one broad peak, suggesting Ge qdots are disordered or of a very small size. Using the Scherrer Equation (see Equation 2-1-4-2), the size of Ge qdots ($CS_1$) was found to be 1.58 nm, which is not consistent with TEM measurements (see Figure 3.4.2.3(a)). This may suggest amorphous nature of the sample, but the peak width (FWHM) extracted using a Gaussian fit of $CS_1$ was found to be 5.48º, which is half that expected for an amorphous Ge (around 10-15º). The corresponding *d*-spacing is calculated to be 3.97 Å using the Bragg law (see Equation 2-1-4-1). This lattice spacing is larger compared to the d-spacing (3.26 Å) for the main (111) reflection of the diamond cubic structure, and closer to (110) of ST-12 phase with 0.22 Å difference. This result contradicts the SAED results which showed mostly the diamond cubic structure of Ge, however, high energetic electrons in SAED can be thought of as a source of annealing (which is not the case for XRD measurements), and the sample may be transformed from ST-12 to the diamond cubic structure via annealing (Kim *et al.*, 2010).

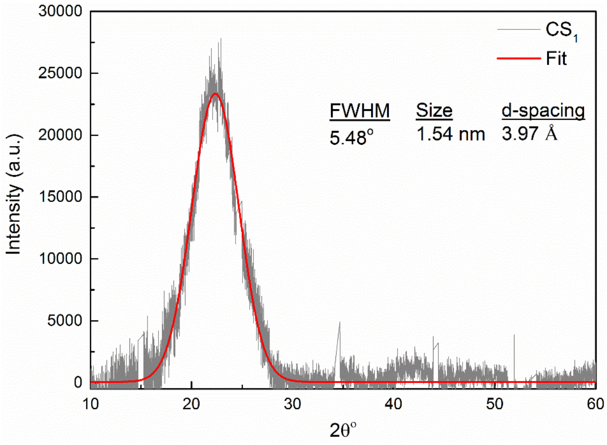

**Figure 3.4.2.7** XRD of Ge qdots as prepared ($CS_1$). The small peak-like shapes at about 35, 45 and 52 ° were due to the scattering from the detector window.

Figure 3.4.2.8(a) and (b) give EXAFS of $CS_1$ at Ge K-edge in *k*-space together with the FT magnitude in *r*-space respectively. The data in Figure 3.4.2.8(c) indicate that as-prepared $CS_1$ sample may be disordered (or made up of very small particles) since there is only single shell in the FT modulus of EXAFS of $CS_1$. This is consistent with the XRD data above.

**Table 3.4.2.1** The R-factor and interatomic distances extracted from the multiple shell fit of the FT modulus of EXAFS of Ge nanoparticles formed using $CS_1$. Alpha-quartz type $GeO_2$ and the diamond cubic Ge structure were used. The interatomic distance is in Å.

| **The fitting quality and parameters** | **$CS_1$ EXAFS** |
|---|---|
| R-factor | 0.004 |
| $R_{i1}$ ($Ge_1$-$Ge_2$) | 2.437 ± 0.011 |

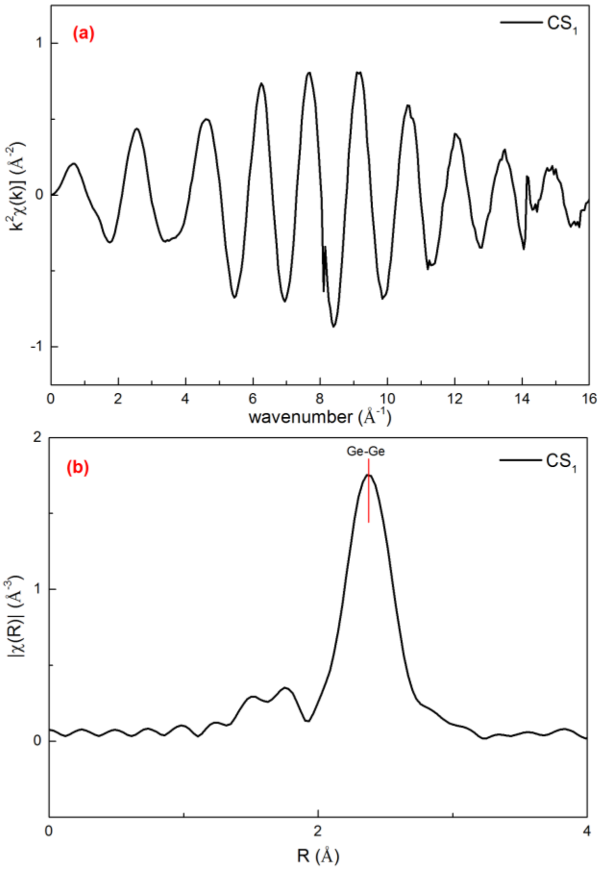

**Figure 3.4.2.8** EXAFS of Ge qdots (CS$_1$) at Ge K-edge (a) in *k*-space and (b) the FT modulus of EXAFS of CS$_1$ in *r*-space.

The FT modulus of EXAFS of CS$_1$ was fitted with the diamond cubic structure of Ge (see Table 3.4.2.1 and Figure 3.4.2.9). The single shell contributions of the diamond cubic structure of Ge are shown in Figure 3.4.2.9. The data in the Table 3.4.2.1 suggest that the first shell distance is close to that of diamond type Ge (see Table 3.1.3.1).

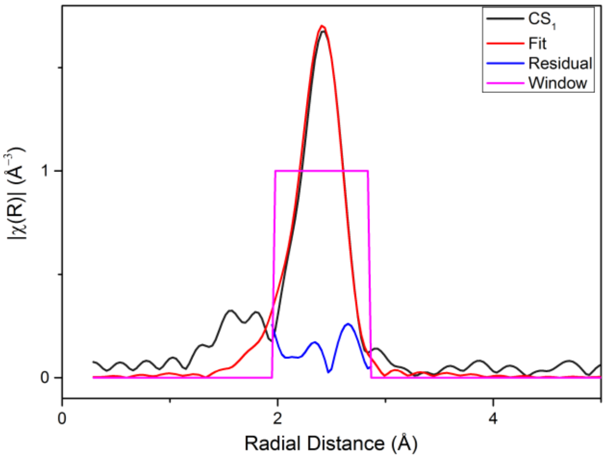

**Figure 3.4.2.9** The FT modulus of EXAFS of CS$_1$ (black colour) is compared with the fit (red colour), the residual between the fit and the data (blue colour) and the window of the fit (magenta colour).

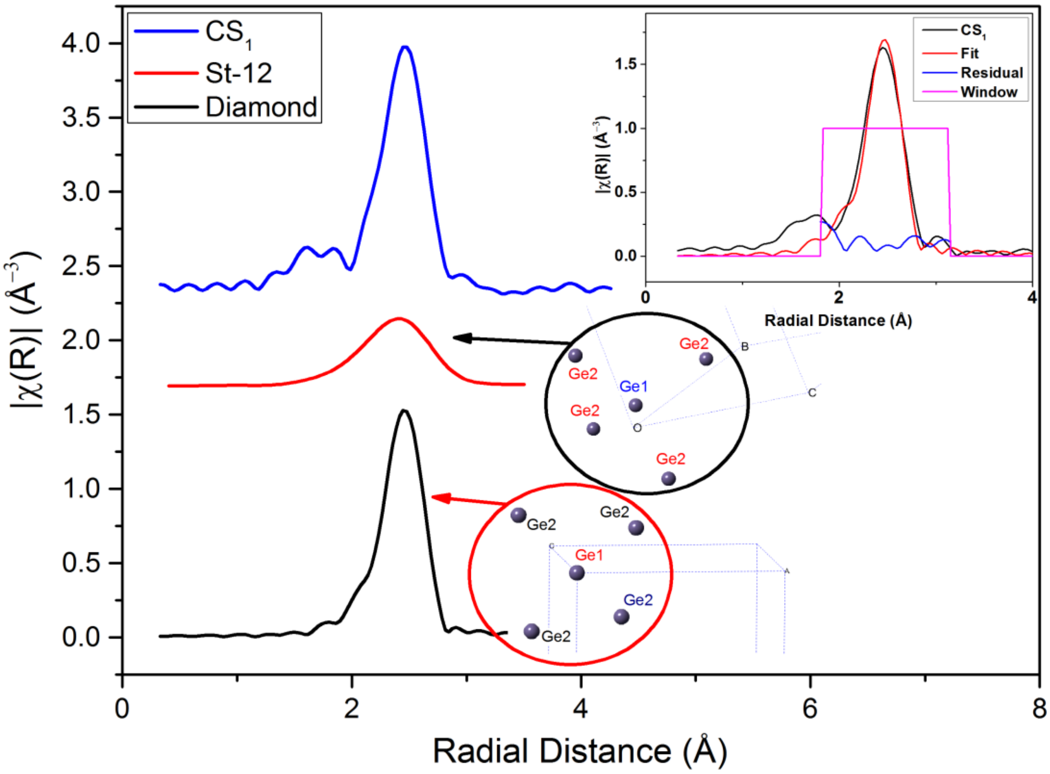

**Figure 3.4.2.10** The FT modulus of EXAFS of CS$_1$ and the individual contributions of the first shells of ST-12 phase and the diamond cubic structures. The inset figure shows the FT modulus of EXAFS of CS$_1$, the fit, the residual between the fit and the data and the window of the fit. The models of ST-12 phase and the diamond cubic type of Ge are shown. The range of the models was obtained between 0-3 Å for the first shells only.

We also tested for possible ST-12 contribution in addition to the diamond cubic structure. The data were fitted (see Table 3.4.2.2) with a combination of individual contributions of both ST-12 and the diamond cubic structures of Ge (mixed cluster model, see also inset in Figure 3.4.2.10).

**Table 3.4.2.2** The R-factor and interatomic distances extracted from the multiple shell fit of the FT modulus of EXAFS of Ge nanoparticles formed using $CS_1$. ST-12 phase and the diamond cubic Ge structures were used. The interatomic distances are in Å.

| **The fitting quality and parameters** | **$CS_1$ EXAFS** |
|---|---|
| R-factor | 0.023 |
| $R_{i1}$ ($Ge_1$-$Ge_1$) Diamond | 2.397 ± 0.023 |
| $R_{i2}$ ($Ge_1$-$Ge_2$) ST-12 | 2.448 ± 0.033 |

Results of the analysis suggest that although ST-12 structure may be present in significant amounts, see Figure 3.4.2.10. The reduction of interatomic distances as compared to diamond type (2.397 Å against 2.45 Å) and ST-12 ( 2.448 Å against 2.48 Å, see Table 3.4.2.2) can be explained by average bond length contraction due to size effects (see Pizzagalli, 2001). However, the quality of the fit for mixed cluster model is much lower (R-factor of 0.023) that that for diamond type Ge model (R-factor of 0.004).

XRD data for as-prepared $CS_1$-$H_2$ sample are shown in Figure 3.4.2.11. The size analysis using the Scherrer equation shows that as-prepared sample ($CS_1$-$H_2$) is smaller in size (1.38 nm) compared to the size of $CS_1$ (1.54 nm). The *d*-spacing corresponding to the main peak at around 22° corresponds to 3.97 Å just like in the case of $CS_1$ sample, suggesting that the two structures are similar.

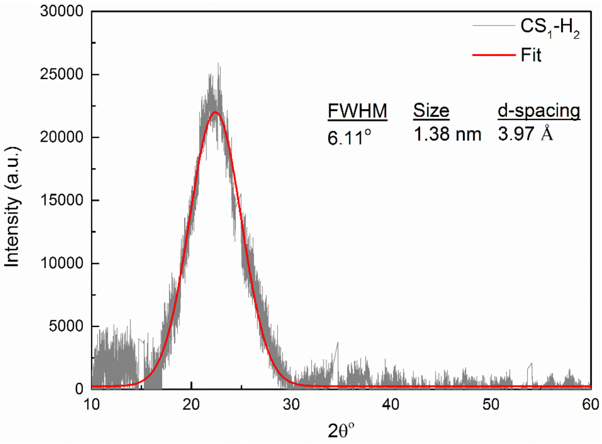

**Figure 3.4.2.11** XRD of Ge qdots as prepared (CS$_1$-H$_2$) which was prepared through the purging of H$_2$/Ar gas instead of Ar gas.

EXAFS data of CS$_1$-H$_2$ at Ge-K edge in *k*-space and FT magnitude in *r*-space are shown in Figure 3.4.2.12(a) and (b). The data in Figure 3.4.2.12(b) suggest there is only one single shell, as in the case of CS$_1$. This single shell seemed to correspond well to the diamond cubic structure as follows from the fit shown in Figure 3.4.2.13. The result of the fit is shown Table 3.4.2.3, which gives Ge atoms at an average distance of 2.439 ± 0.003 Å.

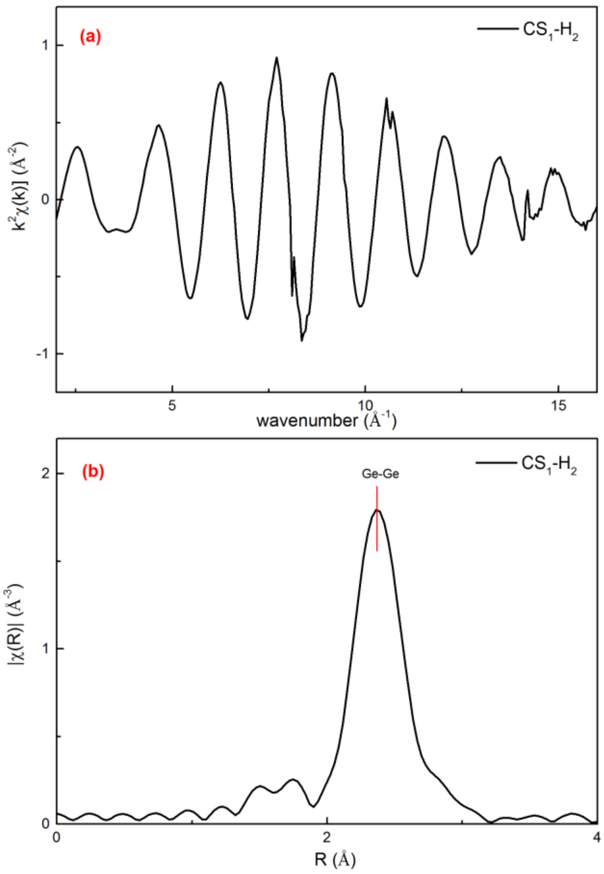

**Figure 3.4.2.12** EXAFS of Ge qdots ($CS_1$-$H_2$) at Ge K-edge (a) in *k*-space and (b) the FT modulus of EXAFS of $CS_1$-$H_2$ in *r*-space.

**Table 3.4.2.3** The R-factor and interatomic distances extracted from a single shell fit of the FT modulus of EXAFS of Ge nanoparticles formed using $CS_1$-$H_2$. The diamond cubic Ge structure was used as a structural model in the fit. The interatomic distance is in Å.

| **The fitting quality and parameters** | **$CS_1$-$H_2$ EXAFS** |
|---|---|
| R-factor | 0.018 |
| $R_{i1}$ ($Ge_1$-$Ge_2$) | 2.439 ± 0.003 |

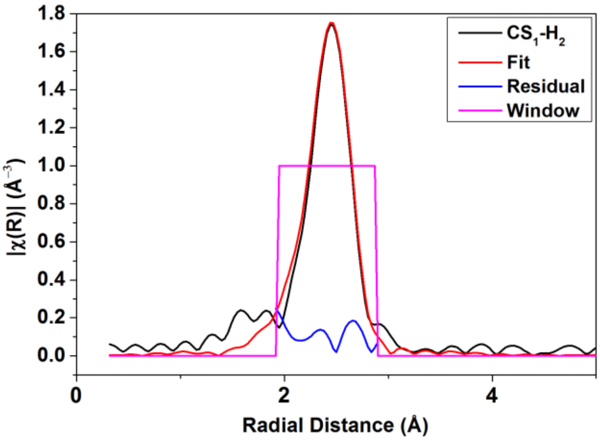

**Figure 3.4.2.13** The FT modulus of EXAFS of $CS_1$-$H_2$ (black colour) is compared with the fit (red colour), the residual between the fit and the data (blue colour) and the window of the fit (magenta colour). Only the diamond cubic structure was used as a structural model.

As in the case of $CS_1$, the fit with the ST-12 phase and the diamond cubic structure (mixed cluster) of Ge was obtained and the results are shown in Figure 3.4.2.14 and summarised in Table 3.4.2.4. In both cases, $CS_1$ (2.448 ± 0.033 Å) and $CS_1$-$H_2$ (2.432 ± 0.006 Å), the Ge-Ge distance within the ST-12 phase shows contraction when compared with experimental data (2.49 Å) at zero pressure (Mujica & Needs, 1993). However, in the case of $CS_1$-$H_2$ sample, the R-factor for the mixed cluster model is smaller (0.014, Table 3.4.2.4) than that from diamond type model (0.018, Table 3.4.2.3).

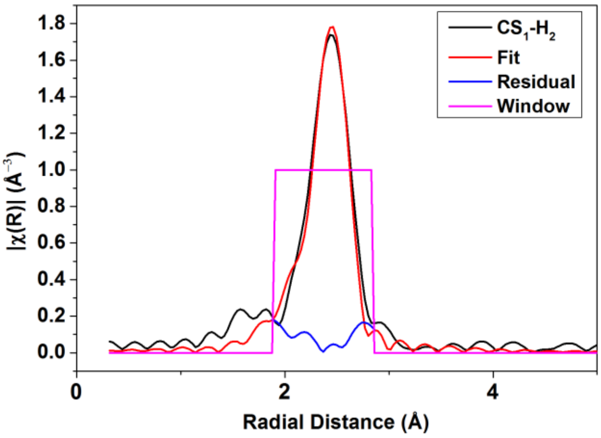

**Figure 3.4.2.14** The FT modulus of EXAFS of $CS_1$-$H_2$ at Ge K-edge, the fit, the residual between the fit and the data and the window. The models of the ST-12 phase and the diamond cubic type of Ge are used for the fit.

**Table 3.4.2.4** The R-factor and the interatomic distances extracted from the multiple shell fit of the FT modulus of EXAFS of Ge nanoparticles formed using CS1-$H_2$. ST-12 phase and the diamond cubic Ge structures were used. The interatomic distances are in Å.

| **The fitting quality and parameters** | **$CS_1$-$H_2$ EXAFS** |
|---|---|
| R-factor | 0.014 |
| $R_{i1}$ ($Ge_1$-$Ge_1$) Diamond | 2.400 ± 0.024 |
| $R_{i2}$ ($Ge_1$-$Ge_2$) ST-12 | 2.432 ± 0.006 |

As mentioned at the beginning of this section, as-prepared Ge qdots ($CS_1$) were annealed in a flow of $H_2$/Ar gas ($CS_1$-$H_2$Ar) and the core/surface modification was shown via Raman spectroscopy studies (see Figure 3.4.2.6). As usually shown in embedded samples, annealing can transform their amorphous components to crystalline (Henderson, Seino, *et al.*, 2010; Wu *et al.*, 1997). Figure 3.4.2.15 shows XRD data for $CS_1$-$H_2$Ar. Reflections corresponding to Ge (111), Ge (022) and Ge (113) of the diamond cubic structure can be clearly seen. The mean size of the crystallites in the diamond cubic structure is calculated as 33.3 nm using the

Scherrer equation. The reflections named $(XYZ)_1$ and $(XYZ)_2$ have the corresponding d-spacing values of 2.82 Å and 1.63 Å respectively and these can be ascribed to (021) and (230) of the ST-12 phase of Ge.

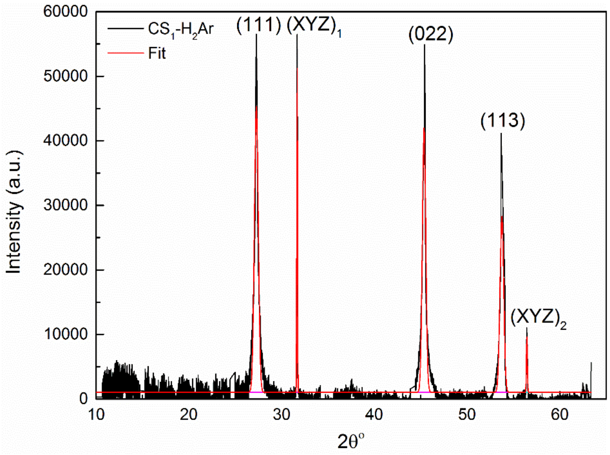

**Figure 3.4.2.15** XRD of Ge qdots ($CS_1$-$H_2Ar$) annealed in $H_2$/Ar medium at 450 ºC. The reflections show growth and crystallisation of Ge qdots due to the annealing process.

EXAFS data of $CS_1$-$H_2Ar$ at Ge-K edge in *k*-space and FT magnitude in *r*-space are also shown in Figure 3.4.2.16(a) and (b) respectively. Figure 3.4.2.16(b) shows the first and the second shells ($Ge_1$:$Ge_2$ and $Ge_1$:$Ge_3$), which demonstrate the characteristics of a crystalline feature in the local range. The FT modulus of EXAFS of $CS_1$-$H_2Ar$ fit well with the diamond cubic structure of Ge (see Table 3.4.2.5). However, the data in Figure 3.4.2.16(b) seem to show that at about 3.8 Å we have one more contribution just before the second shell of the diamond cubic structure of Ge.

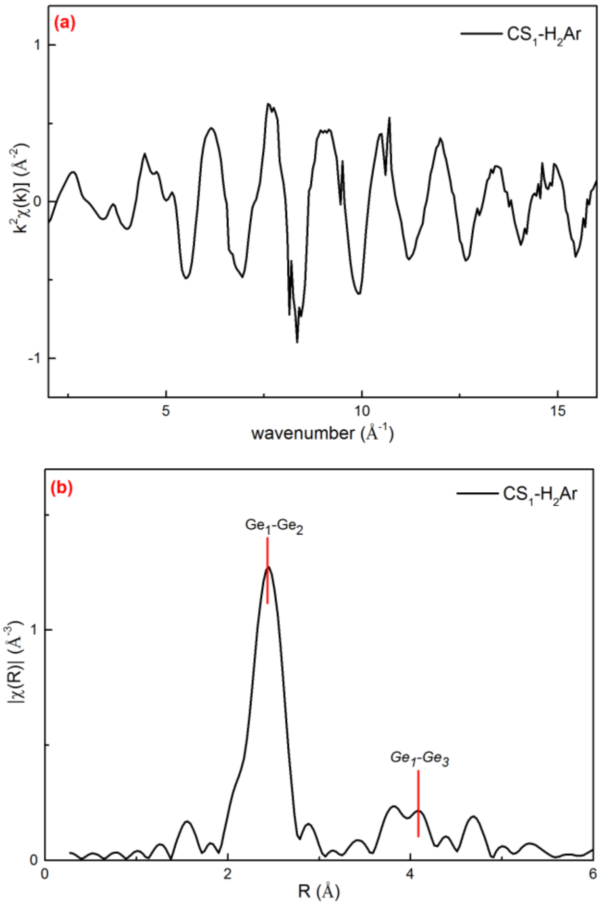

**Figure 3.4.2.16** EXAFS of annealed Ge qdots (CS$_1$-H$_2$Ar) at Ge K-edge (a) in *k*-space and (b) FT modulus of EXAFS in *r*-space.

**Table 3.4.2.5** The R-factor and interatomic distances extracted from the multiple shell fit of the FT modulus of EXAFS of Ge nanoparticles formed using CS$_1$-H$_2$Ar. Only the diamond cubic structure was used for the fit. The interatomic distances are in Å.

| **The fitting quality and parameters** | **CS$_1$-H$_2$Ar EXAFS** |
|---|---|
| R-factor | 0.038 |
| $R_{i1}$ (Ge$_1$-Ge$_2$) | 2.449 ± 0.005 |
| $R_{i2}$ (Ge$_1$-Ge$_3$) | 4.005 ± 0.021 |

XRD of CS$_1$-H$_2$Ar in Figure 3.4.2.15 suggests the presence of the ST-12 phase in CS$_1$-H$_2$Ar upon annealing and, therefore, it may also be possible to observe these contributions in EXAFS. The mixed cluster fit in Figure 3.4.2.17 shows the individual contributions of the diamond cubic structure ($Ge_1$-$Ge_2$ and $Ge_1$-$Ge_3$ with black colour) and ST-12 phase of Ge ($Ge_1$-$Ge_6$ with red colour).

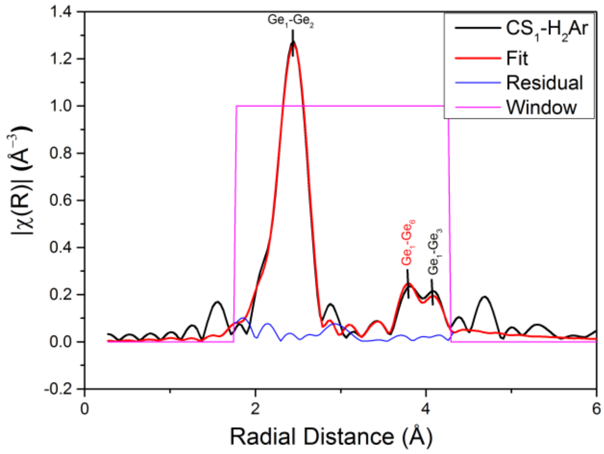

**Figure 3.4.2.17** The FT modulus of EXAFS of $CS_1$-$H_2$Ar at Ge K-edge, the fit, the residual between the fit and the data and the window. The diamond cubic type of Ge and the ST-12 phases were used.

**Table 3.4.2.6** The R-factor and interatomic distances extracted from the multiple shell fit of the FT modulus of EXAFS of Ge nanoparticles formed using $CS_1$-$H_2$. The diamond cubic structure and ST-12 phase of Ge were used for the fit. The distances are in Å.

| **The fitting quality and parameters** | **$CS_1$-$H_2$Ar EXAFS** |
|---|---|
| R-factor | 0.037 |
| $R_{i1}$ ($Ge_1$-$Ge_2$) (Diamond) | 2.451 ± 0.004 |
| $R_{i2}$ ($Ge_1$-$Ge_6$) (ST-12 phase) | 3.887 ± 0.039 |
| $R_{i3}$ ($Ge_1$-$Ge_3$) (Diamond) | 4.035 ± 0.022 |

The fitted second shell of ST-12 structure gives the distance of 3.887 ± 0.039 Å, which falls within the range of values of 3.45 Å and 4 Å for second shell distances in ST-12 structure, (see section 1.1.2). However, the improvement in the fit (R-factor of 0.037, Table 3.4.2.6) compared to the diamond type structure (R-factor of 0.038, Table 3.4.2.5) is marginal.

## Summary of the Results

The results for $CS_1$ sample can be summarised as follows:

- Size of Ge nanoparticles was found to be 1.54 nm by XRD and 3.68 ± 0.6 nm by TEM and 3.2 ± 0.3 nm by the Raman spectroscopy.
- PL spectroscopy shows an emission peak approximately at 680 nm (1.82 eV) which is not inconsistent with the theoretical models (tight binding model and k.p perturbation theory) (Figure 1.2.1.5) for nanoparticles of around 3 nm in size.
- XRD shows a significant degree of disorder and the main XRD peak is not that of the diamond type structure, but can be is assigned to ST-12 phase of Ge.
- EXAFS data confirm the large level of disorder in the sample and provide interatomic distances, but inconclusive as far as ST-12 and diamond type phases are concerned.
- Following annealing at in $H_2$/Ar medium at 450 $^{o}$C samples show clear reflections corresponding to diamond type Ge. However, some extra reflections are also present that can be tentatively assigned to ST-12 phase.

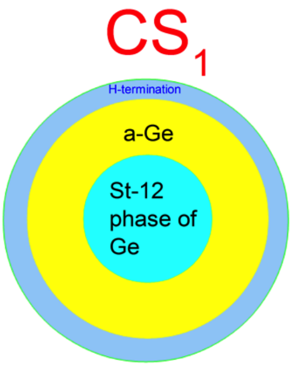

**Figure 3.4.2.18** Schematic representation of as-prepared Ge qdots formed using $CS_1$ in supra-atomic scale showing a nanocrystalline Ge core of ST-12 phase surrounded with disordered Ge qdots and H-terminated surface.

Thus, the peak of PL emission of $CS_1$ is consistent with the theoretical QCE models for 3 nm Ge nanoparticles (Figure 1.2.1.5), but is at odds with the experimental data (Figure 1.2.1.4). Analysis of discrepancies of sizes extracted from TEM, Raman and XRD can be explained by the structural disorder present in as-prepared samples. This is consistent with the corresponding EXAFS and XRD data. However, samples may not consist of a single amorphous phase as indicated by the XRD peak width (see Figures 3.4.2.7 and 3.4.2.11) and the corresponding discussions in Section 3.4.2.4. In other words, presence of a small crystalline core is not inconsistent with our data. In addition, the surface must be terminated by oxygen, hydrogen or any other species. Oxygen termination would have been observed in EXAFS as Ge-O signal, but we do not see a shell corresponding to Ge-O distance. In fact, we see no signal that can be associated with the surface. This may suggest hydrogen termination, as hydrogen scattering amplitudes are too low to be detected by EXAFS.

To summarise, there could be several possibilities in general for the morphology of as-prepared $CS_1$ Ge nanoparticles: (i) crystalline; (ii) amorphous;

(iii) mixture of crystalline and amorphous nanoparticles; (iv) single qdots with a nanocrystalline core and an amorphous shell. Analysis of discrepancies of sizes extracted from TEM and Raman together with EXAFS and XRD data suggests that disorder must be present in our samples as discussed above. This excludes case (i) above. As discussed above, XRD data also suggest that the long-range order in our as-prepared Ge qdots is better than that in amorphous Ge, thus excluding case (ii). A mixture of nano-crystalline and nano-amorphous sample with the particle size observed in TEM would result in observation of second (and possibly further) coordination shells in EXAFS data, which is not the case for as-prepared samples. Moreover, a mixture of single crystalline and amorphous Ge qdots would result in a non-Gaussian shape (broad amorphous background with a sharp crystalline peak on top) rather than Gaussian diffraction peak we observe. Hence we can exclude case (iii).

Therefore, we think that the most likely model for as-prepared Ge qdots is a core-shell - case (iv) above. We believe that the model represented - the crystalline core surrounded by amorphous surface - can explain the discrepancy in the size estimations between XRD (1.54 nm), TEM (3.68±0.62 nm) and Raman measurement (3.2 nm). This suggests that $CS_1$ can be described by the core-shell model with a crystalline core, and an amorphous outer shell and hydrogen-terminated surface (see Figure 3.4.2.18).

### 3.4.3. The Benchtop Colloidal Synthesis Method II ($Ca_1$): Formation of Ge Quantum Dots by Reduction from $GeO_2$

#### 3.4.3.1. Raman and PL Spectroscopy

Two samples have been studied by Raman and PL spectroscopy: $Ca_{1d}$ (brown coloured sample, also referred to as simply $Ca_1$) and $Ca_{1a}$ (yellow coloured sample, see sample preparation chapter). The PL and Raman data for as-prepared $Ca_{1d}$ are shown in Figure 3.4.3.1(a). The size of as-prepared Ge qdots were found to be 2.7 nm using the phonon confinement model (Campbell & Fauchet, 1986; Richter *et al.*, 1981) as represented in Figure 3.4.3.1(a). PL spectroscopy of as-prepared Ge qdots in Figure 3.4.3.1(b) shows emission in the near infrared region at about 810 nm (1.53 eV).

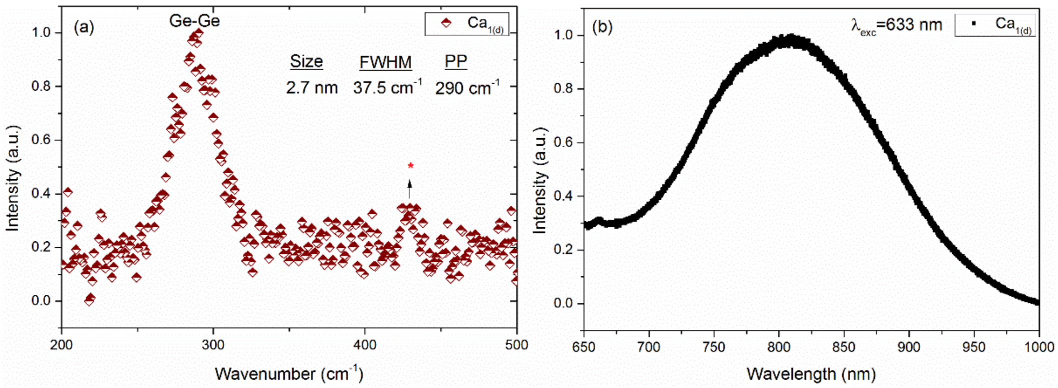

**Figure 3.4.3.1** (a) Raman shift and (b) Photoluminescence of Ge qdots ($Ca_{1d}$). A He-Ne laser was utilised at 633 nm excitation wavelength for both the Raman and PL spectroscopy measurements.

The size change of Ge qdots from $Ca_{1a}$ (early in the synthesis) to $Ca_{1d}$ (late in the synthesis is demonstrated in Figure 3.4.3.2(a). The size of $Ca_{1a}$ was found to be 2.4 nm using the phonon confinement model (Campbell & Fauchet, 1986; Richter *et al.*, 1981) and is shown in Figure 3.4.3.2(a). PL spectra in Figure 3.4.3.2(b) were observed to change significantly as sized is reduced from $Ca_{1d}$ to $Ca_{1a}$. We used multiple Gaussian fitting to obtain peak positions. Three Gaussian peaks were used in fitting $Ca_{1a}$ spectrum, while two Gaussian peaks were used to fit $Ca_{1d}$ data as introducing a third peak did not improve the quality of the fit. The peak detected at 668 nm in Figure 3.4.3.2(b) for $Ca_{1a}$ was reduced significantly in intensity in $Ca_{1d}$ and shifted to the shorter wavelength of 661 nm. There is also a shoulder in Figure 3.4.3.2(b) corresponding to the peak at 738 nm in $Ca_{1a}$, but is absent in $Ca_{1d}$.

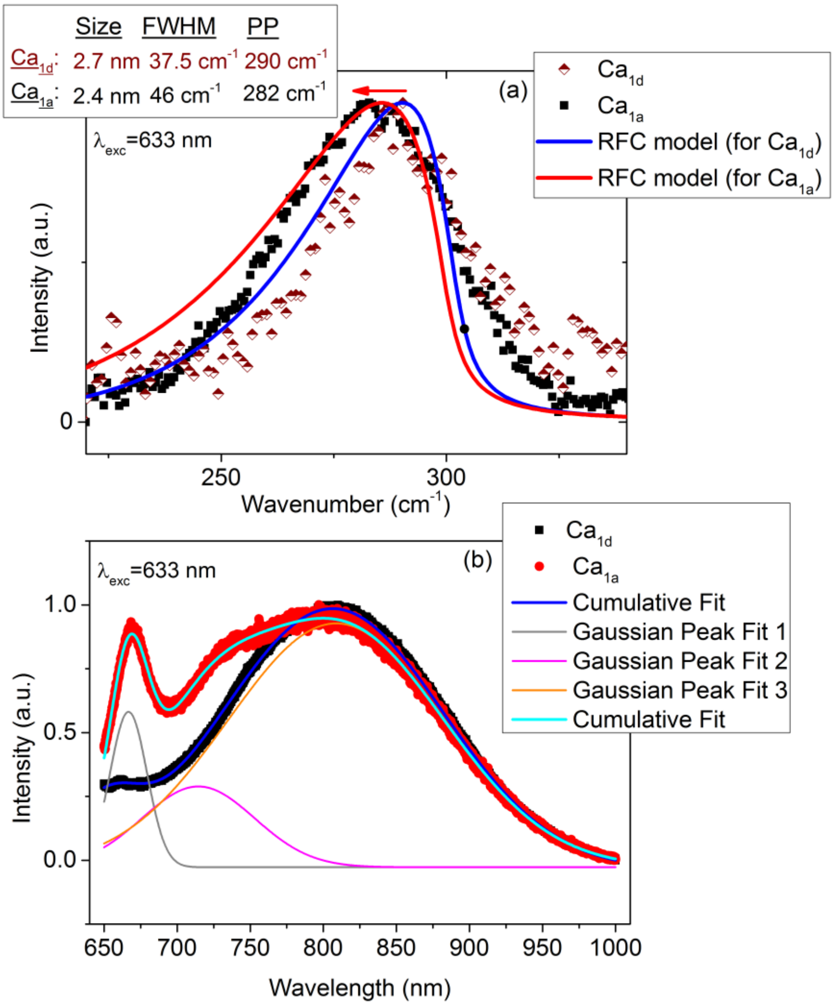

**Figure 3.4.3.2** (a) Raman spectroscopy data of $Ca_{1a}$ and $Ca_{1d}$ show the variation in the sample size together with the RFC model fittings. (b) PL spectroscopy data of $Ca_{1a}$ and $Ca_{1d}$. A multi-peak Gaussian fit to the PL of $Ca_{1a}$ shows three main peaks at 668 nm (1.85 eV), 738 nm (1.68 eV) and 808 nm (1.53 eV). For the PL of $Ca_{1d}$, a peak at 808 nm (1.53 eV) was observed in addition to a peak at 661 nm (1.88 eV). Gaussian peak fits are shown only for $Ca_{1(a)}$ for clarity.

### 3.4.3.2. TEM Data

There was a sufficient amount of $Ca_{1a}$ sample collected to conduct Raman and PL measurements, but not enough to record TEM, XRD and EXAFS data. Therefore we only show the results for $Ca_{1d}$ sample and refer to it simply as $Ca_1$.

Size and morphology of as-prepared Ge qdots ($Ca_1$) were investigated using TEM, as shown in Figure 3.4.3.3(a). The TEM micrograph of $Ca_1$ shows the mean size of as-prepared Ge qdots ($Ca_1$) to be 4.2 nm ±1.7 nm, and which are mostly spherical. Size distribution of Ge qdots ($Ca_1$) is also shown in Figure 3.4.3.3(b).

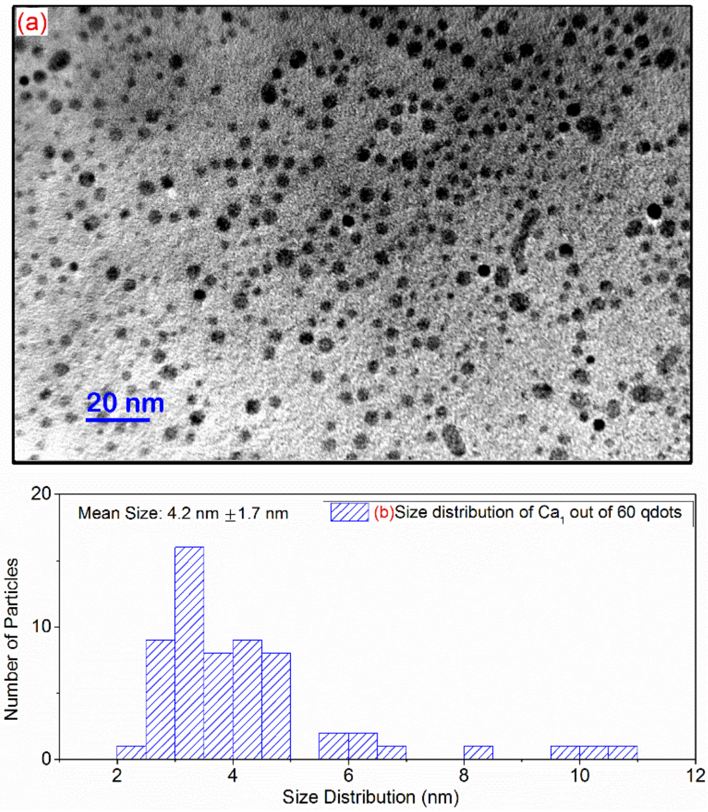

**Figure 3.4.3.3** TEM micrographs of $Ca_1$ and (b) the size distributions of Ge qdots, $Ca_1$ out of 60 qdots.

In Figure 3.4.3.4(a) and (b), the TEM micrograph of $Ca_1$ with higher magnification and SAED from this area is given respectively. Three different phases, the diamond cubic structure, ST-12 phase and the alpha-quartz type $GeO_2$

were assigned in $Ca_1$ as shown in Figure 3.4.3.4(b). Some spots are attributed to the reflections of the diamond cubic Ge (022), Ge (133), Ge (044) and Ge (444) (also designated with the blue circles in Figure 3.4.3.4(b)). Other spots correspond to the alpha-quartz type $GeO_2$ and are marked with circles in red for $GeO_2$ $(\bar{1}20)$ plane in Figure 3.4.3.4 (b). The spots for ST-12 phase with Ge (220) and Ge (222) reflections are marked with green circles.

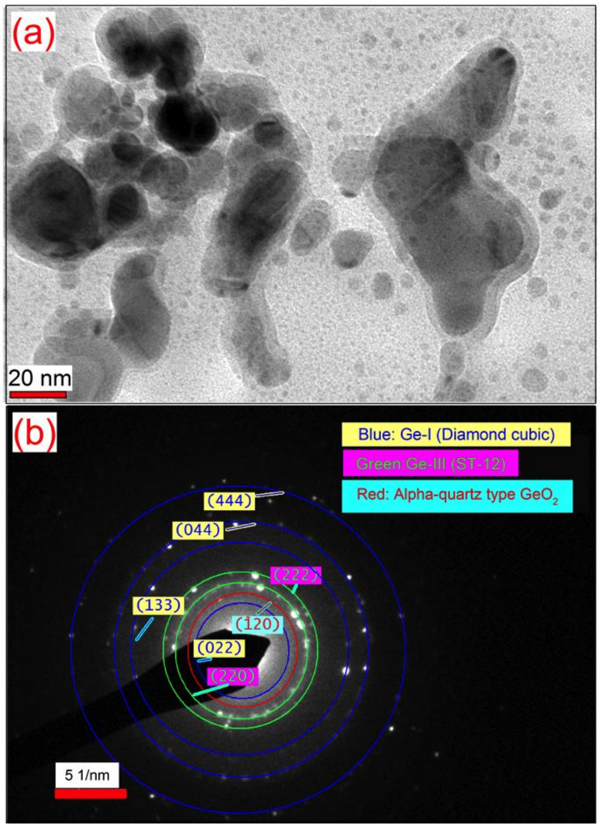

**Figure 3.4.3.4** (a) TEM micrograph of $Ca_1$ with higher magnification [25] (b) SAED of Ge qdots shows spots, which shows crystallisation mostly in the diamond cubic type of Ge, however, there are also reflections which were assigned to the ST-12 phase of Ge and the alpha-quartz type $GeO_2$.

---

[25] The shape of nanoparticles may be seen as not spherical which is due to fact that they were placed one on top of another, since the other areas, as given in Figure 3.4.3.3, show the spherical nanoparticles on average.

In addition to SAED, we have been able to obtain high resolution TEM images from some of which we could obtain lattice spacing by direct measurements from the fringes observed in high resolution TEM micrographs, or take the fast Fourier transform (FFT) of the area in which the fringes are observed and construct a simulation of the corresponding SAED (Taylor *et al.*, 1999). Figure 3.4.3.5(a) shows the TEM micrograph of $Ca_1$ at higher magnification. The FFT of the area from a particle pointed out by an arrow in Figure 3.4.3.5(a) was taken, and is shown in Figure 3.4.3.5(b). The spots from the simulated SAED were found to match with the reflections from Ge (111) and Ge (002) of the diamond cubic structure of Ge, as the corresponding circles and planes are marked with blue circles. Additionally, the reflections of Ge (120) and Ge (220) of ST-12 phases of Ge were also observed and are marked with green squares (see Figure 3.4.3.5(b)). These results are consistent with the SAED of $Ca_1$ in Figure 3.4.3.4(b).

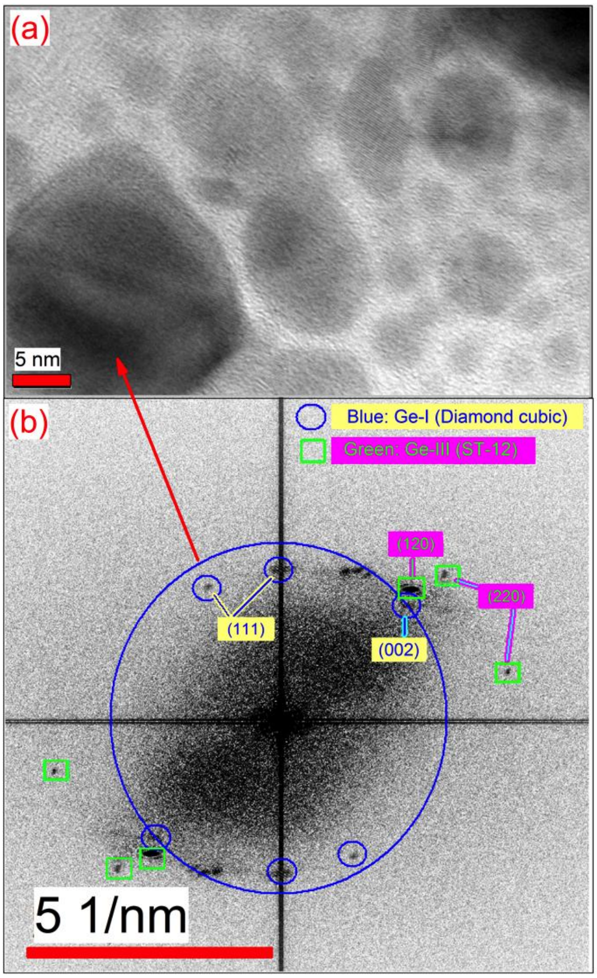

**Figure 3.4.3.5** (a) TEM micrograph of Ca$_1$ in higher magnification. (b) The fast Fourier transform (FFT) from the whole area of (a) shows spots which matches with Ge-I (diamond cubic type) and Ge-III (ST-12) phases.

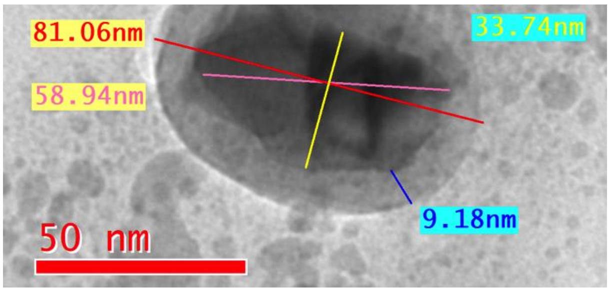

**Figure 3.4.3.6** TEM micrograph of a large particle shows a core-shell structure.

In addition, in some TEM micrographs we observed something that looked like a core-shell structure, although the particle is quite a large one, as shown in Figure 3.4.3.6.

### 3.4.3.3. XRD and XAFS Data

The XRD data for $Ca_1$ are shown in Figure 3.4.3.7. Using the Gaussian fit, the FWHM of XRD of $Ca_1$ was found to be 8.19° and the corresponding *d*-spacing was found to be 3.25 Å using the Bragg law (see page 33 for Equation 2-1-4-1). The d-spacing value matches with the face of (111) of the diamond cubic structure of Ge. The estimated size of the crystallites with the diamond cubic structure was found to be 0.98 nm, which is not consistent with the average size found by TEM (4.2 nm ±1.7, see Figure 3.4.3.3(a)). Furthermore, the second diffraction peak in Figure 3.4.3.7 can be assigned to the alpha-quartz type $GeO_2$ with a width of 5.93°, the *d*-spacing of 2.13 Å and an average size of 1.5 nm.

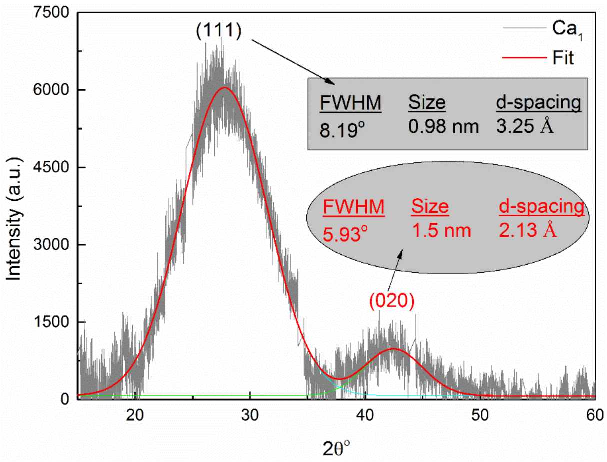

**Figure 3.4.3.7** XRD of $Ca_1$ shows diffraction peaks from Ge-I (Diamond cubic) phase and alpha quartz type $GeO_2$.

An investigation of short-range order of as-prepared Ge qdots ($Ca_1$) was performed with EXAFS at Ge K-edge. The *k*-space EXAFS data and a corresponding FT magnitude in *r*-space are shown in Figure 3.4.3.8(a) and (b) respectively.

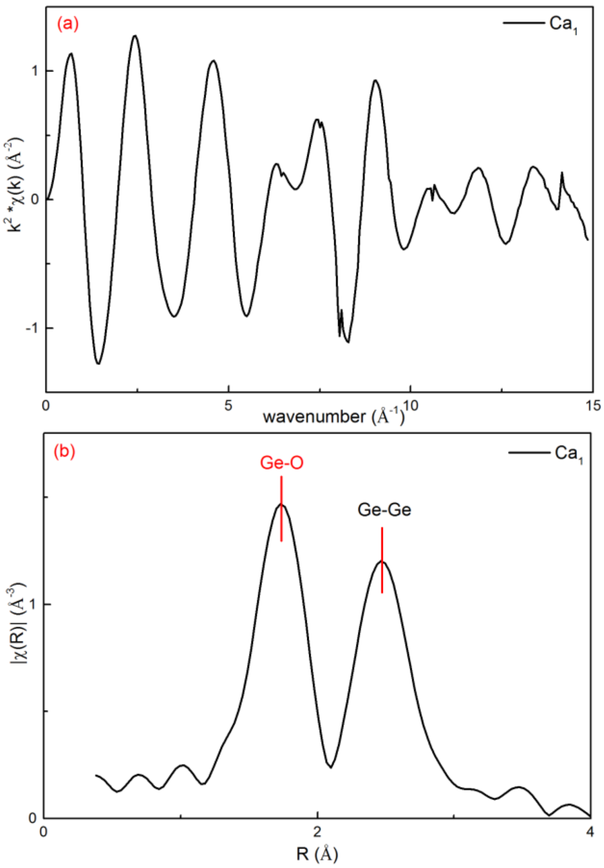

**Figure 3.4.3.8** EXAFS of Ge qdots ($CS_1$) over Ge K-edge (a) in *k*-space and (b) the FT modulus in *r*-space.

Figure 3.4.3.8 clearly shows two main shells unlike in the case of $CS_1$ sample where only single shell was observed (see Figure 3.4.2.12). Preliminary analysis indicates that second shell did not correspond to that of Ge-O-Ge distance in $GeO_2$ (around 3 Å) and is most likely due to Ge-Ge bond in a pure Ge phase. Therefore, we used mixed cluster model ($GeO_2$ and diamond type Ge, based on XRD data) to fit the data. The fitting results are shown in Figure 3.4.3.9 and the extracted data are given in Table 3.4.3.1. One can conclude that the sample is a mixture of disordered alpha-quartz $GeO_2$ and Ge phases. However, the Ge-Ge distance for the Ge phase is slightly longer (2.467 ± 0.006 Å) than that found in diamond type Ge (2.446 ± 0.003 Å, see Table 3.1.3.1). This may suggest a contribution from ST-12 structure for which interatomic distance is 2.48 Å, however further quantitative analysis is not possible due to restrictions on the number off parameters one can use in the fitting (see Equation A-2 in Appendix).

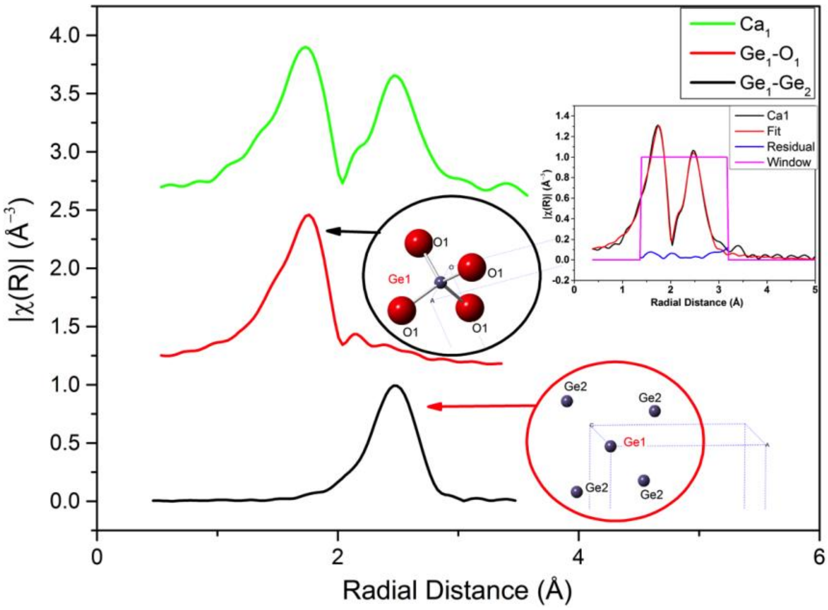

**Figure 3.4.3.9** The FT modulus of EXAFS of $Ca_1$ and the individual contributions of the first shells of the alpha-quartz type $GeO_2$ and the diamond cubic structures. The inset figure shows the FT modulus of EXAFS of $Ca_1$, the fit, the residual between the fit and the data and the window of the fit. The models of the alpha-quartz type $GeO_2$ and the diamond cubic type of Ge are shown.

**Table 3.4.3.1** The R-factor and interatomic distances (in Å) extracted from the multiple shell fit of the FT modulus of EXAFS of Ge nanoparticles formed using $Ca_1$.

| **The fitting quality and parameters** | **$Ca_1$ EXAFS** |
|---|---|
| R-factor | 0.005 |
| $R_{i1}$ ($Ge_1$-$O_2$) | 1.763 ± 0.005 |
| $R_{i2}$ ($Ge_1$-$Ge_2$) | 2.467 ± 0.006 |

The effect of annealing was investigated on as-prepared Ge qdots ($Ca_1$) at 450 $^{o}$C ($Ca_1$-$H_2$Ar450$^{o}$C sample). XRD of $Ca_1$-$H_2$Ar450$^{o}$C is given in Figure 3.4.3.10, which shows diffraction peaks corresponding to the planes of (111), (022) and (113) of the diamond cubic structure. Some of the oxides were also observed ((010) broad peak of alpha-quartz $GeO_2$), therefore not removed completely at the end of 1 hour of annealing at 450 °C in $H_2$/Ar gas medium.

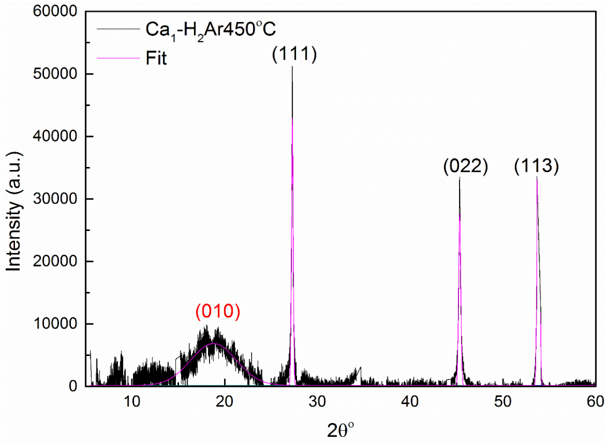

**Figure 3.4.3.10** XRD of Ge qdots ($Ca_1$-$H_2$Ar450°C) annealed in $H_2$/Ar medium at 450 °C. The reflections (111), (022) and (113) show crystallisation of Ge qdots in the diamond cubic structure after the annealing process. The broad (010) peak is of the alpha-quartz type $GeO_2$.

EXAFS at Ge K-edge in *k*-space and *r*-space FT modulus are shown in Figure 3.4.3.12(a) and Figure 3.4.3.12(b) respectively. The two shells are assigned to the alpha-quartz type $GeO_2$ and the diamond cubic structure of Ge. The Ge-O feature is noticeably reduced in amplitude (Figure 3.4.3.12(b)) compared to the as-prepared sample (Figure 3.4.3.11), as expected. Shells beyond the first Ge-Ge neighbours are not obvious, which may suggest possible long-range disorder. Table 3.4.3.2 also shows some evidence of the disorder, since the first shell of the alpha-quartz type $GeO_2$ and the first shell distance of the diamond cubic structure of Ge is slightly longer than in bulk Ge.

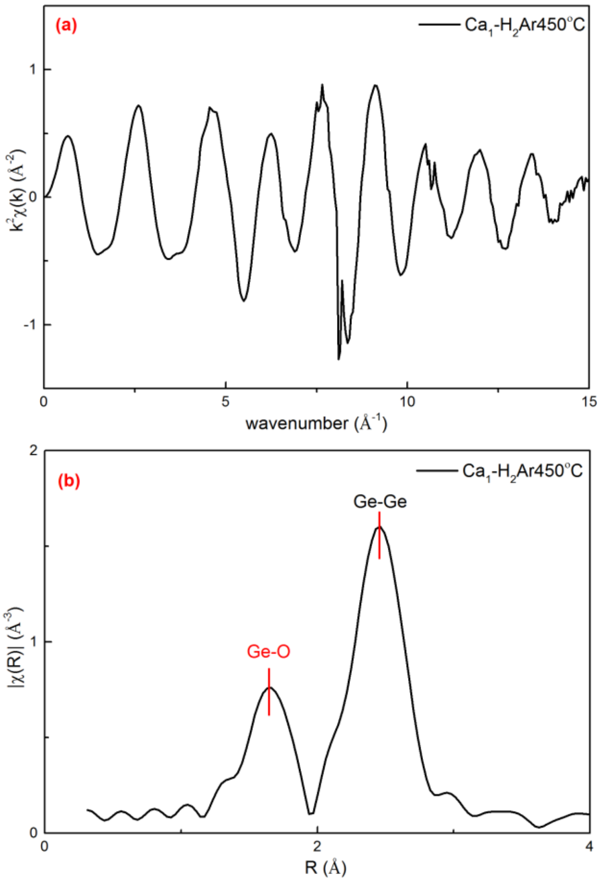

**Figure 3.4.3.12** EXAFS of Ge qdots (Ca$_1$-H$_2$Ar450$^o$C) at Ge K-edge (a) in *k*-space and (b) the FT modulus in *r*-space.

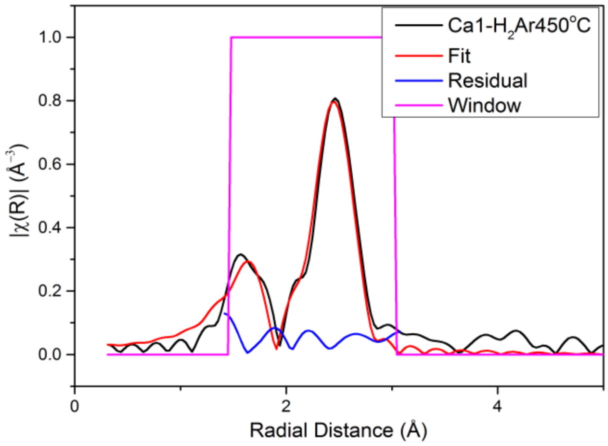

**Figure 3.4.3.13** The FT modulus of EXAFS of Ca$_1$-H$_2$Ar450$^o$C, the fit, the residual between the fit and the data and the window of the fit. The alpha-quartz type GeO$_2$ and the diamond cubic type of Ge are used for the fit.

**Table 3.4.3.2** The R-factor and interatomic distances extracted from the multiple shell fit of the FT modulus of EXAFS of Ge nanoparticles formed using $Ca_1$-$H_2$Ar450 °C. The interatomic distances are in Å.

| **The fitting quality and parameters** | **$Ca_1$-$H_2$Ar450 °C EXAFS** |
|---|---|
| R-factor | 0.012 |
| $R_{i1}$ ($Ge_1$-$O_2$) | 1.763 ± 0.015 |
| $R_{i2}$ ($Ge_1$-$Ge_2$) | 2.461 ± 0.005 |

As-prepared Ge qdots ($Ca_1$) were also investigated in the case of annealing at 600 °C in $H_2$/Ar gas medium ($Ca_1$-$H_2$Ar600°C sample). Crystallisation in the diamond cubic structure of Ge was observed in XRD of $Ca_1$-$H_2$Ar600°C, as shown in Figure 3.4.3.14 where the reflections of the diamond cubic Ge(111), Ge(022), Ge(113) can be seen. In Figure 3.4.3.14, in addition to the diamond cubic structure of Ge, there are two more reflections named $(XYZ)_1$ and $(XYZ)_2$ with *d*-spacing values of 2.82 Å and 1.63 Å respectively, which may correspond to the ST-12 structure. In SAED of as-prepared Ge qdots ($Ca_1$), the existence of the ST-12 phase was already observed and was believed to form via the annealing of Ge qdots due to highly energetic electrons (see Figure 3.4.3.4). Thermal annealing (Kim *et al.*, 2010) and cluster beam evaporation (Nozaki *et al.*, 1999; Sato *et al.*, 1995) techniques can also cause the formation of the ST-12 phase. Therefore, $(XYZ)_1$ and $(XYZ)_2$ in Figure 3.4.3.14 can be attributed to the planes (021) and (222) of the ST-12 phase.

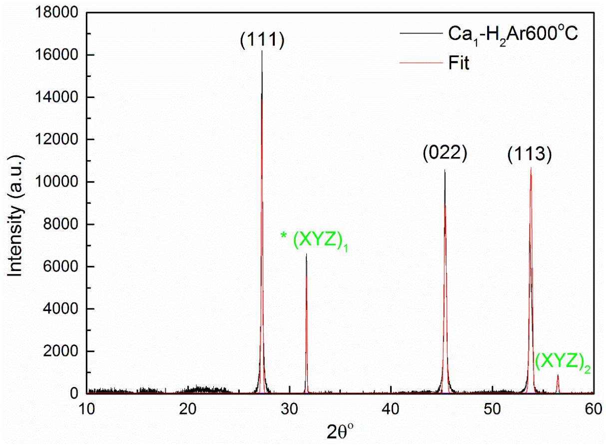

**Figure 3.4.3.14** XRD of Ge qdots (Ca$_1$-H$_2$Ar600°C) annealed in H$_2$/Ar medium at 600 °C. The reflections (111), (022) and (113) show crystallisation of Ge qdots into the diamond cubic structure of Ge after annealing process. (XYZ)$_1$ and (XYZ)$_2$ were assigned to (012) and (222) of ST-12 phase of Ge.

The EXAFS of Ca$_1$-H$_2$Ar600°C at Ge K-edge in *k*-space and FT magnitude in *r*-space are shown in Figure 3.4.3.15(a) and Figure 3.4.3.15(b) respectively. The first and second shells of the diamond cubic structure of Ge labelled as Ge$_1$-Ge$_2$ and Ge$_1$-Ge$_3$ respectively in Figure 3.4.3.15(b) fit well with the FT modulus of Ca$_1$-H$_2$Ar600°C (see Figure 3.4.3.16 and Table 3.4.3.3). This is consistent with the XRD data of Ca$_1$-H$_2$Ar600°C shown in Figure 3.4.3.14.

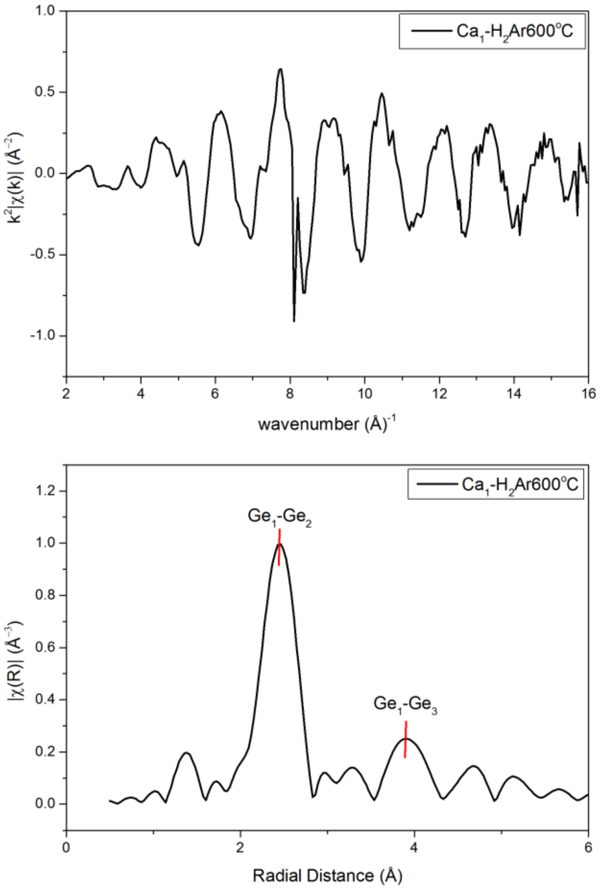

**Figure 3.4.3.15** EXAFS of Ge qdots ($Ca_1$-$H_2$Ar600°C) at Ge K-edge (a) in *k*-space and (b) the FT modulus of EXAFS in *r*-space.

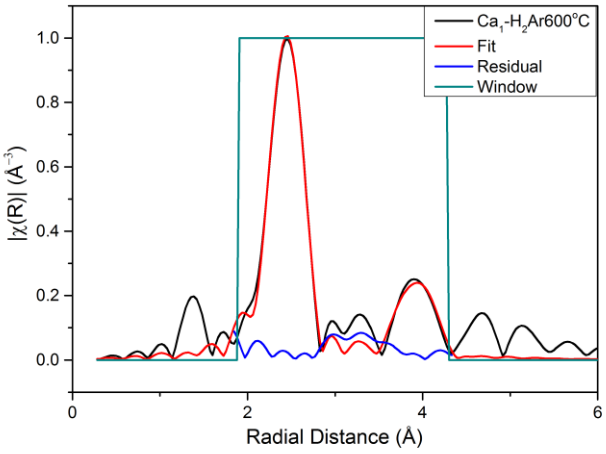

**Figure 3.4.3.16** The FT modulus of EXAFS of $Ca_1$-$H_2$Ar600°C, the fit, the residual between the fit and the data and the window of the fit. The diamond cubic structure of Ge is used for the fit.

**Table 3.4.3.3** The R-factor and interatomic distances extracted from the multiple shell fit of the FT modulus of EXAFS of Ge nanoparticles formed using $Ca_1$- $H_2$Ar600 °C. The interatomic distances are in Å.

| **The fitting quality and parameters** | **$Ca_1$-$H_2$Ar600 °C EXAFS** |
|---|---|
| R-factor | 0.015 |
| $R_{i1}$ ($Ge_1$-$Ge_2$) | 2.461 ± 0.005 |
| $R_{i2}$ ($Ge_1$-$Ge_3$) | 3.993 ± 0.022 |

## Summary of the Results

The results for $Ca_1$ sample can be summarised as follows:

- Size of Ge nanoparticles was found to be 0.98 nm by XRD, 4.2 ± 1.7 nm by TEM and 2.7 ± 0.3 nm by Raman.
- PL spectroscopy shows emission peaks approximately at 661 nm (1.81 eV) and 810 nm (1.53 eV).
- XRD shows alpha-quartz type $GeO_2$ in addition to disordered Ge sites with the diamond cubic like structure.
- EXAFS confirms the disordered diamond cubic-like structure of Ge represented by one shell and alpha-quartz type $GeO_2$.

As seen in the case of $CS_1$ (see page 63), the peak of PL emission at around 810 nm (1.53 eV) of $Ca_1$ is also consistent with the theoretical models (tight binding model and k.p perturbation theory) for matrix-free nanoparticles of around 3 nm in size (Figure 1.2.1.5).

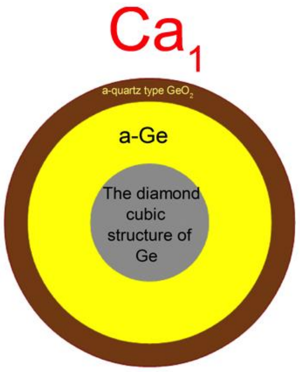

**Figure 3.4.3.17** Schematic representation of as-prepared Ge qdots formed using $Ca_1$ in sub-nano scale showing Ge nanocrystals (the diamond cubic structure of Ge) surrounded with disordered Ge qdots and an oxide surface shell.

XRD results show a significant degree of structural disorder in $Ca_1$ in addition to the signature of alpha-quartz type $GeO_2$. This result was also confirmed by the EXAFS data of $Ca_1$. Based on the analysis carried out for $CS_1$ sample and taking into account presence of the oxide in the EXAFS data of as-prepared $Ca_1$ samples we feel that the core-shell model can be appropriate in this case to explain all the data. However, in case of $Ca_1$ samples the model is different and includes a crystalline core of the diamond cubic structure of Ge, an amorphous outer shell and an O-terminated surface (see Figure 3.4.3.17).

# CHAPTER 4. CONCLUSION

A variety of advanced techniques of synthesis of Ge qdots have been examined. Ge nanoparticles were synthesised using physical and chemical methods, including stain etching, laser ablation, the sol-gel method and two colloidal synthesis techniques ($CS_1$ and $Ca_1$). All of the methods resulted in the formation of Ge nanoparticles. Nevertheless, different light emissions from these samples were detected, and systematic characterisation of Ge nanoparticles with complementary techniques including X-ray absorption spectroscopy and X-ray diffraction was used to understand the structural properties of Ge nanoparticles and to shed light onto the origins of the light emission.

A summary of the findings for as-prepared Ge nanoparticles produced by each method can be given as follows.

H-terminated Ge nanoparticles are formed using chemical stain etching contain disordered Ge structure that is mainly responsible for the light emission at about 700 nm.

Ge nanoparticles formed by the laser ablation mainly have the diamond cubic structure; nevertheless, the light emission with peaks at 605 nm (2.06 eV) and 700 nm (1.77 eV) was found to be due to the alpha-quartz type $GeO_2$ most likely located on the surface of the particles.

Ge nanoparticles embedded in silica were found to be in the form of Ge nanocrystals with alpha-quartz and rutile type $GeO_2$ also present. The light emission at 600 nm (2.05 eV) and 675 nm (1.84 eV) was found to be due to the rutile-like $GeO_2$ most likely located at the surface of nanoparticles.

Colloidally prepared $CS_1$ Ge nanoparticles (formed using $GeCl_4$ as a precursor) were found to be best described by the core/shell model with a crystalline core of the ST-12 phase surrounded by an amorphous Ge layer and H-terminated surface. We have not been able to determine the origins of the light emission.

Colloidally prepared $Ca_1$ Ge nanoparticles (formed using $GeO_2$ as a precursor) were found to be best described by a core-shell model. However, the core, the intermediate region and the surface are likely to consist of crystalline diamond structure of Ge, an amorphous Ge and O-terminated surface respectively.

The colloidal synthesis using $GeCl_4$ ($CS_1$-$H_2$) was shown to result in Ge qdots with an oxide-free surface terminated by hydrogen. Furthermore, we also showed that by using annealing, we can control surface termination in $Ca_1$ samples (reducing the amount of oxide significantly), change particle size, and possibly produce metastable phases.

Out of all the methods considered in this work, colloidal synthesis using benchtop chemistry with $GeCl_4$ as precursor ($CS_1$ samples) is thought to be the most effective and promising synthesis route in terms of stability of the as-prepared Ge qdots and its luminescence, with almost no oxides present.

## 4.1. Outstanding Questions and Future Work

From the point of view of understanding of fundamental origins of the light emission and of applications of Ge qdots there are some important questions that need to be addressed, concerning particle stability (especially against oxidation), optical band gap control and the level of PL quantum yield.

As far as particle stability against oxidation is concerned, $GeCl_4$ based colloidal synthesis is the most promising route, as it seems to yield hydrogen-terminated qdots. Hydrogen termination is usually a starting point for subsequent surface stabilisation and functionalization (Wang, Chang, Liu, & Dai, 2005). In that respect we see the future in adjusting the synthesis to accommodate for surface termination with alkyls, thiols, etc. Here it would be also important to understand the microscopic mechanisms of the nucleation and growth of Ge qdots formed using colloidal synthesis. Understanding these mechanisms in situ can be achieved using synchrotron-based techniques such as a combination of XRD, Raman and quick-EXAFS (Li *et al.*, 2010).

Controlling the optical band gap for the purpose of light emission applications implies an ability to control the particle size of Ge during the synthesis. This would also require in-depth understanding of nucleation and growth of Ge qdots. Specifically, an ability to prepare Ge qdots by colloidal synthesis in the size range of 1.5- 4 nm to cover UV-IR range would be desirable.

Comprehensive work is required to link synthesis conditions (including surface termination) with the PL quantum yield in order to optimise the light emitting properties of Ge qdots. Despite the potential of Ge qdots revealed in this study, including stability and light emission, there are various aspects that can help to further improve their properties, such as quantum yield and stability of Ge qdots in air or water. Water solubility of Ge qdots is found to be useful in biological studies (Lambert *et al.*, 2007; Prabakar *et al.*, 2010), however, in order to keep long-term stability of as-prepared samples, modifications such as surface coating are necessary. This process can generally be applied to CdSe based qdots (Marcel *et al.*, 1998) not only to produce a sample with lower toxicity but also to increase its quantum yield such as more than 50 %.

# APPENDIX

## The Background Subtraction and Normalisation of EXAFS Measurements Using ATHENA

All the EXAFS raw data were processed using the program ATHENA[26]. ATHENA was used to import the raw data and convert it to $\mu(E)$, normalise the data and subtract the background from the data to obtain $\chi(k)$.

The first measurement was taken for bulk Ge as a reference at Ge K-edge between 11 keV-12 keV, and the background removal process of the EXAFS of the bulk Ge was performed as follows. The background function in ATHENA is created using three parameters: rbgk factor, spline range in k (or E) and spline clamps[27] (see Figure A-1 for the parameters shown inside the white oval shapes). Nevertheless, the main parameter that determines the background is the rbgk factor, which enables to minimise the unphysical low part in *r*-space. The effect of the change of the rbgk value (between 1.0 Å to 1.8 Å) on the FT modulus of EXAFS of bulk Ge is shown to be in Figure A-3. As we know there is no bond distance below 2.0 Å in crystalline bulk Ge and, it will be acceptable to set it at 1.8 Å in this case. In other words, the value of rbgk balances between the background and the data, and if it is set too high there may cause to remove information from the measurement.

Normalisation is also an important process to enable direct comparison of the data with the theory. In other words, normalisation is the process of removing variations due to sample preparation, thickness and other aspects of the

---

[26] ATHENA is a program available after installation of DEMETER (Newville, 2001; Ravel & Newville, 2005).

[27] The user guide followed is available in reference (Bruce Ravel, 2009).

measurement. Normalisation in ATHENA is done based on a process called edge step normalisation, which can be controlled by using four parameters: “*E0*”, “edge step”, “pre-edge range”, and “normalisation range” (see Figure A-1 for the parameters shown inside the black rectangular shapes). The pre-edge range and the normalisation range were adjusted using a linear and a quadratic polynomial (usually with a degree of three) regressed to the data respectively.

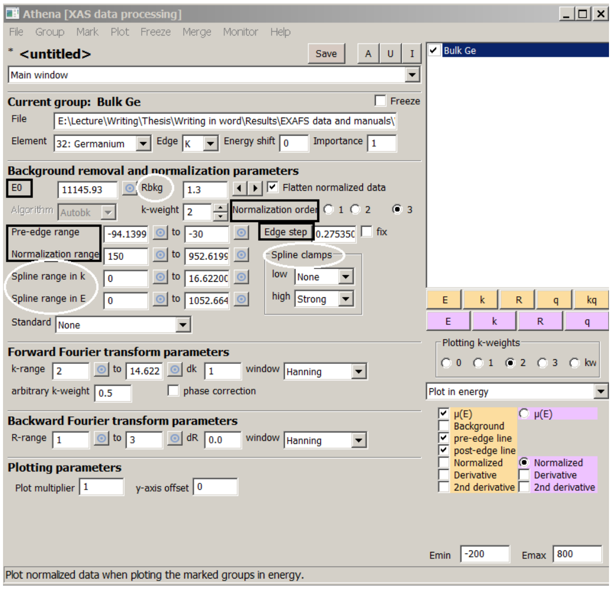

**Current group: Bulk Ge**

☐ Freeze

File: E:\Lecture\Writing\Thesis\Writing in word\Results\EXAFS data and manuals\

Element: 32: Germanium  Edge: K  Energy shift: 0  Importance: 1

**Background removal and normalization parameters**

E0: 11145.93  Rbkg: 1.3  ☑ Flatten normalized data

Algorithm: Autobk  k-weight: 2  Normalization order: ○ 1 ○ 2 ● 3

Pre-edge range: -94.1399 to -30  Edge step: 0.275350  ☐ fix

Normalization range: 150 to 952.6199

Spline range in k: 0 to 16.62200

Spline range in E: 0 to 1052.664

Spline clamps: low: None  high: Strong

Standard: None

**Forward Fourier transform parameters**

k-range: 2 to 14.622  dk: 1  window: Hanning

arbitrary k-weight: 0.5  ☐ phase correction

**Backward Fourier transform parameters**

R-range: 1 to 3  dR: 0.0  window: Hanning

**Plotting parameters**

Plot multiplier: 1  y-axis offset: 0

☑ Bulk Ge

Plotting k-weights: ○ 0 ○ 1 ● 2 ○ 3 ○ kw

Plot in energy

☑ μ(E)  ○ μ(E)
☐ Background
☑ pre-edge line
☑ post-edge line
☐ Normalized  ● Normalized
☐ Derivative  ☐ Derivative
☐ 2nd derivative  ☐ 2nd derivative

Emin: -200  Emax: 800

Plot normalized data when ploting the marked groups in energy.

**Figure A-1** Selecting the background removal and the normalising parameters in ATHENA.

As shown in Figure A-2, before and after normalisation, these parameters were found to be working fine with the reference bulk Ge.

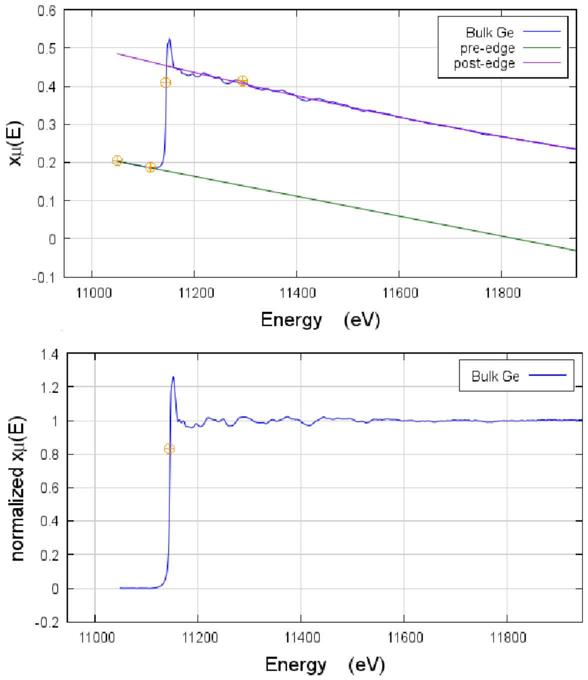

**Figure A-2** (Top) Bulk Ge *μ(E)* at Ge K-edge with pre- and post-edge lines. (Bottom) Normalised *μ(E)* for Bulk Ge,

The background is removed and the normalised EXAFS data are ready to be imported to another package used for the fitting processes -ARTEMIS[28].

---

[28] ARTEMIS is also available after installation of DEMETER (Newville, 2001; Ravel & Newville, 2005).

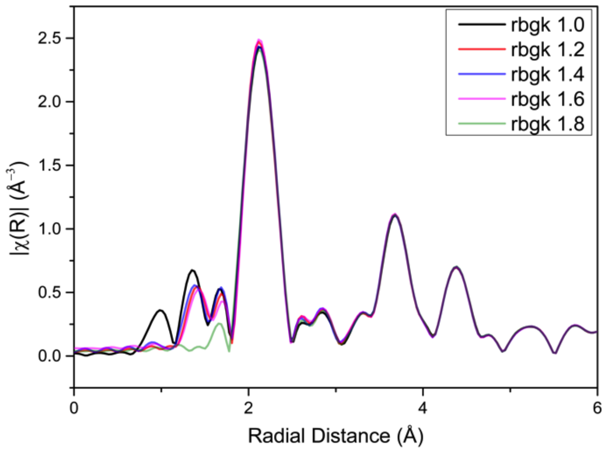

**Figure A-3** The FT modulus of EXAFS of bulk Ge with the rbgk values from 1.0 to 1.8 Å.

## Fitting of EXAFS Measurements Using ARTEMIS

As the data process in ATHENA is already finished, the next steps followed are[29]: (i) choosing the structural reference model; (ii) generating scattering paths based on the model; (iii) choosing the relevant structural parameters to be fitted and finally (iv) completion of the fitting by refining the parameters. The scattering paths as shown in Figure A-4 were generated based on diamond cubic crystalline Ge [30] using the window called "Atoms and Feff" within ARTEMIS.

---

[29] A couple of guides for the EXAFS data analysis presented by Shelly D. Kelly and Bruce Ravel can be followed using references (Shell D. Kelly, 2004) and (Bruce Ravel, 2010).

[30] The file is in .inp format and available in (Newville, n.d.).

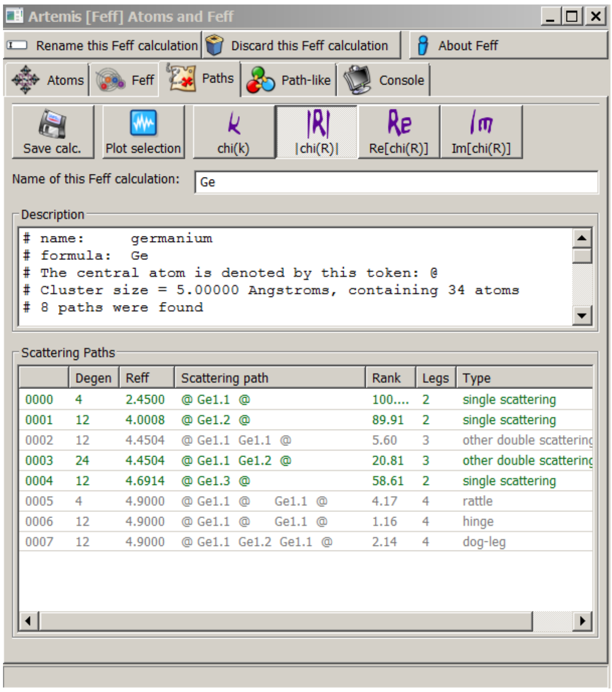

Name of this Feff calculation: Ge

Description

```
# name:     germanium
# formula:  Ge
# The central atom is denoted by this token: @
# Cluster size = 5.00000 Angstroms, containing 34 atoms
# 8 paths were found
```

Scattering Paths

|  | Degen | Reff | Scattering path | Rank | Legs | Type |
|---|---|---|---|---|---|---|
| 0000 | 4 | 2.4500 | @ Ge1.1 @ | 100.... | 2 | single scattering |
| 0001 | 12 | 4.0008 | @ Ge1.2 @ | 89.91 | 2 | single scattering |
| 0002 | 12 | 4.4504 | @ Ge1.1 Ge1.1 @ | 5.60 | 3 | other double scatterin |
| 0003 | 24 | 4.4504 | @ Ge1.1 Ge1.2 @ | 20.81 | 3 | other double scatterin |
| 0004 | 12 | 4.6914 | @ Ge1.3 @ | 58.61 | 2 | single scattering |
| 0005 | 4 | 4.9000 | @ Ge1.1 @ Ge1.1 @ | 4.17 | 4 | rattle |
| 0006 | 12 | 4.9000 | @ Ge1.1 @ Ge1.1 @ | 1.16 | 4 | hinge |
| 0007 | 12 | 4.9000 | @ Ge1.1 Ge1.2 Ge1.1 @ | 2.14 | 4 | dog-leg |

**Figure A-4** The scattering paths were formed using the "Atoms and Feff" window inside ARTEMIS. Inside this window, each scattering path is ready to be inserted to the "Data" window in ARTEMIS. This window is very useful since the contributions from each scattering path can be plotted as chi($k$), chi($R$), Re[chi($R$)] and Im[chi($R$)] to compare with the EXAFS measurement without performing the fit.

It is useful to mention some of the fitting parameters (see page 37), which will be used either as variables or will be set to a value before the fitting is performed. These parameters are $N_i$ for the number of neighbors, $S_0^2$ for scattering amplitude attenuation, $\Delta R$ [31] for the absorber-scatterer distance, $\sigma^2$ for the RMSD value which stands for the vibration of the atoms and contributes to the Debye-Waller factor. These parameters, as shown in Figure A-5, were defined in the "Data" window in ARTEMIS. Additionally, there is a parameter for the energy shift

---

[31] $R_i$ is determined using the sum of the initial path length ($\mathrm{R_{eff}}$) and change in the half-path length $\Delta R$.

named $\Delta E0$ [32] shown in the parameter entry side in the Data window in Figure A-5.

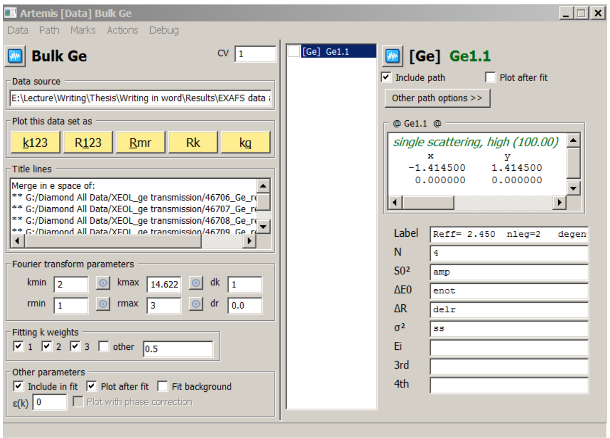

**Bulk Ge**

CV: 1

Data source: E:\Lecture\Writing\Thesis\Writing in word\Results\EXAFS data

Title lines:

```
Merge in e space of:
** G:/Diamond All Data/XEOL_ge transmission/46706_Ge_re
** G:/Diamond All Data/XEOL_ge transmission/46707_Ge_re
** G:/Diamond All Data/XEOL_ge transmission/46708_Ge_re
** G:/Diamond All Data/XEOL_ge transmission/46709_Ge_re
```

Fourier transform parameters: kmin 2, kmax 14.622, dk 1, rmin 1, rmax 3, dr 0.0

Fitting k weights: ☑ 1 ☑ 2 ☑ 3 ☐ other 0.5

Other parameters: ☑ Include in fit ☑ Plot after fit ☐ Fit background

ε(k) 0 ☐ Plot with phase correction

**[Ge] Ge1.1**

☑ Include path ☐ Plot after fit

@ Ge1.1 @

```
single scattering, high (100.00)
        x           y
  -1.414500    1.414500
   0.000000    0.000000
```

Label: Reff= 2.450 nleg=2 degen

N: 4

S0²: amp

ΔE0: enot

ΔR: delr

σ²: ss

Ei:

3rd:

4th:

**Figure A-5** The Data window in ARTEMIS used to include the scattering paths and their relevant parameters. As given in the bottom right hand side of the figure, the parameters $N_i$, $S_0^2$, $\Delta E_0$, $R_i$ are obtained using $N$, $S0^2$, $\Delta E0$, $\Delta R$ respectively.

As the sample is crystalline bulk Ge, we know it has 4 nearest neighbours, hence it is set to 4. Other parameters, $S0^2$, $\Delta E0$, $\Delta R$ and $\sigma^2$ were named as amp, enot, delr, and ss respectively in the Data window. Then, the parameters can be set in another window called "GDS" (Guess, Define, and Set). As shown in Figure A-6, the parameters were chosen in the GDS window as guess parameters and their values were entered using the reference (Ridgway *et al.*, 2004) values for c-Ge in the first instance.

---

[32] The formula for the energy shift, $\Delta E0$ can be given as $k^2=2\, m_e(E-\Delta E0)/\hbar^2$.

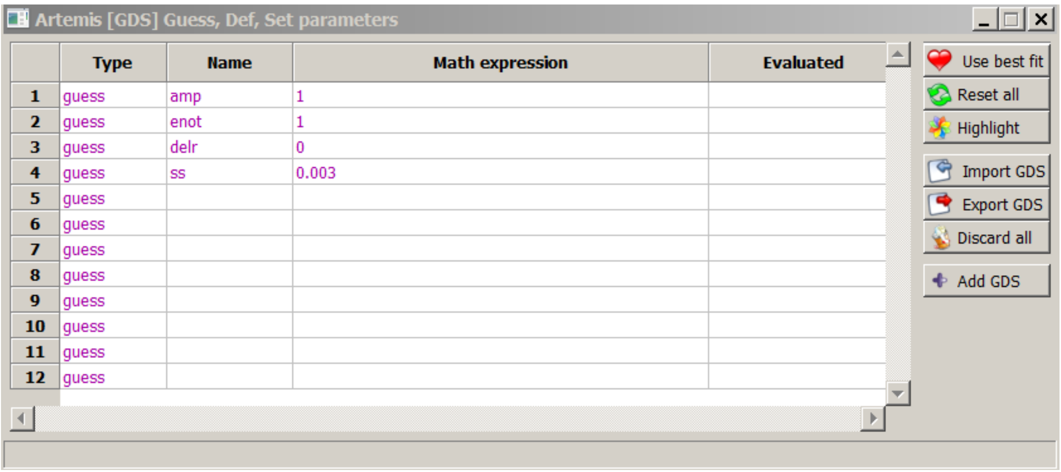

|  | Type | Name | Math expression | Evaluated |
|---|---|---|---|---|
| 1 | guess | amp | 1 |  |
| 2 | guess | enot | 1 |  |
| 3 | guess | delr | 0 |  |
| 4 | guess | ss | 0.003 |  |
| 5 | guess |  |  |  |
| 6 | guess |  |  |  |
| 7 | guess |  |  |  |
| 8 | guess |  |  |  |
| 9 | guess |  |  |  |
| 10 | guess |  |  |  |
| 11 | guess |  |  |  |
| 12 | guess |  |  |  |

**Figure A-6** The GDS window in ARTEMIS used to insert the parameters as guess parameters; nevertheless they can also be set to a value or a defined function in this window.

Before performing the fitting process in *r*-space, the data can be plotted in the "Plot" window in ARTEMIS, as represented in Figure A-7, in order to see the range of the fitting window.

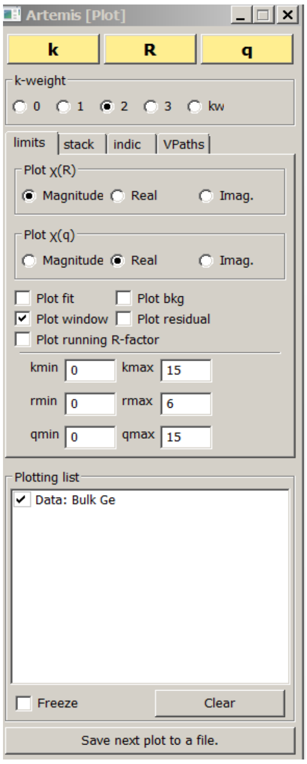

k-weight
○ 0 ○ 1 ● 2 ○ 3 ○ kw

Plot χ(R)
● Magnitude ○ Real ○ Imag.

Plot χ(q)
○ Magnitude ● Real ○ Imag.

☐ Plot fit ☐ Plot bkg
☑ Plot window ☐ Plot residual
☐ Plot running R-factor

kmin 0 kmax 15
rmin 0 rmax 6
qmin 0 qmax 15

Plotting list
☑ Data: Bulk Ge

☐ Freeze

**Figure A-7** The Plot window in ARTEMIS which gives control over plotting before and after a fitting process.

Figure A-8 was obtained by clicking the R button (in yellow) in the Plot window. In Figure A-8, the fitting window is shown to be set between 1-3 Å. Nevertheless, only for the first shell fit of Fourier transform (FT) modulus of the EXAFS of the reference bulk Ge, the window range was changed to between 1.5-2.8 Å, as shown in Figure A-9.

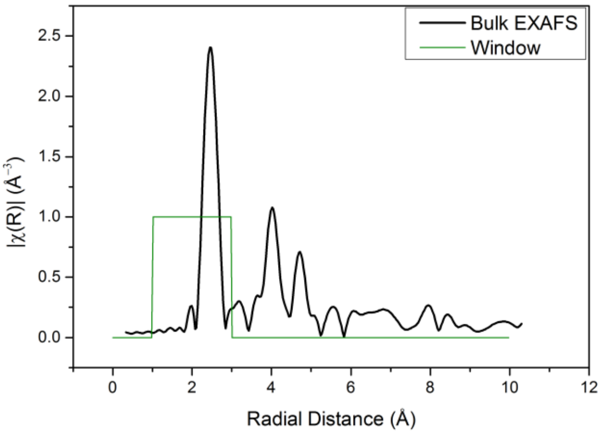

**Figure A-8** The Fourier transform modulus of EXAFS of Bulk Ge in *r*-space (blue colour) is shown with the fitting window (olive colour) between 1.0-3.0 Å. The data is shown as phase-shifted.

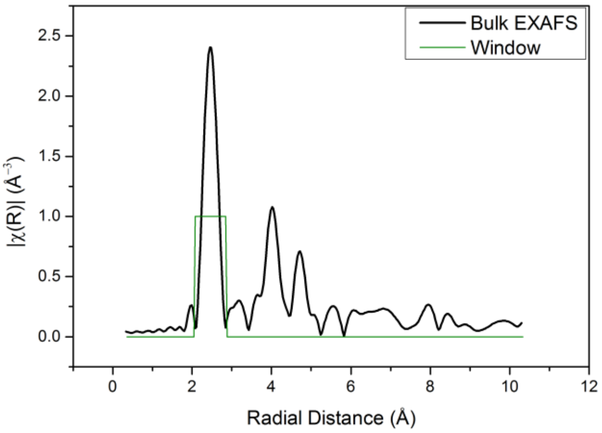

**Figure A-9** The Fourier transform modulus of EXAFS of Bulk Ge in *r*-space (black colour) is shown with the fitting window (olive colour) between 1.7-2.5 Å. The data and the window was shown as phase-shifted, thus, it is represented between 2.0-2.8 Å.

After this process, the fitting process for the first shell fit was launched by clicking the fit button in the "EXAFS data analysis" window shown in Figure A-

10, and the log file was obtained, which gives the values of each parameter entered as variable in the Data window in Figure A-5.

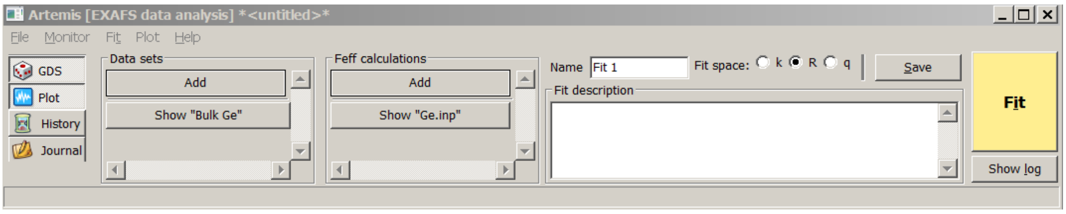

Name: Fit 1

Fit space: ○ k ● R ○ q

**Figure A-10** The EXAFS data analysis window which is main control window in ARTEMIS.

The first shell fit of the FT modulus of EXAFS of bulk Ge was obtained and shown in Figure A-11. By clicking the Show log button under the Fit button in the EXAFS data analysis window, the fitting parameters can be obtained after completing the fit, thus the quality of the fitting can be evaluated.

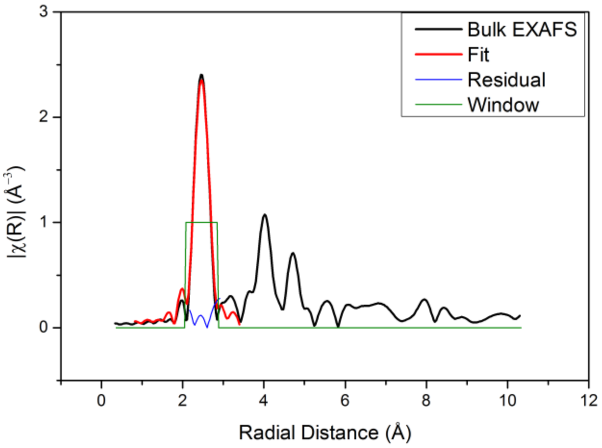

**Figure A-11** The Fourier transform modulus of EXAFS of Bulk Ge (black colour), the first shell fit (red colour) and the fitting window range (olive colour) are represented in *r*-space. Additionally, the residual (blue colour) between the fit and the measurement can be demonstrated.

**Table A-1** The fit quality and the parameters after completing the first shell fit of the FT of EXAFS of bulk Ge.

| **The fitting quality and parameters** | **Bulk Ge** |
|---|---|
| R-factor | 0.0150 |
| N | 4 |
| $S_0^2$ | 0.903 ± 0.096 |
| $\Delta E_0$ (eV) | 3.763 ± 1.378 |
| $\sigma^2$ ($Å^2$) | 0.0023 ± 0.0005 |
| $\Delta R$ (Å) | -0.0023 ± 0.005 |
| $R_i=R_{eff}$[33] + $\Delta R$ (Å) | 2.45-0.002± 0.005<br>≈2.4475± 0.005 |

There are two values inside the log file in order to understand the quality of the fit (Penner-Hahn, 2003). One of them is a reduced chi-squared statistic, $\xi^2$ as shown in Equation A-1.

$$\xi^2 = \frac{(N_{ind}/\nu)\cdot\sum_{i=1}^{N}(\chi_{obs}(k_i)-\chi_{cal}(k_i))^2/\varepsilon_i^2}{N} \qquad \text{Equation A-1}$$

where the sum is calculated over all the measured data points, $N$ and the deviation is weighted by a factor of $1/\varepsilon_i^2$ where $\varepsilon_i^2$ is the root-mean square uncertainty in $\chi_{obs}$. In Equation A-1, $\upsilon$ is number of the degrees of the freedom calculated from $\upsilon=N_{ind}-N_{var}$.

$N_{ind}$ is the well-known Nyquist criteria as given in Equation A-2 which limits the number of variables in the case of the fitting process. $N_{var}$ is the number of variables that are inserted to perform the fitting process.

---

[33] $R_{eff}$ is the theoretically calculated interatomic distance and found in the output log file next to $R_i$.

$$N_{ind} = \frac{2\Delta k \Delta R}{\pi} \qquad \text{Equation A-2}$$

In most cases of the EXAFS measurements, $k_{min}$ is 2 Å$^{-1}$ and $k_{max}$ is often 14 Å$^{-1}$ or less. $R$ range is usually between 1-4 Å, hence $N_{ind}$ can be approximately 20 with the possibility of being larger in some cases.

The second criterion used to understand the quality of the fit is the R-factor, which is the percentage of the misfit between the measured EXAFS signal and the fit. In most cases, it may not be possible to see straightaway the quality of the fit by looking at the reduced chi-squared value, and in such cases the R-factor value can be helpful.

Another important criterion to keep in mind is the correlation between the variables. Correlation shows the range, which can change from -1 to 1 and indicates in which direction and how much a parameter can change, without statistically changing the fit when changing another parameter (Tromp, 2007). $S_0^2$ is correlated to $\sigma^2$ and $\Delta E_0$ is correlated with $\Delta R$. Since $\Delta E_0$ was obtained as 3.763 ± 1.378 at the end of the first shell fit, the error, ± 1.378 in $\Delta E_0$ may be considered large and, in such cases, $\Delta E_0$ can be set to 0 (Kelly, 2004). On the other hand, $\Delta E_0$ can be negative so, in some cases, the error for $\Delta E_0$ obtained can be larger and is considered to be acceptable (Ravel, 2010).

Furthermore, in multiple shell fitting, the amplitude reduction factor ($S_0^2$) and the energy shift ($\Delta E_0$) are usually believed to be the same for each path of the same element (Ridgway *et al.*, 2004). Therefore, the procedure given in the first shell fitting was followed in a similar manner and only the $\sigma^2$ and $\Delta R$ were written differently as guess parameters for each path.

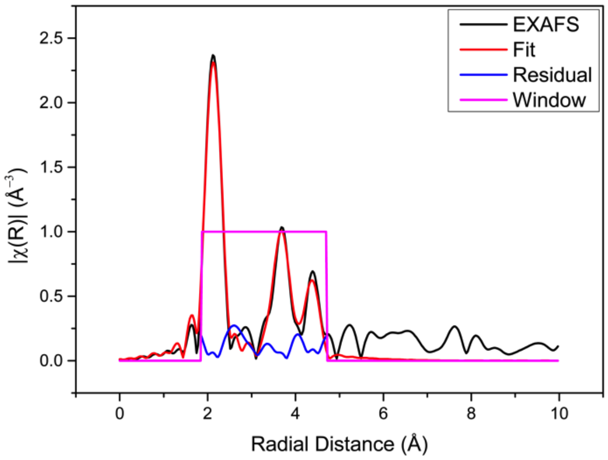

**Figure A- 12** The multiple shells fit (red colour) of the Fourier transform modulus of EXAFS of Bulk Ge (black colour), the fitting window range (magenta colour) and the residual (blue colour) between the data and the fit are represented in *r*-space.

**Table A- 2** The R-factor and interatomic distances extracted from the multiple shell fit of EXAFS of bulk Ge.

| **The fitting quality and parameters**[34] | **Bulk Ge Fit** | **Bulk Ge Model** |
|---|---|---|
| R-factor | 0.016 | - |
| $R_{i1}$ (Å) | 2.442 ± 0.002 | 2.449 |
| $R_{i2}$ (Å) | 3.990 ± 0.004 | 3.999 |
| $R_{i3}$ (Å) | 4.674 ± 0.006 | 4.691 |

Nevertheless, if we set all the parameters for the each shell of the fit of the bulk Ge as different from one another[35], and the parameters, the $\sigma^2$ and $\Delta R$ at the

---

[34] $R_{i1}$ is the first interatomic distance and was named Ge1.1. $R_{i2}$ was the secondary shell and named Ge1.2 and the third shell, $R_{i3}$ was named Ge1.3.

[35] The *R* and the *k* fit range was also changed to 1.75-4.65 Å and 3.1-13.6 Å$^{-1}$ respectively for the multiple shell fitting. Since there are 18.98 independent parameters (the calculation was based on Nyquist criteria), $S_0^2$, $\Delta E_0$, $\Delta R$ and $\sigma^2$ are considered to be different for all the shells in Ge. For the secondary shell, the number of nearest neighbour, *N* was set to 12 and the other parameters, $S_0^2$, $\Delta E_0$,

end of the fit of EXAFS of bulk Ge, was not changed and the fit is shown in Figure A-13.

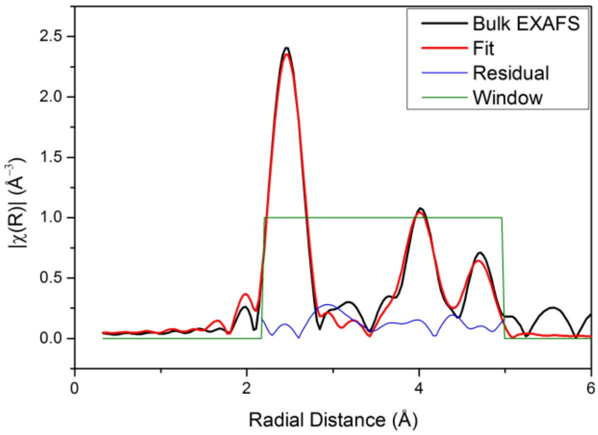

**Figure A-13** The multiple shell fit (red colour) of the Fourier transform modulus of EXAFS of Bulk Ge (blue colour), and the fitting window range (olive colour) are represented in *r*-space.

In this project, the main aim of using EXAFS was to determine the local structure around the central Ge atom. Hence, instead of giving all the parameters in Table A-1, reporting the interatomic distances between the central atom and its neighbours, as shown in Table 3, was considered to be adequate.

**Table A-3** The R-factor and interatomic distances extracted from the multiple shell fit of EXAFS of bulk Ge.

| The fitting quality and parameters | Bulk Ge Fit | Bulk Ge Model |
|---|---|---|
| R-factor | 0.016 | - |
| $R_{i1}$ (Å) | 2.446 ± 0.003 | 2.449 |
| $R_{i2}$ (Å) | 3.989 ± 0.005 | 3.999 |
| $R_{i3}$ (Å) | 4.696 ± 0.007 | 4.691 |

---

$\Delta R$ and $\sigma^2$ were used as a guess parameter with values of 1, 0.0, 0 and 0.003 in the first instance, based on the calculation of FEFF6 code for crystalline bulk Ge.

As shown in Table A-3, the interatomic distances of the bulk Ge was compared with those of bulk Ge data obtained using ICSD-43422 and found to be consistent within the range of experimental error.

It is also possible to get the fit with the contributions from the individual contribution of each interatomic distance (see Figure A-14).

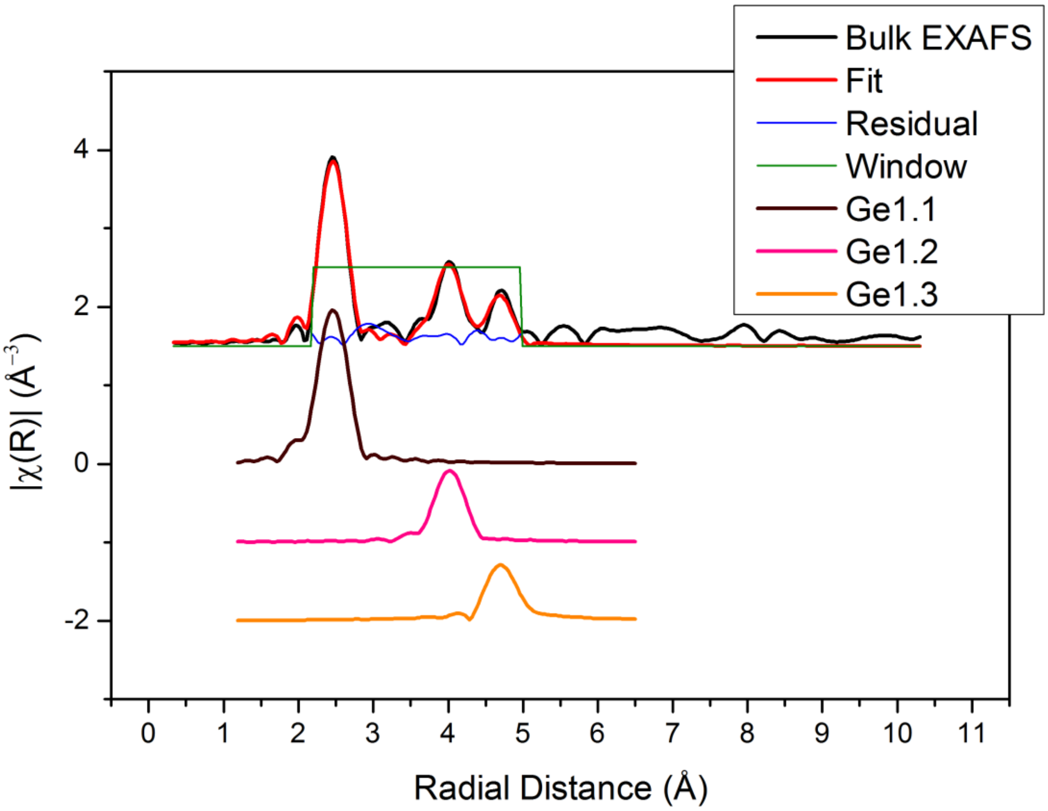

**Figure A-14** The multiple shell fit (red colour) of the Fourier transform modulus of EXAFS of Bulk Ge (black colour), and the fitting window range (olive colour) are represented in *r*-space. The first shell (Ge1.1, brown colour), the second shell (Ge1.2, pink colour) and the third shell (Ge1.3, orange colour) are represented separately in order to demonstrate how each scattering path contributed to the fit.

The results of the EXAFS fit of each sample can be seen in the corresponding part of each sample in RESULTS AND DISCUSSIONS. For the samples which are considered to be oxidised, the scattering paths formed using rutile type $GeO_2$ structure[36] or formed using alpha-quartz type $GeO_2$[37] were fitted with a similar [38] procedure to that applied above for the fit of the FT modulus of EXAFS of bulk Ge in *r*-space.

## Tables of Fitted Parameters

The tables of the fit parameters for all of the samples can be found in this section, one after another as followed in the thesis. The models used in order to perform the fit of the FT modulus of EXAFS of the samples were separated according to the appointed colour for each model. The shells for the diamond structure are shown in light blue e.g. $Ge_1$-$Ge_2$. The shells of the alpha-quartz type are shown in red e.g. $Ge_1$-$O_1$. The shells of the rutile type $GeO_2$ are represented in black e.g. $Ge_1$-$O_1$. In the same way, the shells of the ST-12 phase are shown in green e.g. $Ge_1$-$Ge_2$.

---

[36] See (Newville, 2001) to get the .inp file for rutile type $GeO_2$.

[37] FEFF code formed using COD ID: 9007477 database card for alpha-quartz type $GeO_2$ via FEFF window inside ARTEMIS.

[38] The rbgk value for the background removal was set as 1.0 since larger values may offer the possibility of removing or adding information to the data. The appropriate $GeO_2$ model was used based on the data. Other process were followed in the same manner of the EXAFS analysis of bulk Ge.

## EXAFS of Bulk Ge (Diamond)

The amplitude reduction factor and the energy shifts in the fit of the FT modulus of EXAFS of bulk Ge were used as guess parameters and set to the same values for each scattering path.

**Table A- 4** The fit quality and the parameters after completing the multiple shell fit of the FT of EXAFS of bulk Ge

| **The fitting quality and parameters** | **Bulk Ge** |
|---|---|
| R-factor | 0.023 |
| N (Ge$_1$-Ge$_2$) (set) | 4 |
| $S_0^2$ | 0.843 ± 0.054 |
| $\Delta E_0$ (eV) | 2.095 ± 0.619 |
| $\sigma^2$ (Å$^2$) | 0.0020 ± 0.0003 |
| $\Delta R$ (Å) | -0.007 ± 0.002 |
| N (Ge$_1$-Ge$_3$) (set) | 12 |
| $S_0^2$ | 0.843 ± 0.054 |
| $\Delta E_0$ (eV) | 2.095 ± 0.619 |
| $\sigma^2$ (Å$^2$) | 0.0035 ± 0.0004 |
| $\Delta R$ (Å) | -0.010 ± 0.005 |
| N (Ge$_1$-Ge$_4$) (set) | 12 |
| $S_0^2$ | 0.843 ± 0.054 |
| $\Delta E_0$ (eV) | 2.095 ± 0.619 |
| $\sigma^2$ (Å$^2$) | 0.0038 ± 0.0005 |
| $\Delta R$ (Å) | -0.016 ± 0.006 |

## OD-EXAFS of Bulk Ge (Alpha-quartz type $GeO_2$)

The amplitude reduction factor and the energy shifts in the fit of the FT modulus of OD-EXAFS of bulk Ge were used as guess parameters and set to the same values for each scattering path.

**Table A- 5** The fit quality and the parameters after completing the multiple shell fit of the FT of OD-EXAFS of bulk Ge.

| **The fitting quality and parameters** | **Bulk Ge** |
|---|---|
| R-factor | 0.022 |
| N ($Ge_1$-$O_1$) (set) | 4 |
| $S_0^2$ | 0.867 ± 0.085 |
| $\Delta E_0$ (eV) | 2.875 ± 1.625 |
| $\sigma^2$ (Å$^2$) | 0.0017 ± 0.0009 |
| $\Delta R$ (Å) | -0.018 ± 0.009 |
| N ($Ge_1$-$Ge_2$) (set) | 4 |
| $S_0^2$ | 0.867 ± 0.085 |
| $\Delta E_0$ (eV) | 2.875 ± 1.625 |
| $\sigma^2$ (Å$^2$) | 0.0025 ± 0.0009 |
| $\Delta R$ (Å) | -0.008 ± 0.010 |

## EXAFS of LP-PLA (Diamond)

The amplitude factor and energy shifts were set to the same values for each path. The amplitude factor used in the fit of EXAFS of LP-PLA was copied from the amplitude factor obtained from the fit of EXAFS of bulk Ge.

**Table A- 6** The fit quality and the parameters after completing the multiple shell fit of the FT of EXAFS of LP-PLA.

| **The fitting quality and parameters** | **LP-PLA** |
|---|---|
| R-factor | 0.028 |
| N (Ge$_1$-Ge$_2$) (set) | 4 |
| $S_0^2$ (set) | 0.843 |
| $\Delta E_0$ (eV) | 3.071 ± 1.157 |
| $\sigma^2$ (Å$^2$) | 0.0036 ± 0.0003 |
| $\Delta R$ (Å) | -0.012 ± 0.005 |
| N (Ge$_1$-Ge$_3$) (set) | 12 |
| $S_0^2$ (set) | 0.843 |
| $\Delta E_0$ (eV) | 3.071 ± 1.157 |
| $\sigma^2$ (Å$^2$) | 0.0054 ± 0.0005 |
| $\Delta R$ (Å) | -0.019 ± 0.008 |
| N (Ge$_1$-Ge$_4$) (set) | 12 |
| $S_0^2$ (set) | 0.843 |
| $\Delta E_0$ (eV) | 3.071 ± 1.157 |
| $\sigma^2$ (Å$^2$) | 0.0065± 0.0005 |
| $\Delta R$ (Å) | 0.023± 0.009 |

## OD-EXAFS of LP-PLA (Alpha-quartz type $GeO_2$) + (Diamond)

The amplitude factors for alpha-quartz type $GeO_2$ and for the diamond cubic structure used in the fit of OD-EXAFS of LP-PLA were copied from the amplitude reduction factor obtained from the fit of OD-EXAFS and EXAFS of bulk Ge respectively.

**Table A- 7** The fit quality and the parameters after completing the multiple shell fit of the FT of OD-EXAFS of LP-PLA.

| **The fitting quality and parameters** | **LP-PLA** |
|---|---|
| R-factor | 0.020 |
| N ($Ge_1$-$O_1$) (set) | 4 |
| $S_0^2$ | 0.868 |
| $\Delta E_0$ (eV) | 4.673 ± 0.959 |
| $\sigma^2$ (Å$^2$) | 0.0021 ± 0.0008 |
| ΔR (Å) | -0.005 ± 0.004 |
| N ($Ge_1$-$Ge_2$) (set) | 2 |
| $S_0^2$ | 0.232 ± 0.037 |
| $\Delta E_0$ (eV) | 22.498 ± 2.047 |
| $\sigma^2$ (Å$^2$) | 0.0061 ± 0.0013 |
| ΔR (Å) | 0.043 ± 0.016 |
| N ($Ge_1$-$Ge_2$) (set) | 4 |
| $S_0^2$ (set) | 0.868 |
| $\Delta E_0$ (eV) | 4.673 ± 0.959 |
| $\sigma^2$ (Å$^2$) | 0.0027 ± 0.0006 |
| ΔR (Å) | -0.008 ± 0.008 |

### EXAFS of the sol-gel method (Alpha-quartz type $GeO_2$) + (Diamond)

The amplitude factors for alpha-quartz type $GeO_2$ and for the diamond cubic structure used in the fit of EXAFS of the sol-gel method were copied from the amplitude reduction factor obtained from the fit of OD-EXAFS and EXAFS of bulk Ge respectively.

**Table A- 8** The fit quality and the parameters after completing the multiple shell fit of the FT of EXAFS of the sol-gel method.

| **The fitting quality and parameters** | **The sol-gel method** |
|---|---|
| R-factor | 0.018 |
| N ($Ge_1$-$O_1$) (set) | 4 |
| $S_0^2$ | 0.868 |
| $\Delta E_0$ (eV) | 3.545 ± 1.468 |
| $\sigma^2$ (Å$^2$) | 0.0015 ± 0.0008 |
| ΔR (Å) | -0.012 ± 0.011 |
| N ($Ge_1$-$Ge_2$) (set) | 4 |
| $S_0^2$ (set) | 0.843 |
| $\Delta E_0$ (eV) | 16.005 ± 0.172 |
| $\sigma^2$ (Å$^2$) | 0.0181 ± 0.0049 |
| ΔR (Å) | 0.028 ± 0.035 |

## OD-EXAFS of the sol-gel method (rutile type $GeO_2$)

The parameters for the fit of OD-EXAFS of the sol-gel method were used as guess parameters while some parameters, such as the amplitude reduction factor, were kept fixed.

**Table A- 9** The fit quality and the parameters after completing the multiple shell fit of the FT of OD-EXAFS of the sol-gel method.

| **The fitting quality and parameters** | **The sol-gel method** |
|---|---|
| R-factor | 0.019 |
| N ($Ge_1$-$O_1$) (set) | 2 |
| $S_0^2$ (set) | 1.150 |
| $\Delta E_0$ (eV) | 7.303 ± 2.081 |
| $\sigma^2$ (Å$^2$) (set) | 0.0022 |
| $\Delta R$ (Å) | -0.117 ± 0.014 |
| N ($Ge_1$-$Ge_2$) (set) | 4 |
| $S_0^2$ | 1.150 |
| $\Delta E_0$ (eV) | 7.303 ± 2.081 |
| $\sigma^2$ (Å$^2$) (set) | 0.0147 |
| $\Delta R$ (Å) | 0.031 ± 0.028 |

## EXAFS of $CS_1$ (Diamond)

The amplitude reduction factor used in the fit of EXAFS of $CS_1$ was copied from the amplitude factor obtained from the fit of EXAFS of bulk Ge.

**Table A- 10** The fit quality and the parameters after completing the single shell fit of the FT of EXAFS of $CS_1$.

| **The fitting quality and parameters** | **$CS_1$** |
|---|---|
| R-factor | 0.029 |
| N ($Ge_1$-$Ge_2$) (set) | 4 |
| $S_0^2$ (set) | 0.843 |
| $\Delta E_0$ (eV) | 2.175 ± 2.427 |
| $\sigma^2$ (Å$^2$) | 0.0062 ± 0.0005 |
| $\Delta R$ (Å) | -0.013 ± 0.012 |

## EXAFS of $CS_1$ (Diamond) + (ST-12 phase)

The amplitude reduction factor used in the fit of EXAFS of $CS_1$ was copied from the amplitude factor obtained from the fit of EXAFS of bulk Ge.

**Table A- 11** The fit quality and the parameters after completing the multiple shell fit of the FT of EXAFS of $CS_1$.

| **The fitting quality and parameters** | **$CS_1$** |
|---|---|
| R-factor | 0.023 |
| N ($Ge_1$-$Ge_1$) (set) | 2 |
| $S_0^2$ (set) | 0.843 |
| $\Delta E_0$ (eV) (set) | 0 |
| $\sigma^2$ (Å$^2$) | 0.0031 ± 0.0007 |
| $\Delta R$ (Å) | -0.018 ± 0.008 |
| N ($Ge_1$-$Ge_2$) (set) | 4 |
| $S_0^2$ | 0.843 |
| $\Delta E_0$ (eV) (set) | 0 |
| $\sigma^2$ (Å$^2$) | 0.0205 ± 0.0055 |
| $\Delta R$ (Å) | -0.083 ± 0.035 |

## EXAFS of $CS_1$-$H_2$ (Diamond)

The amplitude reduction factor used in the fit of EXAFS of $CS_1$ was copied from the amplitude factor obtained from the fit of EXAFS of bulk Ge.

**Table A- 12** The fit quality and the parameters after completing the single shell fit of FT of EXAFS of $CS_1$-$H_2$.

| **The fitting quality and parameters** | **$CS_1$-$H_2$** |
|---|---|
| R-factor | 0.018 |
| N ($Ge_1$-$Ge_2$) (set) | 4 |
| $S_0^2$ | 0.843 |
| $\Delta E_0$ (eV) | 2.814 ± 1.774 |
| $\sigma^2$ (Å$^2$) | 0.0060 ± 0.0004 |
| $\Delta R$ (Å) | -0.011 ± 0.008 |

## EXAFS of $CS_1$-$H_2$ (Diamond) + (ST-12 phase)

The amplitude reduction factor used in the fit of EXAFS of $CS_1$ was copied from the amplitude factor obtained from the fit of EXAFS of bulk Ge.

**Table A- 13** The fit quality and the parameters after completing the multiple shell fit of the FT of EXAFS of $CS_1H_2$.

| **The fitting quality and parameters** | **$CS_1$** |
|---|---|
| R-factor | 0.014 |
| N ($Ge_1$-$Ge_1$) (set) | 2 |
| $S_0^2$ (set) | 0.843 |
| $\Delta E_0$ (eV) (set) | 0 |
| $\sigma^2$ (Å$^2$) | 0.0030 ± 0.0005 |
| $\Delta R$ (Å) | -0.018 ± 0.006 |
| N ($Ge_1$-$Ge_2$) (set) | 4 |
| $S_0^2$ | 0.843 |
| $\Delta E_0$ (eV) (set) | 0 |
| $\sigma^2$ (Å$^2$) | 0.0201 ± 0.0036 |
| $\Delta R$ (Å) | -0.083 ± 0.024 |

## EXAFS of $CS_1$-$H_2Ar$ (Diamond)

The parameters for the fit of FT modulus of EXAFS of $CS_1$-$H_2Ar$ were used as guess parameters while some parameters, such as the amplitude reduction factor, were kept fixed for the each path.

**Table A- 14** The fit quality and the parameters after completing the multiple shell fit of the FT of EXAFS of $CS_1$-$H_2Ar$.

| **The fitting quality and parameters** | **$CS_1$-$H_2Ar$** |
|---|---|
| R-factor | 0.038 |
| N ($Ge_1$-$Ge_2$) (set) | 4 |
| $S_0^2$ (set) | 0.345 |
| $\Delta E_0$ (eV) | 3.108 ± 1.173 |
| $\sigma^2$ (Å$^2$) | 0.0029 ± 0.0003 |
| ΔR (Å) | -0.0003 ± 0.0047 |
| N ($Ge_1$-$Ge_3$) (set) | 12 |
| $S_0^2$ (set) | 0.345 |
| $\Delta E_0$ (eV) | 3.108 ± 1.173 |
| $\sigma^2$ (Å$^2$) | 0.0126 ± 0.004 |
| ΔR (Å) | 0.0040 ± 0.0021 |

## EXAFS of $CS_1$-$H_2Ar$ (Diamond) + (ST-12)

The parameters for the fit of the FT modulus of EXAFS of $CS_1$-$H_2Ar$ were used as guess parameters, and the amplitude reduction factor was copied from the fit of the FT modulus of EXAFS of $CS_1$-$H_2Ar$ (only using the diamond cubic structure) and fixed for each path.

**Table A- 15** The fit quality and the parameters after completing the multiple shell fit of the FT of EXAFS of $CS_1$-$H_2Ar$.

| **The fitting quality and parameters** | **LP-PLA** |
|---|---|
| R-factor | 0.013 |
| N ($Ge_1$-$Ge_2$) (set) | 4 |
| $S_0^2$ (set) | 0.345 |
| $\Delta E_0$ | 3.504 ± 1.215 |
| $\sigma^2$ | 0.0028 ± 0.0002 |
| $\Delta R$ | 0.001 ± 0.004 |
| N ($Ge_1$-$Ge_3$) (set) | 12 |
| $S_0^2$ (set) | 0.345 |
| $\Delta E_0$ (eV) (set) | 0 |
| $\sigma^2$ (Å$^2$) (set) | 0.005 |
| $\Delta R$ (Å) | 0.076 ± 0.040 |
| N ($Ge_1$-$Ge_4$) (set) | 12 |
| $S_0^2$ (set) | 0.345 |
| $\Delta E_0$ (eV) | 3.504 ± 1.215 |
| $\sigma^2$ (Å$^2$) | 0.0118 ± 0.0026 |
| $\Delta R$ (Å) | 0.034 ± 0.022 |

## EXAFS of $Ca_1$ (Diamond) + (a-quartz $GeO_2$)

The parameters for the fit of FT modulus of EXAFS of $CS_1$-$H_2Ar$ were used as guess parameters while the amplitude reduction factor was kept fixed for each path.

**Table A- 16** The fit quality and the parameters after completing the multiple shell fit of the FT of EXAFS of $Ca_1$.

| **The fitting quality and parameters** | **$Ca_1$** |
|---|---|
| R-factor | 0.005 |
| N ($Ge_1$-$O_1$) (set) | 2 |
| $S_0^2$ (set) | 1.128 |
| $\Delta E_0$ (eV) | 5.121 ± 0.880 |
| $\sigma^2$ ($Å^2$) | 0.0050 ± 0.0005 |
| ΔR (Å) | 0.025 ± 0.005 |
| N ($Ge_1$-$Ge_2$) (set) | 4 |
| $S_0^2$ (set) | 0.413 |
| $\Delta E_0$ (eV) | 3.209 ± 1.387 |
| $\sigma^2$ ($Å^2$) | 0.0032 ± 0.0006 |
| ΔR (Å) | 0.0165 ± 0.006 |

## EXAFS of $Ca_1H_2Ar450^oC$ (Diamond) + (a-quartz $GeO_2$)

The parameters for the fit of the FT modulus of EXAFS of $CS_1$-$H_2Ar450^oC$ were used as guess parameters while the amplitude reduction factor was kept fixed for each path.

**Table A- 17** The fit quality and the parameters after completing the multiple shell fit of the FT of EXAFS of $Ca_1$-$H_2$Ar450ºC.

| **The fitting quality and parameters** | **$CS_1$-$H_2$Ar450ºC** |
|---|---|
| R-factor | 0.012 |
| N ($Ge_1$-$O_1$) (set) | 2 |
| $S_0^2$ (set) | 0.225 |
| $\Delta E_0$ (eV) | 8.321 ± 2.592 |
| $\sigma^2$ (Å$^2$) | 0.0022 ± 0.0010 |
| ΔR (Å) | 0.025 ± 0.015 |
| N ($Ge_1$-$Ge_2$) (set) | 4 |
| $S_0^2$ (set) | 0.243 |
| $\Delta E_0$ (eV) | 5.482 ± 1.296 |
| $\sigma^2$ (Å$^2$) | 0.0039 ± 0.0003 |
| ΔR (Å) | 0.011 ± 0.005 |

## EXAFS of $Ca_1$-$H_2$Ar600ºC (Diamond)

The parameters for the fit of the FT modulus of EXAFS of $CS_1$-$H_2$Ar600ºC were used as guess parameters while the amplitude reduction factor was kept fixed for each path.

**Table A- 18** The fit quality and the parameters after completing the multiple shell fit of the FT of EXAFS of $Ca_1$-$H_2$Ar600°C.

| **The fitting quality and parameters** | **$Ca_1$-$H_2$Ar600°C** |
|---|---|
| R-factor | 0.015 |
| N ($Ge_1$-$Ge_2$) (set) | 4 |
| $S_0^2$ | 0.281 |
| $\Delta E_0$ (eV) | 5.986 ± 1.342 |
| $\sigma^2$ (Å$^2$) | 0.0025 ± 0.0004 |
| $\Delta R$ (Å) | 0.011 ± 0.005 |
| N ($Ge_1$-$Ge_3$) (set) | 12 |
| $S_0^2$ | 0.281 |
| $\Delta E_0$ (eV) | 1.356 ± 1.342 |
| $\sigma^2$ (Å$^2$) | 0.0082 ± 0.0028 |
| $\Delta R$ (Å) | -0.008± 0.022 |

# Bibliography

Abramof, P. G., Beloto, A. F., Ueta, A. Y., & Ferreira, N. G. (2006). X-ray investigation of nanostructured stain-etched porous silicon. *Journal of Applied Physics*, **99** (2), 024304. doi:10.1063/1.2162273

Alivisatos, A. P. (1996a). Perspectives on the Physical Chemistry of Semiconductor Nanocrystals. *The Journal of Physical Chemistry*, **100** (31), 13226–13239. doi:10.1021/jp9535506

Alivisatos, A. P. (1996b). Semiconductor Clusters, Nanocrystals, and Quantum Dots. *Science*, **271** , 933–937. doi:10.1126/science.271.5251.933

Alivisatos, A. P., Harris, A. L., Levinos, N. J., Steigerwald, M. L., & Brus, L. E. (1988). Electronic states of semiconductor clusters: Homogeneous and inhomogeneous broadening of the optical spectrum. *The Journal of Chemical Physics*, **89** (7), 4001–4011. doi:10.1063/1.454833

Amendola, V., & Meneghetti, M. (2013). What controls the composition and the structure of nanomaterials generated by laser ablation in liquid solution? *Physical Chemistry Chemical Physics : PCCP*, **15** (9), 3027–46. doi:10.1039/c2cp42895d

Ankudinov, A. L., Rehr, J. J., & Conradson, S. D. (1998). Real-space multiple-scattering calculation and interpretation of X-ray-absorption near-edge structure. *Physical Review B*, **58** (12), 7565–7576. doi:10.1103/PhysRevB.58.7565

Aspenberg, P., Anttila, A., Konttinen, Y. T., Lappalainen, R., Goodman, S. B., Nordsletten, L., & Santavirta, S. (1996). Benign response to particles of diamond and SiC: bone chamber studies of new joint replacement coating materials in rabbits. *Biomaterials*, **17** (8), 807–812. doi:10.1016/0142-9612(96)81418-9

Bar-Lev, A. (1984). *Semiconductors and electronic devices* (p. xii,468 p. : ill ; 23 cm.). Prentice-Hall, c1984 ISBN: 0138252092.

Bostedt, C. (2002). *Electronic Structure of Germanium Nanocrystal Films Probed with Synchrotron Radiation*. PhD Thesis Universitat Hamburg.

Bottani, C. E., Mantini, C., Milani, P., Manfredini, M., Stella, a., Tognini, P., Cheyssac, P., & Kofman, R. (1996). Raman, optical-absorption, and transmission electron microscopy study of size effects in germanium quantum dots. *Applied Physics Letters*, **69** (16), 2409. doi:10.1063/1.117653

Brus, L. (1986). Electronic wave functions in semiconductor clusters: experiment and theory. *The Journal of Physical Chemistry*, **90** (12), 2555–2560. doi:10.1021/j100403a003

Brus, L. E. (1984). Electron–electron and electron-hole interactions in small semiconductor crystallites: The size dependence of the lowest excited electronic state. *The Journal of Chemical Physics*, **80** (9), 4403. doi:10.1063/1.447218

Bulk Ge Band Gap. (2010). Retrieved August 15, 2013, from http://www.ioffe.ru/SVA/NSM/Semicond/Ge/Figs/221.gif

Bulutay, C. (2007). Interband, intraband, and excited-state direct photon absorption of silicon and germanium nanocrystals embedded in a wide band-gap lattice. *Physical Review B*, **76** (20), 205321. doi:10.1103/PhysRevB.76.205321

Bundy, F. P., & Kasper, J. S. (1963). A New Dense Form of Solid Germanium. *Science (New York, N.Y.),* **139** (3552), 340–1. doi:10.1126/science.139.3552.340

Bunker, G. (2010). *A Practical Guide to X-ray Absorption Fine Structure Spectroscopy* (pp. 1–260). Cambridge University Press.

Buriak, J. M. (2002). Organometallic Chemistry on Silicon and Germanium Surfaces. *Chemical Reviews,* **102** (5), 1271–1308. doi:10.1021/cr000064s

Campbell, I. H., & Fauchet, P. M. (1986). The effects of microcrystal size and shape on the one phonon Raman spectra of crystalline semiconductors. *Solid State Communications,* **58** (10), 739–741. doi:10.1016/0038-1098(86)90513-2

Canham, L. T. (1990). Silicon quantum wire array fabrication by electrochemical and chemical dissolution of wafers. *Applied Physics Letters,* **57** (10), 1046. doi:10.1063/1.103561

Choi, H. C., & Buriak, J. M. (2000). Preparation and functionalization of hydride terminated porous germanium. *Chemical Communications*, (17), 1669–1670. doi:10.1039/b004011h

Chou, N. H., Oyler, K. D., Motl, N. E., & Schaak, R. E. (2009). Colloidal Synthesis of Germanium Nanocrystals Using Room-Temperature Benchtop Chemistry. *Chemistry of Materials*, **21** (18), 4105–4107. doi:10.1021/cm902088y

Coppari, F., Di Cicco, a., Congeduti, a., Chervin, J. C., Baudelet, F., & Polian, a. (2009). Amorphous germanium under high-pressure conditions. *High Pressure Research*, **29** (1), 103–107. doi:10.1080/08957950802628190

Crystal Maker. (2013). Retrieved December 21, 2013, from http://www.crystalmaker.com/crystalmaker/index.html

Crystalline Bulk Ge. (2013). Retrieved August 10, 2013, from http://ph.qmul.ac.uk/directory/a.sapelkin

Cullis, A. G., & Canham, L. T. (1991). Visible light emission due to quantum size effects in highly porous crystalline silicon. *Nature*, **353** (6342), 335–338. doi:10.1038/353335a0

Daldosso, N., Luppi, M., Ossicini, S., Degoli, E., Magri, R., Dalba, G., Fornasini, P., Grisenti, R., Rocca, F., Pavesi, L., Boninelli, S., Priolo, F., Spinella, C., & Iacona, F. (2003). Role of the interface region on the optoelectronic properties of silicon nanocrystals embedded in $SiO_2$. *Physical Review B*, **68** (8), 1–8. doi:10.1103/PhysRevB.68.085327

Das, A. K., Ghose, S. K., Dev, B. N.,Kuri, G., Yang, T.R., Sponteneous nanostructural island formation and layer-to-island mass transport in Ge layers on Si(111) surfaces, *Applied Surface Science* **165** (2000) 260-270, doi: 10.1016//S0169-4332(00)0357-3

Delerue, C., Allan, G., & Lannoo, M. (1998). Optical band gap of Si nanoclusters. *Journal of Luminescence*, **80** (1-4), 65–73. doi:10.1016/S0022-2313(98)00071-4

Ding, K., & Andersen, H. (1986). Molecular-dynamics simulation of amorphous germanium. *Physical Review B*, **34** (10), 6987–6991. doi:10.1103/PhysRevB.34.6987

Dove, M. T. (2002). *Structure and Dynamics: An Atomic View of Materials* (pp. 1–331). OXFORD University Press ISBN: 978 0 19 850677.

Dowsett, M. G., Adriaens, A., Jones, G. K. C., Poolton, N., & Fiddy, S. (2008). Optically Detected X-ray Absorption Spectroscopy Measurements as a Means of Monitoring Corrosion Layers on Copper. *Analytical Chemistry*, **80** (22), 8717–8724. doi:10.1179/174329408

Efros, A. L., & Rosen, M. (2000). The Electronic Structure Of Semiconductor Nanocrystals. *Annual Review of Materials Science*, **30** (1), 475–521. doi:10.1146/annurev.matsci.30.1.475

Ekimov, A. I., Efros, A. L., & Onushchenko, A. A. (1985). Quantum size effect in semiconductor microcrystals. *Solid State Communications,* **56** (11), 921–924. doi:10.1016/S0038-1098(85)80025-9

Ekimov, A. I., & Onuschenko, A. A. (1981). Quantum size effect in three-dimensional microscopic semiconductor crystals. *Pis'ma Zh. Eksp. Teor. Fiz.*, **34** (6), 363–366.

Fan, J., & Chu, P. K. (2010). Group IV nanoparticles: synthesis, properties, and biological applications. *Small*, **6** (19), 2080–98. doi:10.1002/smll.201000543

Fitting, H.-J., Barfels, T., Trukhin, A. ., & Schmidt, B. (2001). Cathodoluminescence of crystalline and amorphous SiO2 and GeO2. *Journal of Non-Crystalline Solids*, **279** (1), 51–59. doi:10.1016/S0022-3093(00)00348-3

Fojtik, A., Weller, H., & Henglein, A. (1985). Photochemistry of semiconductor colloids. Size quantization effects in Q-cadmium arsenide. *Chemical Physics Letters*, **120** (6), 552–554. doi:10.1016/0009-2614(85)80553-4

Fujii, M., Hayashi, S., & Yamamoto, K. (1991). Growth of Ge Microcrystals in $SiO_2$ Thin Film Matrices: A Raman and Electron Microscopic Study. *Japanese Journal of Applied Physics*, **30** (Part 1, No. 4), 687–694. doi:10.1143/JJAP.30.687

Garralaga Rojas, E. J.. (2010). *Mesoporous Germanium Layer Formation by Electrochemical Etching*. PhD Thesis, Technische Fakultät, Christian-Albrechts-Universität

Gerion, D., Zaitseva, N., Saw, C., Casula, M. F., Fakra, S., Van Buuren, T., & Galli, G. (2004). Solution Synthesis of Germanium Nanocrystals: Success and Open Challenges. *Nano Letters*, **4** (4), 597–602. doi:10.1021/nl035231t

Ghandour, A. J. (2009). *Carbon Nanotubes Under Pressure : A Raman Study*. PhD Thesis, Centre for Condensed Matter and Materials Physics, School of Physics and Astronomy, Queen Mary University of London.

Gouadec, G., & Colomban, P. (2007). Raman Spectroscopy of nanomaterials: How spectra relate to disorder, particle size and mechanical properties. *Progress in Crystal Growth and Characterization of Materials*, **53** (1), 1–56. doi:10.1016/j.pcrysgrow.2007.01.001

Hayashi, R., Yamamoto, M., Tsunetomo, K., Kohno, K., Osaka, Y., & Nasu, H. (1990). Preparation and Properties of Ge Microcrystals Embedded in SiO2 Glass Films. *Japanese Journal of Applied Physics*, **29** (Part 1, No. 4), 756–759. doi:10.1143/JJAP.29.756

Hayashi, S., & Yamamoto, K. (1990). Raman scattering from microcrystals. *Phase Transitions*, **24-26** (2), 641–660. doi:10.1080/01411599008210247

Heath, J. R. (1992). A liquid-solution-phase synthesis of crystalline silicon. *Science*, **258** (5085), 1131–3. doi:10.1126/science.258.5085.1131

Heath, J. R., Shiang, J. J., & Alivisatos, A. P. (1994). Germanium quantum dots: Optical properties and synthesis. *The Journal of Chemical Physics*, **101** (2), 1607–1615. doi:10.1063/1.467781

Heiman, D. (2004). Photoluminescence Spectroscopy. Retrieved August 01, 2013, from http://tns.ndhu.edu.tw/~clcheng/class-94/bio-phy94/Class-2-PL.pdf

Heintz, A. S., Fink, M. J., & Mitchell, B. S. (2010). Silicon nanoparticles with chemically tailored surfaces. *Applied Organometallic Chemistry*, **24** (3), 236–240. doi:10.1002/aoc.1602

Henderson, E. J., Hessel, C. M., Cavell, R. G., & Veinot, J. G. C. (2010). How Processing Atmosphere Influences the Evolution of GeO 2 -Embedded Germanium Nanocrystals Obtained from the Thermolysis of Phenyl Trichlorogermane-Derived Polymers. *Chemistry of Materials*, **22** (8), 2653–2661. doi:10.1021/cm100107p

Henderson, E. J., Hessel, C. M., & Veinot, J. G. C. (2008). Synthesis and photoluminescent properties of size-controlled germanium nanocrystals from phenyl trichlorogermane-derived polymers. *Journal of the American Chemical Society*, **130** (11), 3624–32. doi:10.1021/ja710286a

Henderson, E. J., Seino, M., Puzzo, D. P., & Ozin, G. A. (2010). Colloidally Stable Germanium Nanocrystals for Photonic Applications. *ACS Nano*, **4** (12), 7683–7691. doi:10.1021/nn102521k

Hessel, C. M., Henderson, E. J., & Veinot, J. G. C. (2006). Hydrogen Silsesquioxane: A Molecular Precursor for Nanocrystalline Si−$SiO_2$ Composites and Freestanding Hydride-Surface-Terminated Silicon Nanoparticles. *Chemistry of Materials,* **18** (26), 6139–6146. doi:10.1021/cm0602803

Jiang, Y., Liu, P., Liang, Y., Li, H. B., & Yang, G. W. (2011). Promoting the yield of nanoparticles from laser ablation in liquid. *Applied Physics A*, **105** (4), 903–907. doi:10.1007/s00339-011-6557-z

Joannopoulos, J., & Cohen, M. (1973). Electronic Properties of Complex Crystalline and Amorphous Phases of Ge and Si. I. Density of States and Band Structures. *Physical Review B,* **7** (6), 2644–2657. doi:10.1103/PhysRevB.7.2644

Johnson, B. C., Haberl, B., Deshmukh, S., Malone, B. D., Cohen, M. L., McCallum, J. C., Williams, J. S., & Bradby, J. E. (2013). Evidence for the R8 Phase of Germanium. *Physical Review Letters*, **110** (8), 085502. doi:10.1103/PhysRevLett.110.085502

Karatutlu, A., Little, W. R., Sapelkin, A. V, Dent, A., Mosselmans, F. G., Cibin, G., & Taylor, R. (2013). OD-XAS and EXAFS: Structure and Luminescence in Ge Quantum Dots. *Journal of Physics: Conference Series*, **430** (012026), 1–6. doi:10.1088/1742-6596/430/1/012026

Karavanskii, V., Lomov, A., Sutyrin, A., Bushuev, V., Loikho, N., Melnik, N., Zavaritskaya, T., & Bayliss, S. (2003). Raman and X-ray studies of nanocrystals in porous stain-etched germanium. *Thin Solid Films,* **437** (1-2), 290–296. doi:10.1016/S0040-6090(03)00158-5

Kartopu, G., Bayliss, S. C., Hummel, R. E., & Ekinci, Y. (2004). Simultaneous micro-Raman and photoluminescence study of spark-processed germanium:

Report on the origin of the orange photoluminescence emission band. *Journal of Applied Physics*, **95** (7), 3466. doi:10.1063/1.1650919

Kelly, M. T., Chun, J. K. M., & Bocarsly, A. B. (1994). High efficiency chemical etchant for the formation of luminescent porous silicon. *Applied Physics Letters*, **64** (13), 1693. doi:10.1063/1.111834

Kim, S. J., Quy, O. K., Chang, L.-S., Stach, E. A., Handwerker, C. A., & Wei, A. (2010). Formation of the ST12 phase in nanocrystalline Ge at ambient pressure. *Journal of Materials Chemistry*, **20** (2), 331. doi:10.1039/b915841c

Kipphardt, H., Valkiers, S., Henriksen, F., De Bièvre, P., Taylor, P. D. P., & Tölg, G. (1999). Measurement of the isotopic composition of germanium using GeF4 produced by direct fluorination and wet chemical procedures. *International Journal of Mass Spectrometry*, **189** (1), 27–37. doi:10.1016/S1387-3806(99)00047-0

Kittel, C. (2004). *Introduction to Solid State Physics*, (*8th Edition*, pp. 1–704). Wiley ISBN: 978-0-471-41526-8.

Koch, U., Fojtik, A., Weller, H., & Henglein, A. (1985). Photochemistry of semiconductor colloids. Preparation of extremely small ZnO particles, fluorescence phenomena and size quantization effects. *Chemical Physics Letters*, **122** (5), 507–510. doi:10.1016/0009-2614(85)87255-9

Lambert, T. N., Andrews, N. L., Gerung, H., Boyle, T. J., Oliver, J. M., Wilson, B. S., & Han, S. M. (2007). Water-soluble germanium(0) nanocrystals: cell recognition and near-infrared photothermal conversion properties. *Small*, **3** (4), 691–9. doi:10.1002/smll.200600529

Li, Z., Dervishi, E., Saini, V., Zheng, L., Yan, W., Wei, S., Xu, Y., & Biris, A. S. (2010). X-ray Absorption Fine Structure Techniques. *Particulate Science and Technology*, **28** (2), 95–131. doi:10.1080/02726350903328944

Lieten, R. R., Bustillo, K., Smets, T., Simoen, E., Ager, J. W., Haller, E. E., & Locquet, J.-P. (2012). Photoluminescence of bulk germanium. *Physical Review B*, **86** (3), 035204. doi:10.1103/PhysRevB.86.035204

Littau, K. A., Szajowski, P. J., Muller, A. J., Kortan, A. R., & Brus, L. E. (1993). A luminescent silicon nanocrystal colloid via a high-temperature aerosol reaction. *The Journal of Physical Chemistry*, **97** (6), 1224–1230. doi:10.1021/j100108a019

Madelung, O. (2004). *Semiconductors: Data Handbook* (pp. 1–703). Berlin Heidelberg: Springer-Verlag ISBN 978-3-642-18865-7.

Maeda, Y., Tsukamoto, N., Yazawa, Y., Kanemitsu, Y., & Masumoto, Y. (1991). Visible photoluminescence of Ge microcrystals embedded in $SiO_2$ glassy matrices. *Applied Physics Letters*, **59** (24), 3168. doi:10.1063/1.105773

Maiman, T. H. (1960). Stimulated Optical Radiation in Ruby. *Nature*, **187** (4736), 493–494. doi:10.1038/187493a0

Malone, B. D., & Cohen, M. L. (2012). Electronic structure, equation of state, and lattice dynamics of low-pressure Ge polymorphs. *Physical Review B*, **86** (5), 054101. doi:10.1103/PhysRevB.86.054101

Marcel, B. J., Mario, M., Gin, P., Shimon, W., Paul, A. A., & Bruchez Jr., M. (1998). Semiconductor Nanocrystals as Fluorescent Biological Labels. *Science*, **281** (5385), 2013–2016. doi:10.1126/science.281.5385.2013

Mayr, H., Bug, T., Gotta, M. F., Hering, N., Irrgang, B., Janker, B., Kempf, B., Loos, R., Ofial, A. R., Remennikov, G., & Schimmel, H. (2001). Reference Scales for the Characterization of Cationic Electrophiles and Neutral Nucleophiles. *Journal of the American Chemical Society*, **123** (39), 9500–9512. doi:10.1021/ja010890y

Micoulaut, M., Cormier, L., & Henderson, G. S. (2006). The structure of amorphous, crystalline and liquid $GeO_2$. *Journal of Physics: Condensed Matter*, **18** (45), R753–R784. doi:10.1088/0953-8984/18/45/R01

Mirabella, S., Cosentino, S., Failla, M., Miritello, M., Nicotra, G., Simone, F., Spinella, C., Franzò, G., & Terrasi, A. (2013). Light absorption enhancement in closely packed Ge quantum dots. *Applied Physics Letters*, **102** (19), 193105. doi:10.1063/1.4805356

Mui, C., Han, J. H., Wang, G. T., Musgrave, C. B., & Bent, S. F. (2002). Proton Transfer Reactions on Semiconductor Surfaces. *Journal of the American Chemical Society*, **124** (15), 4027–4038. doi:10.1021/ja0171512

Mujica, A., & Needs, R. J. (1993). First-principles calculations of the structural properties, stability, and band structure of complex tetrahedral phases of germanium: ST12 and BC. *Physical Review B*, **48** (23), 10–17.

Muthuswamy, E., Iskandar, A. S., Amador, M. M., & Kauzlarich, S. M. (2013). Facile Synthesis of Germanium Nanoparticles with Size Control: Microwave versus Conventional Heating. *Chemistry of Materials,* **25** (8), 1416–1422. doi:10.1021/cm302229b

Nataraj, L. (2010). *Fabrication And Characterization Of Low-Dimensional Structures For Optoelectronic Device Applications*. PhD Thesis, Department of Electrical and Computer Engineering, University of Delaware.

Newville, M. (2001). The Atoms.inp Archive. Retrieved January 01, 2014, from http://cars9.uchicago.edu/~newville/adb/search.html

Newville, M. (2001). IFEFFIT : interactive XAFS analysis and FEFF fitting. *Journal of Synchrotron Radiation*, **8** (2), 322–324. doi:10.1107/S0909049500016964

Newville, M. (2004). Fundamentals of XAFS. Retrieved January 24, 2014, from http://xafs.org/Tutorials?action=AttachFile&do=get&target=Newville_xas_fundamentals.pdf

Niquet, Y. M., Allan, G., Delerue, C., & Lannoo, M. (2000). Quantum confinement in germanium nanocrystals. *Applied Physics Letters*, **77** (8), 1182. doi:10.1063/1.1289659

Nogami, M., & Abe, Y. (1997). Sol-gel synthesis of ge nanocrystals-doped glass and its photoluminescence. *Journal of Sol-Gel Science and Technology*, **9** (2), 139–143. doi:10.1007/BF02439394

Noll, G., Carius, R., & Fuhs, W. (1985). Photoluminescence in hydrogenated amorphous germanium (a-Ge:H). *Solid State Communications*, **55** (2), 117–120. doi:10.1016/0038-1098(85)90260-1

Nozaki, S., Sato, S., Rath, S., Ono, H., & Morisaki, H. (1999). Optical properties of tetragonal germanium nanocrystals deposited by the cluster-beam evaporation technique: New light emitting material for future. *Bulletin of Materials Science*, **22** (3), 377–381. doi:10.1007/BF02749945

Ogale, S. B., Patil, P. P., Roorda, S., & Saris, F. W. (1987). Nitridation of iron by pulsed excimer laser treatment under liquid ammonia: Mössbauer spectroscopic study. *Applied Physics Letters*, **50** (25), 1802. doi:10.1063/1.97702

Okamoto, S., & Kanemitsu, Y. (1996). Photoluminescence properties of surface-oxidized Ge nanocrystals: Surface localization of excitons. *Physical Review B*, **54** (23), 16421–16424. doi:10.1103/PhysRevB.54.16421

Oliver, D. J. (2008). *Nanoindentation-induced Deformation Mechanisms in Germanium*. PhD Thesis, Research School of Physics & Engineering, ANU College of Physical & Mathematical Sciences, The Australian National University.

Peng, M., Li, Y., Gao, J., Zhang, D., Jiang, Z., & Sun, X. (2011). Electronic Structure and Photoluminescence Origin of Single-Crystalline Germanium Oxide Nanowires with Green Light Emission. *The Journal of Physical Chemistry C*, **115** (23), 11420–11426. doi:10.1021/jp201884y

Penner-Hahn, J. E. (2003). X-ray Absorption Spectroscopy. In *Comprehensive Coordination Chemistry II* (pp. 159–186) Elsevier Ltd ISBN: 978-0-08-043748-4.

Perkampus, H. H., Grinter, H. C., & Threlfall, T. L. (2012). *UV-Vis Spectroscopy and Its Applications* (pp. 1–237). Springer London, Limited. Retrieved from http://books.google.co.uk/books?id=h5dpMQEACAAJ

Pizzagalli, L., Galli, G., Klepeis, J., & Gygi, F. (2001). Structure and stability of germanium nanoparticles. *Physical Review B*, **63** (16), 165324. doi:10.1103/PhysRevB.63.165324

Prabakar, S., Shiohara, A., Hanada, S., Fujioka, K., Yamamoto, K., & Tilley, R. D. (2010). Size Controlled Synthesis of Germanium Nanocrystals by Hydride Reducing Agents and Their Biological Applications. *Chemistry of Materials*, **22** (2), 482–486. doi:10.1021/cm9030599

Raman, C. V., & Krishnan, K. S. (1928). A New Type of Secondary Radiation. *Nature*, **121** (3048), 501–502. doi:10.1038/121501c0

Ravel, B. (2009). ATHENA User 's Guide. Retrieved from http://cars9.uchicago.edu/~ravel/software/doc/Athena/html/athena.pdf

Ravel, B. (2010). Advanced Topics in EXAFS Analysis. Retrieved January 02, 2014, from http://www.bnl.gov/ps/nsls/workshops/2010/exafs/files/Ravel.pdf

Ravel, B., & Newville, M. (2005). ATHENA, ARTEMIS, HEPHAESTUS: data analysis for X-ray absorption spectroscopy using IFEFFIT. *Journal of Synchrotron Radiation*, **12** (Pt 4), 537–41. doi:10.1107/S0909049505012719

Renishaw. (2002). Invia Raman Microscope. Retrieved from http://www.renishaw.com/en/invia-raman-microscope--6260

Richter, H., Wang, Z. P., & Ley, L. (1981). The one phonon Raman spectrum in microcrystalline silicon. *Solid State Communications*, **39** (5), 625–629. doi:10.1016/0038-1098(81)90337-9

Ridgway, M. C., Azevedo, G. D. M., Glover, C. J., Elliman, R. G., Llewellyn, D. J., Cheung, A., Johannessen, B., Brett, D. A., & Foran, G. J. (2004). EXAFS characterisation of Ge nanocrystals in silica. *Nuclear Instruments and Methods in Physics Research Section B: Beam Interactions with Materials and Atoms*, **218** , 421–426. doi:10.1016/j.nimb.2004.01.004

Ruddy, D. A., Johnson, J. C., Smith, E. R., & Neale, N. R. (2010). Size and bandgap control in the solution-phase synthesis of near-infrared-emitting germanium nanocrystals. *ACS Nano*, **4** (12), 7459–66. doi:10.1021/nn102728u

Sato, S., Ikeda, T., Hamada, K., & Kimura, K. (2009). Size regulation by bandgap-controlled etching: Application to germanium nanoparticles. *Solid State Communications*, **149** (21-22), 862–865. doi:10.1016/j.ssc.2009.03.008

Sato, S., Nozaki, S., Morisaki, H., & Iwase, M. (1995). Tetragonal germanium flims deposited by the cluster-beam evaporation technique. *Applied Physics Letters*, **66** (23), 3176. doi:10.1063/1.113714

Semaltianos, N. G., Logothetidis, S., Perrie, W., Romani, S., Potter, R. J., Edwardson, S. P., French, P., Sharp, M., Dearden, G., & Watkins, K. G. (2009). Silicon nanoparticles generated by femtosecond laser ablation in a liquid environment. *Journal of Nanoparticle Research*, **12** (2), 573–580. doi:10.1007/s11051-009-9625-y

Seo, M. a, Kim, D. S., Kim, H. S., Choi, D. S., & Jeoung, S. C. (2006). Formation of Photoluminescent Germanium Nanostructures by Femtosecond Laser Processing on Bulk Germanium: Role of Ambient Gases. *Optics Express*, **14** (11), 4908. doi:10.1364/OE.14.004908

Shell D. Kelly. (2004). Introduction to EXAFS data analysis. Retrieved January 02, 2014, from http://www.bio.anl.gov/environmental_biology/subsurface_science/shelly_kelly/documents/Basics_of_EXAFS_data_analysis2004.pdf

Shieh, J., Chen, H. L., Ko, T. S., Cheng, H. C., & Chu, T. C. (2004). Nanoparticle-Assisted Growth of Porous Germanium Thin Films. *Advanced Materials*, **16** (13), 1121–1124. doi:10.1002/adma.200306541

Stern, E., Sayers, D., & Lytle, F. (1975). Extended X-ray-absorption fine-structure technique. III. Determination of physical parameters. *Physical Review B*, **11** (12), 4836–4846. doi:10.1103/PhysRevB.11.4836

Su, C., Tsai, C.-S., Lin, C.-E., Chen, K.-H., Wang, J.-K., & Lin, J.-C. (2000). Interaction of atomic hydrogen with a Ge(111) surface: low-energy electron diffraction and surface Raman studies. *Surface Science*, **445** (2-3), 139–150. doi:10.1016/S0039-6028(99)00991-7

Takada, N., Sasaki, T., & Sasaki, K. (2008). Synthesis of crystalline TiN and Si particles by laser ablation in liquid nitrogen. *Applied Physics A*, **93** (4), 833–836. doi:10.1007/s00339-008-4748-z

Taylor, B. R., Kauzlarich, S. M., Delgado, G. R., & Lee, H. W. H. (1999). Solution Synthesis and Characterization of Quantum Confined Ge Nanoparticles. *Chemistry of Materials*, **11** (9), 2493–2500. doi:10.1021/cm990203q

Taylor, R. P., Finch, A. A., Mosselmans, J. F. W., & Quinn, P. D. (2013). The development of a XEOL and TR XEOL detection system for the I18 microfocus beamline Diamond light source. *Journal of Luminescence*, **134** , 49–58. doi:10.1016/j.jlumin.2012.09.018

Tranmission electron microscopy scheme. (2010). *http://labs.mete.metu.edu.tr/tem/TEMtext/TEMtext.html*. Retrieved August 04, 2013, from http://labs.mete.metu.edu.tr/tem/TEMtext/TEMtext.html

Tromp, M. (2007). IFEFFIT- FEFF : A ( very ) basic introduction. Retrieved January 05, 2014, from http://webcache.googleusercontent.com/search?q=cache:AKUX3o_-

LVUJ:www.diamond.ac.uk/dms/Beamlines/I18/I18_Mar07/introductiontofeff.pdf+&cd=6&hl=en&ct=clnk&gl=uk

Trukhin, A. N. (2009). Luminescence of polymorph crystalline and glassy $SiO_2$, $GeO_2$: A short review. *Journal of Non-Crystalline Solids*, **355** (18-21), 1013–1019. doi:10.1016/j.jnoncrysol.2009.01.040

Tsuchiya, T., Yamanaka, T., & Matsui, M. (1998). Molecular dynamics study of the crystal structure and phase relation of the $GeO_2$ polymorphs. *Physics and Chemistry of Minerals*, **25** (2), 94–100. doi:10.1007/s002690050091

Turner, D. R. (1960). On the Mechanism of Chemically Etching Germanium and Silicon. *Journal of The Electrochemical Society*, **107** (10), 810. doi:10.1149/1.2427519

Umezu, I., Minami, H., Senoo, H., & Sugimura, a. (2007). Synthesis of photoluminescent colloidal silicon nanoparticles by pulsed laser ablation in liquids. *Journal of Physics: Conference Series*, **59** , 392–395. doi:10.1088/1742-6596/59/1/083

Vaughn, D. D., Bondi, J. F., & Schaak, R. E. (2010). Colloidal Synthesis of Air-Stable Crystalline Germanium Nanoparticles with Tunable Sizes and Shapes. *Chemistry of Materials*, **22** (22), 6103–6108. doi:10.1021/cm1015965

Veinot, J. G. C., Henderson, E. J., & Hessel, C. M. (2009). Sol-gel derived precursors to Group 14 semiconductor nanocrystals – Convenient materials for enabling nanocrystal-based applications. *IOP Conference Series:*

*Materials Science and Engineering*, **6** , 012017. doi:10.1088/1757-899X/6/1/012017

Wang, D., Chang, Y., Liu, Z., & Dai, H. (2005). Oxidation resistant germanium nanowires: bulk synthesis, long chain alkanethiol functionalization, and Langmuir-Blodgett assembly. *Journal of the American Chemical Society*, **127** (33), 11871–5. doi:10.1021/ja053836g

Warner, J. H., & Tilley, R. D. (2006). Synthesis of water-soluble photoluminescent germanium nanocrystals. *Nanotechnology*, **17** (15), 3745–3749. doi:10.1088/0957-4484/17/15/022

Welter, E. (2003). Direct Speciation of Solids: X-ray Absorption Fine Structure Spectroscopy for Species Analysis in Solid Samples. In R. Cornelis, H. Crews, I. Caruso, & K. Heumann (Eds.), *Handbook of Elemental Speciarron: Techniques and Methodology* (pp. 526–545). John Wiley & Sons, Ltd.

Wosylus, A., Prots', Y., Schnelle, W., Hanfland, M., & Schwarz, U. (2008). Crystal structure refinement of Ge(tP12), physical properties and pressure-induced phase transformation Ge(tP12)<-->Ge(tI4). *Zeitschrift Fuer Naturforschung, B: Chemical Sciences*, **63** (6), 608–614. Retrieved from http://znaturforsch.com/rb/s63b0608.pdf

Wu, J., Sun, Y., Zou, R., Song, G., Chen, Z., Wang, C., & Hu, J. (2011). One-step aqueous solution synthesis of Ge nanocrystals from GeO2 powders. *CrystEngComm*, **13** (11), 3674. doi:10.1039/c1ce05191a

Wu, X. L., Gao, T., Bao, X. M., Yan, F., Jiang, S. S., & Feng, D. (1997). Annealing temperature dependence of Raman scattering in Ge[sup +]-implanted SiO[sub 2] films. *Journal of Applied Physics*, **82** (5), 2704. doi:10.1063/1.366089

Xu, X.-L., Zhu, L.-X., Chen, T. ., Fung, S., & Li, S.-M. (1996). Optical transitions in germanium dioxide. *Thin Solid Films*, **283** (1-2), 230–234. doi:10.1016/0040-6090(96)08732-9

Yang, C., Bley, R. A., Kauzlarich, S. M., Lee, H. W. H., & Delgado, G. R. (1999). Synthesis of Alkyl-Terminated Silicon Nanoclusters by a Solution Route. *Journal of the American Chemical Society*, **121** (22), 5191–5195. doi:10.1021/ja9828509

Yang, H. (2004). Structure and photoluminescence of Ge nanoparticles with different sizes embedded in $SiO_2$ glasses fabricated by a sol–gel method. *Journal of Crystal Growth*, **261** (4), 549–556. doi:10.1016/j.jcrysgro.2003.08.081

Yang, H., Wang, X., Shi, H., Wang, F., Gu, X., & Yao, X. (2002). Sol–gel preparation of Ge nanocrystals embedded in $SiO_2$ glasses. *Journal of Crystal Growth*, **236** (1-3), 371–375. doi:10.1016/S0022-0248(01)02158-3

Yang, L. (2007). *Self-Assembly and Ordering Nanomaterials by Liquid-Phase Pulsed Laser Ablation*. University of Bristol.

Yoshida, T., Tanabe, T., Takahara, S., & Yoshida, H. (2005). Measurement of Luminescence from Silica Glasses an Optical XRay Absorption Fine

Structures Study at Si KEdge. *Physica Scripta*, **T115** , 528. doi:10.1238/Physica.Topical.115a00528

Zhang, Y. (2013). *Structure and characterization of Ge Quantum Dots through combined Diffraction/EXAFS* (pp. 1–26) Progress report, Centre for Condensed Matter and Materials Physics, School of Physics and Astronomy, Queen Mary, University of London.